UC Berkeley
UC Berkeley Electronic Theses and Dissertations

Title

X-Ray and Deep-UV Spectroscopy of Interfaces: Liquids and Solids

Permalink

https://escholarship.org/uc/item/8ch3r917

Author

Bernal, Franky

Publication Date

2024

Peer reviewed|Thesis/dissertation

X-Ray and Deep-UV Spectroscopy of Interfaces: Liquids and Solids

By

Franky Bernal

A dissertation submitted in partial satisfaction of the

requirements for the degree of

Doctor of Philosophy

in

Chemistry

in the

Graduate Division

of the

University of California, Berkeley

Committee in charge:

Professor Richard J. Saykally, Chair
Professor Graham R. Fleming
Professor Bryan D. McCloskey

Fall 2024

Abstract

X-Ray and Deep UV Spectroscopy of Interfaces: Liquids and Solids

By

Franky Bernal

Doctor of Philosophy in Chemistry

University of California, Berkeley

Professor Richard J. Saykally, Chair

Chemistry at interfaces is of profound importance in the natural world, but only recently have the tools been developed to adequately study such finite boundaries. Much work has gone into the study of aqueous interfaces, as they play crucial roles in atmospheric, electrochemical, and biological phenomena. The bulk of this dissertation is focused on the application of nonlinear spectroscopy to study the behavior ions at the air-water interface and their effects on interfacial chemistry. I also discuss the latest work on the elusive characterization of liquid carbon produced from diamond samples.

Chapter 1: A summary of the work done in the last century surrounding interfacial ions in water is provided. Today, we know that the surface tension of salt solutions increases with added solute concentration, but at the time this observation was first made, the molecular-level understanding of ions at the air-water interface was still in its infancy. This chapter focuses on the origins of the first widely-accepted theoretical model of interfacial ions developed by Wagner, Onsager, and Samaras in the early 1930s, and on key experimental evidence that influenced the development of more sophisticated computer models. This recollection emphasizes the enormous progress made in this field, particularly in the last decade.

Chapter 2: The theory of nonlinear deep ultraviolet second harmonic generation spectroscopy is reviewed. I describe the theoretical framework vital to understanding the origin of the generated second harmonic response. From this, I describe the development of a Langmuir model, used to quantify the adsorption of ions. The optical DUV-SHG setup is described in detail and data analysis methods are discussed.

Chapter 3: The first experiment to identify a polyatomic cation adsorbed to the air-water interface using DUV-SHG is described. Guanidinium is found to adsorb to the interface with a similarly strong propensity as the thiocyanate anion. MD simulations identify a strong interfacial orientational preference for guanidinium ions wherein the cation lies parallel to the air-water boundary. Furthermore, the data are suggestive of ion-pairing effects, the exact nature of which remain to be established. This work highlights an important milestone in the study of interfacial specific ion effects.

Chapter 4: DUV-SHG, microdroplet mass spectrometry, and kinetic modeling are employed to study atmospherically-relevant sulfur oxyanions at the air-water interface and reexamine the mechanism of thiosulfate ozonation. Previous work highlighted that the doubly-charged carbonate anion exhibits a stronger affinity for the interface than does the singly-charged

bicarbonate. To determine if other multiply-charged anions are also surface active, sodium sulfate, sulfite, and thiosulfate solutions are studied. It is found that thiosulfate exhibits a strong propensity for the air-water interface, while sulfate and sulfite do not. A new kinetic model for thiosulfate ozonation is developed which agrees well with the experimental data.

Chapter 5: Efforts to produce and characterize the liquid state of carbon from irradiation of diamond samples are described. Mega-electronvolt ultrafast electron diffraction is used to study the structure of crystalline diamond thin films following excitation from an ultrafast laser pulse. Additional resonant inelastic x-ray spectroscopy measurements are performed to determine the electronic structure of laser-excited diamond. It is then determined that the physical and electronic structure of diamond remains unchanged when probed at picoseconds after excitation. This work highlights the resilient nature of diamond and the experimental challenge of evidencing a clear liquid carbon signal.

A mis padres, abuelos, hermanos, y amigos.

Table of Contents

Acknowledgments

First, a huge thank you to Rich Saykally for allowing me to join his lab when I knew absolutely nothing about lasers. My first year in a spectroscopy lab was tough, but Rich was very encouraging and his infectious enthusiasm for science kept me motivated. I learned a lot about research and thinking critically from my discussions with Rich, and I feel very fortunate to have him as my PhD advisor. Even as the lab is winding down, he keeps coming up with research ideas… makes me wish I could stick around a bit longer! I'm happy with my grad school journey and lucky to have been a member of the Saykally group. O Captain! My Captain!

I overlapped with several Saykally group members when I started, and I am thankful to have met you all. Chris Hull was an incredibly intelligent and patient mentor to me. Sumana Raj provided me with a lot of great tips while I studied for my qual, and I enjoyed our science chats with Chris in D35A. Will Cole taught me everything I know about lab safety and his questions during group meeting were always insightful. Hikaru Mizuno took over as my mentor after Chris left and taught me how to navigate the bureaucracy of the chemistry department. I met Shane Devlin during visitation weekend and by some random unexplainable chance, we both joined the Saykally group our first year. We drank a ton of high caliber beers during grad school, including our first Pliny the Elder and years later our first Pliny the Younger. As one of my best friends, we even split an apartment for a couple of years. Most importantly, I learned a lot of invaluable tips and tricks working on setups with Shane. Erika Riffe was the last to join the Saykally group and I am happy to have a friend with me as the lab closes shop. We have had a ton of great memories together and I look forward to sharing many more!

Given Rich's long career in academia, I have also had the pleasure of working with group alumni. I would like to thank Craig Schwartz for including me in beamtime experiments and holding down the night-shift with me. Craig was a great mentor to me, and I enjoyed our discussions of science, Malört, and life. Tony Rizzuto was a huge help when rebuilding the evaporation setup and I also learned a great deal of experimental skills working with him.

I chose to pursue a degree in chemistry thanks to the outstanding lectures of Michael Morgan at Bravo HS. Once at CSULA, working in the lab of Dr. Frank Gomez inspired me to pursue a doctoral degree. I am fortunate to have had their guidance at an early stage in my studies.

I am thankful for the friends that I made outside of the lab during grad school. I enjoyed homebrewing with Steve Saric and bonding over being SoCal guys. Katherine Chan was awesome for letting me tag along on her Target runs and talking about music. Paul Huang was our ace for trivia night, I still have no idea how one can retain that much information. It was always a great time being at the Katherine-Steve-Paul apartment having some beers and talking science. Thanks to Abel Ricano for helping me navigate the first-year Berkeley culture shock. Shoutout to Alex Prophet for pool nights with Shane and Erika, and for keeping rhythm on guitar during Saykally group parties.

 I would also like to thank my friends back home in LA for staying in touch daily. Ruben, Madrid, Jose, and Carlos, I am grateful for the few hours each week we would spend chatting and gaming online that allowed me to take my mind off academia.

Chapter 1 – A Brief Summary of Interfacial Ion Adsorption Studies

Water remains a prominent research subject across many disciplines, including agriculture, biology, atmospheric sciences, and chemistry.[1] Although humanity has harnessed water for millennia, it was only in the last few decades that we began to uncover its intricate nature. Questions as simple as *why is water wet? (A: "Strong tetrahedral hydrogen bonding"- R.J.S.*), have prompted much research into understanding the structure of water and its properties. This chapter comprises a brief historical overview of the research surrounding water and ions. The history of water research is rich and extensive, so the discussion below is centered on the phenomenon of surface ion adsorption.

Throughout recorded history, humans have understood the importance of sourcing clean water, but as the leading solvent on this planet, chemically pure water is naturally unobtainable. Early Greek philosophers report that while water was a critical substance, it was often contaminated and distributed in a dull murky state.[2] With modern filtration methods, clean water is accessible to more lives than ever before, free of toxic chemicals and microbes. Still, even our modern definition of clean water does not necessarily imply it is pure. Common ions exist naturally in most fresh water sources and are often supplemented into purified water to impart flavor, and atmospheric gases are nearly always dissolved to some extent. While studies have investigated the bulk properties of water and the changes induced by dissolving simple salts, only within the last century have the interfacial properties been rigorously explored.

1.1. Specific Ion Effects on Surface Tension

One of the earliest investigations of ions and their effects on a surface property of water was published in 1910 by Heydweiller and his team.[3] They recorded the surface tension of several inorganic salt solutions as a function of salt concentration via the capillary rise method. Their work was fundamentally insightful as it established simple salts altering a surface property of aqueous solutions. They found that increasing the bulk salt concentration strengthened the surface tension of solutions. Additionally, they noted that these positive increases were not constant for all ions and that the identity of the anion exhibited specific effects while that of cations did not.

By this time the Gibbs adsorption isotherm was well-established and related changes in surface tension ($d\gamma$) to the chemical activities ($d\mu_i$) of the species in solution and their surface excess (Γ_i).[4,5]

$$-d\gamma \;=\; \Gamma_1 d\mu_1 \;+\; \Gamma_2 d\mu_2 \;+\;.. \tag{1.1}$$

If we consider the density of water across a small air-water boundary, a simple definition of the interface is where the density of solvent falls to half of its bulk value. This is known as the Gibbs dividing surface and provides a theoretical finite boundary of the interface (Figure 1.1). We can modify Eq. 1.1 for an aqueous solution composed of water and a single solute species as follows:

$$\Gamma_i = -\frac{1}{RT}\left(\frac{\partial \gamma}{\partial \ln C_i}\right)_{T,p} \tag{1.2}$$

Here, we find that the direction in which the surface tension $(\partial \gamma)$ changes with increasing salt concentration $(\partial \ln C_i)$ dictates the sign of Γ_i under constant temperature and pressure conditions. The surface excess term describes the interfacial concentration of a species relative to its bulk concentration across the entire interfacial surface area. A positive surface excess would suggest a higher concentration of species in the interfacial region relative to the bulk, whereas a negative surface excess suggests a lower interfacial concentration. Typically, surfactants in water such as the ubiquitous sodium dodecyl sulfate found in soap, lower the surface tension of water and exhibit a positive surface excess since they tend to accumulate at the interface and disrupt the interfacial hydrogen bond network of water.[6] Heydweiller recorded an increasing surface tension with solute concentration, from which the Gibbs adsorption isotherm predicts a negative surface excess for ions in solution. This implies that ions are net depleted at the interface.
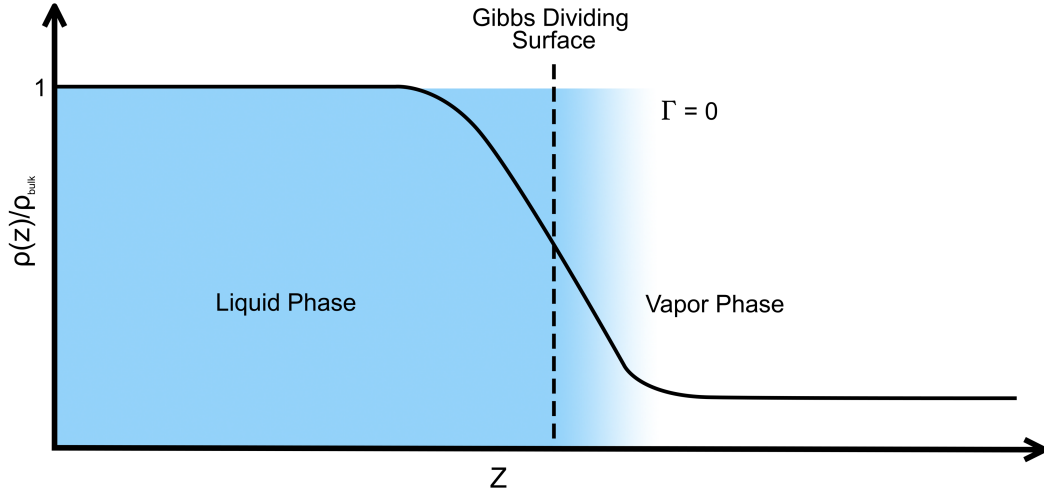
Figure 1.1 Density of water relative to its bulk value as a function of distance. Moving from the liquid phase to the vapor phase, the Gibbs dividing surface is set where the relative density falls to half its bulk value. The surface excess of water is zero at the GDS.

Heydweiller proposed that electrostatic attractions between the ions in solution prevented their accumulation at the interface and resulted in the observed surface tension results. However, this theory was too simplistic and did not consider electrostatic effects inherent to the interface. Shortly after Debye and Hückel published their seminal paper on electrolyte solutions in 1923, Wagner attempted to calculate Heydweiller's results and developed a model based on classical electrostatics.[7,8] Onsager and Samaras further simplified Wagner's work, and the Wagner-Onsager-Samaras (WOS) model was introduced.[9] In the WOS model, ions experience an electric force from the interface known as an image charge interaction.

$$q_{image} = q_{ion}\left(\frac{\varepsilon_{water} - \varepsilon_{air}}{\varepsilon_{water} + \varepsilon_{air}}\right) \tag{1.3}$$

2

Since the dielectric constant of water ($\varepsilon_{water} \approx 80$) is much greater than that of air ($\varepsilon_{air} \approx 1$), the image charge ($q_{image}$) is of the same sign and similar magnitude as the ion charge (q_{ion}). Therefore, ions in solution experience a repulsive force as they approach the interface and are repelled, as depicted in Figure 1.2. The computed results of the WOS model determined that the magnitude of the surface tension increase was constant across all ion species and was dependent only on the charge of the ion. The model did not reproduce specific ion effects on surface tension, as seen in the experimental data. Given the theoretical approximations employed in the model and the experimental uncertainty of Heydweiller's work, it was not clear whether these discrepancies had physical meaning. Nevertheless, this work bridged fundamental thermodynamics and electrostatics to explain the experimental observations and became universally adopted.
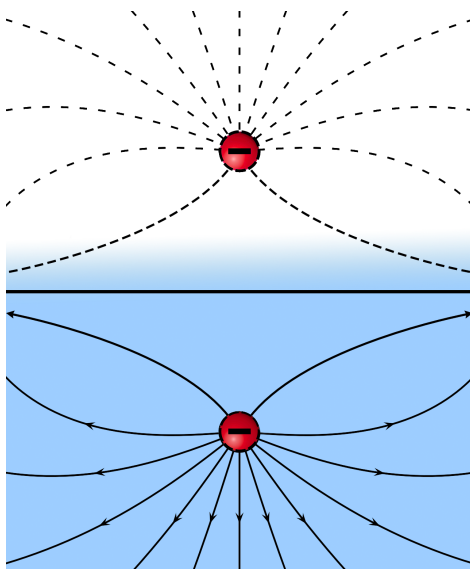
Figure 1.2 Depiction of the image charge interaction experienced by ions as they approach the interface. The image charge effected by the interface is of the same sign and therefore repulsive.

1.2. Early Evidence of Interfacial Ions

Decades after the WOS model, a series of puzzling results were published by the atmospheric community that reinvigorated interest in the study of interfacial ions.[10–12] Hu et al. examined the gas uptake of halogens (X_2) onto halide (Y^-) solution droplets via the reaction:[10]

$$X_2 + Y^- \rightarrow XY + X^- \tag{1.4}$$

The measured reaction kinetics were not adequately explained by simple bulk phase mechanisms and more halogen gas was consumed than predicted. To better model the gas uptake, researchers included an interfacial reaction mechanism in their calculations and determined that the observed

reaction kinetics were best described by this interfacial mechanism at solution concentrations > 50 mM.

In the Arctic, scientists noticed a depletion of ozone that coincided with the polar sunrise and heavily relied on the presence of bromide species.[12] Foster et al. evidenced increased reactions between Br^- and O_3 at the interface of polar snow, where it was reasoned that ocean aerosols melting on the surface of ice caps were the primary source of Br^-. Studies further emphasized that halide reactions with O_3 were ion-specific and found Br^- / O_3 reactions were favored over Cl^- / O_3, even when Cl^- ions were far more abundant than Br^-. Although there was Br_2 in the atmosphere, it was determined that much of the O_3 / Br^- reaction proceeded through an interfacial mechanism above polar ice. Given the results of the WOS model, proposing an interfacial reaction mechanism involving ions at the air-water interface was unconventional. A comprehensive aerosol study in 2004 confirmed these results and demonstrated that indeed bromide ions were reacting with ozone at the air-water interface.[13]

In response to the emerging experimental results, a theoretical effort was made to reconcile the early theories of WOS with experiments.[11,14–20] Specifically, how could a negative surface excess for ions in solution hold when there is growing evidence for interfacial reaction mechanisms involving halides? Equipped with modern computational advances, molecular dynamics simulations were employed to study specific ion effects at the air-water interface. In these early simulations, rectangular slabs were populated with a few hundred water molecules and a single ion pair. These slab simulations modeled ion-water interactions at the infinitely dilute limit which was necessary to capture specific ion effects. The first notable results showed that anions tended to reside closer to the interface than did cations.[15] Subsequent simulations, including the landmark paper by Jungwirth and Tobias, found that including polarizability terms for ions and water molecules resulted in the larger halides demonstrating a propensity for the interface, the magnitudes of which scaled with size, $Cl^- < Br^- < I^-$.[18] It was rationalized that ions in the bulk experienced a small net electric field from the surrounding water dipoles, but at the interface, the asymmetric solvent environment strongly polarizes the ion and only the larger, more "soft" ions were stabilized at the interface. These results noted that not only were large halides surface active, but also suggested ion concentrations could actually be enhanced at the interface relative to the bulk.

To rationalize the negative surface excess predicted by the Gibbs adsorption isotherm, ion densities relative to the bulk were simulated across the interface.[21] Although some ions were exhibiting increased interfacial surface density, simulations found there was a considerable region of subsurface depletion just below the interface. Thus, when ion densities were integrated across the entire interfacial region, the net surface excess was indeed negative as predicted by the WOS model and Gibbs adsorption isotherm. The regions of surface enhancement and subsurface depletion are illustrated in Figure 1.3.
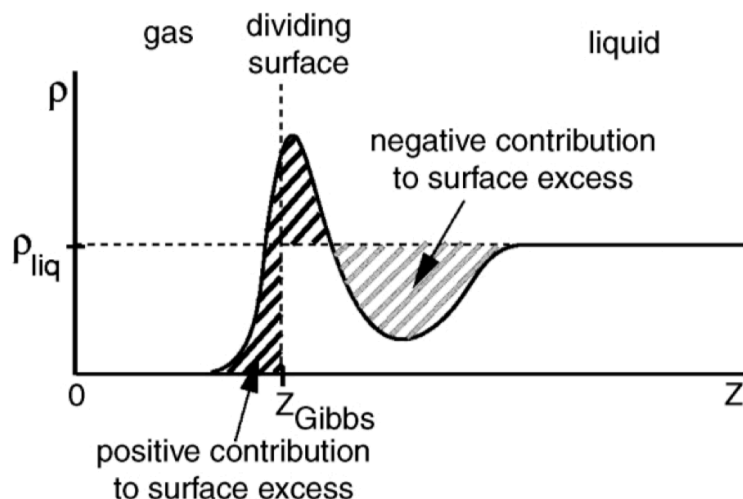
Figure 1.3 Density profile plot of a surface-active ion demonstrating an enhanced density at the interface. A subsurface depletion region is highlighted as a negative contribution to the surface excess. Integrating across Z, the net surface excess is negative and in agreement with the Gibbs adsorption isotherm for ions in solution. Reprinted with permission from Ref 21. Copyright 2004 Elsevier.

1.3. Spectroscopic Measurements

The measurements taken by the atmospheric community were made primarily via mass spectrometry in efforts to detail bulk reaction kinetics and mechanisms. To experimentally verify specific ion effects predicted by theory, new surface-specific measurements were necessary. Fortunately, by the early 2000s, nonlinear second harmonic generation (SHG) spectroscopy had been established by the pioneering work of the Eisenthal and Shen groups.[22–25] These techniques provided unrivaled surface specificity that allowed researchers to probe the topmost molecular layers of the air-water interface, ca. 1 nm into solutions.

SHG was first used by the Eisenthal group to study the average dipole orientation of water molecules at the air-water interface and concluded that most water molecules point their O-H groups towards the bulk. The Shen group would further elucidate the orientational preference of water molecules by recording a vibrational-SFG spectrum of the surface of water and concluded that ca. 20% of water molecules point one O-H group into the vapor phase.[25] With the interfacial spectrum of neat water well-detailed, subsequent studies monitored perturbations in the spectra due to the addition of ions.[26–28] These studies were able to infer the presence of interfacial ions through a suppression of the interfacial dangling water O-H peak and increases in the O-H stretch band.

By leveraging ion-specific charge-transfer-to-solvent (CTTS) transitions, Petersen and Saykally developed deep-ultraviolet SHG (DUV-SHG) to directly probe interfacial anions.[29–32] In aqueous solution, many anions exhibit broad absorption bands in the UV region attributed to CTTS transitions, wherein excitation from a UV light source ejects an electron from the ion into the solvent.[33] These transitions were ideal candidates for resonance-enhanced DUV-SHG studies and provided a direct route to probe interfacial ions. Azide (N_3^-) was the first of many ions confirmed to reside at the air-water interface via DUV-SHG. An added benefit to this technique was the ability

to measure a solution as function of solute concentration and thereby extract thermodynamic information. Fitting the concentration-dependent DUV-SHG results to a Langmuir isotherm allowed for the Gibbs free energy of adsorption for ions to be determined. Not only was the DUV-SHG signal qualitatively indicative of ions at the interface, but it also allowed for a quantitative description of surface propensity. Temperature-dependent DUV-SHG would enhance our thermodynamic understanding by extracting enthalpic and entropic adsorption contributions.[34] Rizzuto et al. adapted DUV-SHG into a nonlinear electronic sum-frequency technique (DUV-ESFG) by introducing a broadband white light continuum based on previous work by the Tahara group.[35,36] Instead of relying on the time-consuming pointwise measurements of DUV-SHG, an electronic interfacial spectrum spanning ca. 30 nm was now obtainable. DUV-ESFG was able to characterize interfacial ion transitions and evidenced energy shifts of the CTTS transitions at the interface relative to the bulk. These studies directly evidenced ions at the air-water interface and helped develop a deeper understanding of the ion adsorption phenomenon. Further theoretical details of nonlinear SHG are provided in Chapter 2.

1.4. Mechanism of Ion Adsorption

The thermodynamic information gathered from DUV-SHG studies helped to characterize ion surface propensity, but alone was insufficient to elicit a full molecular description of the ion adsorption phenomenon. Although the simulations by Jungwirth and Tobias were key to predicting ion adsorption, they lacked a clear mechanism of the molecular driving force. In collaboration with the Geissler group, Saykally and coworkers determined the Gibbs free energy for adsorption of thiocyanate anions to the air-water interface as a function of temperature to extract enthalpic and entropic contributions.[34] MD simulations added perspective to these results, and allowed for the mechanistic details to be determined. In their mechanism, ions fluctuating to the interface shed one or more water molecules from their solvation shell, which then move into the bulk. The displaced water molecules become fully coordinated in the bulk and provide an enthalpic driving force for ion adsorption. Moreover, ions situated at the interface dampen interfacial capillary waves, which introduces an entropic penalty to surface adsorption. This mechanism highlights the fact that ion solvation plays a major role in determining surface activity, since weakly hydrated ions (e.g., SCN^-, I^-) are most likely to shed their solvation shell and exhibit an affinity for the interface than are strongly hydrated ions (e.g., F^-, Na^+).

The balance between enthalpic and entropic contributions is not constant at all interfaces. Studies of the mechanism of ion adsorption to the graphene-water and oil-water interface revealed different underlying mechanistic details. At the graphene-water interface, the graphene sheet itself dampens capillary waves, yet limits adjacent ion rotational degrees of freedom, resulting in an overall lowered entropic cost compared to the air-water interface. Additionally, direct graphene-ion interactions contribute to the enthalpic driving force more than does solvent repartitioning. At the oil-water interface, the enthalpic and entropic contributions are reversed and the main driving force for ion adsorption is entropic in nature.[37] This is due to the formation of "water fingers" extending into the hydrophobic layer and increasing water density fluctuations.

While much progress has been made in describing ions at interfaces, our description of ion adsorption continues to evolve. Recent studies have discovered that ion pairing effects may further complicate the mechanism of adsorption. X-ray photoelectron spectroscopy measurements identified the surprising surface enhancement of the doubly-charged carbonate ions over

bicarbonate ions at the air-water interface.[38] Given the advances in surface adsorption understanding from the early 2000s, it was thought that multiply charged ions would be too "hard" to adsorb to the air-water interface. To gain a deeper understanding of the mechanism for carbonate surface adsorption, Devlin et al. performed DUV-SHG measurements of carbonate and bicarbonate, finding that indeed the carbonate ion demonstrates an affinity for the interface about ten times stronger than bicarbonate.[39] MD simulations by the Pascal group identified "agglomeration" of the carbonate ions with sodium counterions, leading to near-neutral clusters that subsequently follow the thiocyanate adsorption mechanism driven by solvent repartitioning (Figure 1.4).
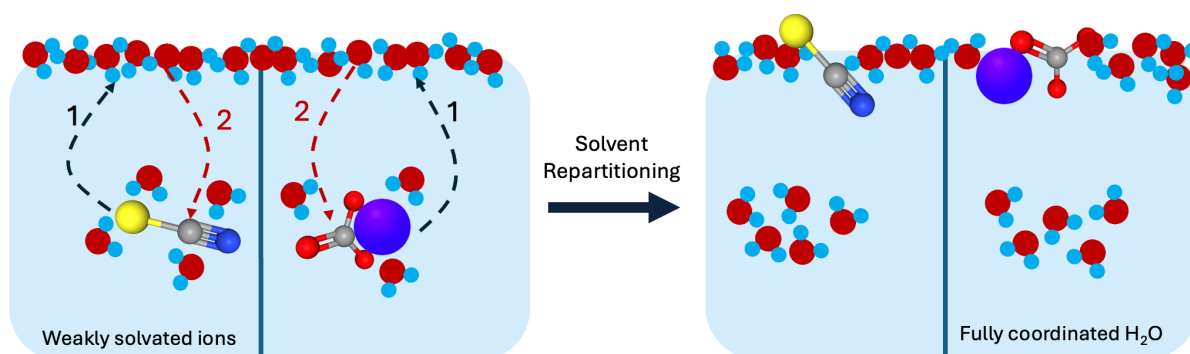
Figure 1.4 Molecular cartoon depicting the mechanism of ion adsorption to the air-water interface. 1. ions move to the interface and shed water molecules from their solvation shell. 2. Interfacial water molecules are repartitioned into the bulk, resulting in an enthalpic driving force for ion adsorption.

1.5. Next Steps

Our fundamental understanding of the mechanism behind ion adsorption has dramatically advanced in the last few decades, but it is still developing, as there are many interfacial systems yet to be explored. Cations have been generally thought to be too nonpolarizable to exhibit much surface affinity; however, as will be shown in Chapter 3, this is not necessarily true of all positively charged ions. Additionally, there are several environmentally-relevant multiply charged ions that may need to be reconsidered, some of which are explored in Chapter 4.

References
(1)   Jackson, R. B.; Carpenter, S. R.; Dahm, C. N.; McKnight, D. M.; Naiman, R. J.; Postel, S. L.; Running, S. W. Water in a Changing World. *Ecological Applications* **2001**, *11* (4), 1027–1045. https://doi.org/10.1890/1051-0761(2001)011[1027:WIACW]2.0.CO;2.
(2)   Cobb, C.; Goldwhite, H. *Creations Of Fire: Chemistry's Lively History From Alchemy To The Atomic Age*; Basic Books, 2009.
(3)   Heydweiller, A. Interdependence of the Physical Properties of Solutions. II. Surface Tension and Electrical Conductivity of Aqueous Salt-Solutions. *Ann. d. Physik* **1910**, *4* (33), 145–185.
(4)   Girolami, G. S. A Brief History of Thermodynamics, As Illustrated by Books and People. *J. Chem. Eng. Data* **2020**, *65* (2), 298–311. https://doi.org/10.1021/acs.jced.9b00515.

(5)   Gibbs, J. W. On the Equilibrium of Heterogeneous Substances. *American Journal of Science* **1878**, *s3-16* (96), 441–458. https://doi.org/10.2475/ajs.s3-16.96.441.

(6)   Gragson, D. E.; McCarty, B. M.; Richmond, G. L. Surfactant/Water Interactions at the Air/Water Interface Probed by Vibrational Sum Frequency Generation. *J. Phys. Chem.* **1996**, *100* (34), 14272–14275. https://doi.org/10.1021/jp961034p.

(7)   Debye, P.; Hückel, E. On the Theory of Electrolytes. I. Freezing Point Depression and Related Phenomena. *Phys. Z* **1923**, *24*, 185–206.

(8)   Wagner, C. The Surface Tension of Dilute Solutions of Electrolytes. *Phys. Z* **1924**, *25*, 474–477.

(9)   Onsager, L.; Samaras, N. N. T. The Surface Tension of Debye-Hückel Electrolytes. *The Journal of Chemical Physics* **1934**, *2* (8), 528–536. https://doi.org/10.1063/1.1749522.

(10)   Hu, J. H.; Shi, Q.; Davidovits, P.; Worsnop, D. R.; Zahniser, M. S.; Kolb, C. E. *Reactive Uptake of Cl2(g) and Br2(g) by Aqueous Surfaces as a Function of Br- and I- Ion Concentration: The Effect of Chemical Reaction at the Interface*. ACS Publications. https://doi.org/10.1021/j100021a050.

(11)   Knipping, E. M.; Lakin, M. J.; Foster, K. L.; Jungwirth, P.; Tobias, D. J.; Gerber, R. B.; Dabdub, D.; Finlayson-Pitts, B. J. Experiments and Simulations of Ion-Enhanced Interfacial Chemistry on Aqueous NaCl Aerosols. *Science* **2000**, *288* (5464), 301–306. https://doi.org/10.1126/science.288.5464.301.

(12)   Foster, K. L.; Plastridge, R. A.; Bottenheim, J. W.; Shepson, P. B.; Finlayson-Pitts, B. J.; Spicer, C. W. The Role of Br2 and BrCl in Surface Ozone Destruction at Polar Sunrise. *Science* **2001**, *291* (5503), 471–474. https://doi.org/10.1126/science.291.5503.471.

(13)   Hunt, S. W.; Roeselová, M.; Wang, W.; Wingen, L. M.; Knipping, E. M.; Tobias, D. J.; Dabdub, D.; Finlayson-Pitts, B. J. Formation of Molecular Bromine from the Reaction of Ozone with Deliquesced NaBr Aerosol: Evidence for Interface Chemistry. *J. Phys. Chem. A* **2004**, *108* (52), 11559–11572. https://doi.org/10.1021/jp0467346.

(14)   Wilson, M. A.; Pohorille, Andrew.; Pratt, L. R. Molecular Dynamics of the Water Liquid-Vapor Interface. *The Journal of Physical Chemistry* **1987**, *91* (19), 4873–4878. https://doi.org/10.1021/j100303a002.

(15)   Wilson, M. A.; Pohorille, A. Interaction of Monovalent Ions with the Water Liquid–Vapor Interface: A Molecular Dynamics Study. *The Journal of Chemical Physics* **1991**, *95* (8), 6005–6013. https://doi.org/10.1063/1.461592.

(16)   Stuart*, S. J.; Berne†, B. J. *Surface Curvature Effects in the Aqueous Ionic Solvation of the Chloride Ion*. ACS Publications. https://doi.org/10.1021/jp991671q.

(17)   Jungwirth, P.; Tobias, D. J. Surface Effects on Aqueous Ionic Solvation: A Molecular Dynamics Simulation Study of NaCl at the Air/Water Interface from Infinite Dilution to Saturation. *J. Phys. Chem. B* **2000**, *104* (32), 7702–7706. https://doi.org/10.1021/jp000941y.

(18)   Jungwirth, P.; Tobias, D. J. Ions at the Air/Water Interface. *J. Phys. Chem. B* **2002**, *106* (25), 6361–6373. https://doi.org/10.1021/jp020242g.

(19)   Pegram, L. M.; Record, M. T. Partitioning of Atmospherically Relevant Ions between Bulk Water and the Water/Vapor Interface. *Proceedings of the National Academy of Sciences* **2006**, *103* (39), 14278–14281. https://doi.org/10.1073/pnas.0606256103.

(20)   Jungwirth, P.; Tobias, D. J. Specific Ion Effects at the Air/Water Interface. *Chem. Rev.* **2006**, *106* (4), 1259–1281. https://doi.org/10.1021/cr0403741.

(21)   Vrbka, L.; Mucha, M.; Minofar, B.; Jungwirth, P.; Brown, E. C.; Tobias, D. J. Propensity of Soft Ions for the Air/Water Interface. *Current Opinion in Colloid & Interface Science* **2004**, *9* (1), 67–73. https://doi.org/10.1016/j.cocis.2004.05.028.

(22)   Goh, M. C.; Hicks, J. M.; Kemnitz, K.; Pinto, G. R.; Heinz, T. F.; Eisenthal, K. B.; Bhattacharyya, K. Absolute Orientation of Water Molecules at the Neat Water Surface. *J. Phys. Chem.* **1988**, *92* (18), 5074–5075. https://doi.org/10.1021/j100329a003.

(23)   Shen, Y. R. Surface Properties Probed by Second-Harmonic and Sum-Frequency Generation. *Nature* **1989**, *337* (6207), 519–525. https://doi.org/10.1038/337519a0.

(24)   Shen, Y. R. Optical Second Harmonic Generation at Interfaces. *Annual Review of Physical Chemistry* **1989**, *40* (1), 327–350. https://doi.org/10.1146/annurev.pc.40.100189.001551.

(25)   Du, Q.; Superfine, R.; Freysz, E.; Shen, Y. R. Vibrational Spectroscopy of Water at the Vapor/Water Interface. *Phys. Rev. Lett.* **1993**, *70* (15), 2313–2316. https://doi.org/10.1103/PhysRevLett.70.2313.

(26)   Schultz, M. J.; Baldelli, S.; Schnitzer, C.; Simonelli, D. Aqueous Solution/Air Interfaces Probed with Sum Frequency Generation Spectroscopy. *J. Phys. Chem. B* **2002**, *106* (21), 5313–5324. https://doi.org/10.1021/jp014466v.

(27)   Raymond, E. A.; Richmond, G. L. Probing the Molecular Structure and Bonding of the Surface of Aqueous Salt Solutions. *J. Phys. Chem. B* **2004**, *108* (16), 5051–5059. https://doi.org/10.1021/jp037725k.

(28)   Mucha, M.; Frigato, T.; Levering, L. M.; Allen, H. C.; Tobias, D. J.; Dang, L. X.; Jungwirth, P. Unified Molecular Picture of the Surfaces of Aqueous Acid, Base, and Salt Solutions. *J. Phys. Chem. B* **2005**, *109* (16), 7617–7623. https://doi.org/10.1021/jp0445730.

(29)   Petersen, P. B.; Saykally, R. J. Confirmation of Enhanced Anion Concentration at the Liquid Water Surface. *Chemical Physics Letters* **2004**, *397* (1–3), 51–55. https://doi.org/10.1016/j.cplett.2004.08.049.

(30)   Petersen, P. B.; Johnson, J. C.; Knutsen, K. P.; Saykally, R. J. Direct Experimental Validation of the Jones–Ray Effect. *Chemical Physics Letters* **2004**, *397* (1), 46–50. https://doi.org/10.1016/j.cplett.2004.08.048.

(31)   Petersen, P. B.; Saykally, R. J. ON THE NATURE OF IONS AT THE LIQUID WATER SURFACE. *Annu. Rev. Phys. Chem.* **2006**, *57* (1), 333–364. https://doi.org/10.1146/annurev.physchem.57.032905.104609.

(32)   Petersen, P. B.; Saykally, R. J. Probing the Interfacial Structure of Aqueous Electrolytes with Femtosecond Second Harmonic Generation Spectroscopy. *J. Phys. Chem. B* **2006**, *110* (29), 14060–14073. https://doi.org/10.1021/jp0601825.

(33)   Blandamer, M. J.; Fox, M. F. Theory and Applications of Charge-Transfer-to-Solvent Spectra. *Chem. Rev.* **1970**, *70* (1), 59–93. https://doi.org/10.1021/cr60263a002.

(34)   Otten, D. E.; Shaffer, P. R.; Geissler, P. L.; Saykally, R. J. Elucidating the Mechanism of Selective Ion Adsorption to the Liquid Water Surface. *Proceedings of the National Academy of Sciences* **2012**, *109* (3), 701–705. https://doi.org/10.1073/pnas.1116169109.

(35)   Rizzuto, A. M.; Irgen-Gioro, S.; Eftekhari-Bafrooei, A.; Saykally, R. J. Broadband Deep UV Spectra of Interfacial Aqueous Iodide. *J. Phys. Chem. Lett.* **2016**, *7* (19), 3882–3885. https://doi.org/10.1021/acs.jpclett.6b01931.

(36)   Yamaguchi, S.; Tahara, T. Precise Electronic χ(2) Spectra of Molecules Adsorbed at an Interface Measured by Multiplex Sum Frequency Generation. *J. Phys. Chem. B* **2004**, *108* (50), 19079–19082. https://doi.org/10.1021/jp045306x.

(37)   Devlin, S. W.; Benjamin, I.; Saykally, R. J. On the Mechanisms of Ion Adsorption to Aqueous Interfaces: Air-Water vs. Oil-Water. *Proceedings of the National Academy of Sciences* **2022**, *119* (42), e2210857119. https://doi.org/10.1073/pnas.2210857119.

(38)   Lam, R. K.; Smith, J. W.; Rizzuto, A. M.; Karslıoğlu, O.; Bluhm, H.; Saykally, R. J. Reversed Interfacial Fractionation of Carbonate and Bicarbonate Evidenced by X-Ray Photoemission Spectroscopy. *J. Chem. Phys.* **2017**, *146* (9), 094703. https://doi.org/10.1063/1.4977046.

(39)   Devlin, S. W.; Jamnuch, S.; Xu, Q.; Chen, A. A.; Qian, J.; Pascal, T. A.; Saykally, R. J. Agglomeration Drives the Reversed Fractionation of Aqueous Carbonate and Bicarbonate at the Air–Water Interface. *J. Am. Chem. Soc.* **2023**, *145* (41), 22384–22393. https://doi.org/10.1021/jacs.3c05093.

Chapter 2 – SHG Spectroscopy and Data Analysis

This chapter establishes the theoretical framework for DUV-SHG spectroscopy, derives the simple Langmuir model underlying the analysis of data, and describes the experimental setup and the actual data analysis methods.

2.1. Second Harmonic Generation

In 1960, the first ruby lasers were developed, giving researchers access to millisecond-long pulses of highly monochromatic 694 nm light[1]. The peak intensities effected by these lasers set the stage for the first demonstration of second harmonic generation in quartz a year later[2]. As laser technologies have continued to evolve, modern amplified systems are able to deliver sub-100 femtosecond pulses with pulse energies in the tens of millijoules. As will be demonstrated below, the field of nonlinear optical spectroscopy has greatly benefitted from these technological advances as the increased pulse energies have unlocked the ability to perform higher-order nonlinear spectroscopies.

The following is adapted from expert works on nonlinear spectroscopy and several established papers; the reader should refer to them for an in-depth discussion of these topics[3–9]. When light traverses a dielectric medium, the electric field (E) of the oscillating electromagnetic waves induces dipole moments, causing the material to become polarized (P). The degree to which the dielectric becomes polarized depends on its electric susceptibility (χ). We can express the polarization of a material as:

$$P(t) = \epsilon_0 \chi E(t) \tag{2.1}$$

Where ϵ_0 is the vacuum permittivity. At high electric field strengths, the polarization response of a dielectric becomes nonlinear and is better described by a Taylor series expansion in $E(t)$ accounting for higher-order contributions:

$$P(t) = \epsilon_0 \chi^{(1)} E(t) + \epsilon_0 \chi^{(2)} E^2(t) + \epsilon_0 \chi^{(3)} E^3(t) \tag{2.2}$$

The second term in the expanded polarization of Eq. 2.2 is the nonlinear second-order polarization ($P^{(2)}$), which is proportional to the second-order susceptibility ($\chi^{(2)}$) and the square of the electric field:

$$P^{(2)}(t) = \epsilon_0 \chi^{(2)} E^2(t) \tag{2.3}$$

If we substitute into Eq. 2.3, the electric field expressed as a wave of frequency ω and amplitude E as shown in Eq. 2.4:

$$E(t) = E e^{-i\omega t} + c.c. \tag{2.4}$$

The expression for $P^{(2)}(t)$ can then be rewritten as:

$$P^{(2)}(t) = 2\epsilon_0\chi^{(2)}E(t)^2 + \left(\epsilon_0\chi^{(2)}E(t)^2 e^{-i2\omega t} + c.c.\right) \qquad (2.5)$$

here we see the appearance of a 2ω term. Therefore, after applying a sufficiently intense electric field with frequency ω, the induced second-order polarization drives an electric field at twice the input frequency, i.e., second harmonic generation.

In the dipole approximation, the second harmonic field is only generated in non-centrosymmetric media such as certain crystals (e.g., quartz, beta barium borate, lithium triborate) and at interfaces. To understand this, consider the polarization response in materials with inversion symmetry. The polarization is denoted as in Eq. 2.3 for the positive direction; however, if we reverse the electric field direction ($-E(t)$), then the instantaneous induced second-order polarization should follow ($-P^{(2)}(t)$):

$$-P^{(2)}(t) = \epsilon_0\chi^{(2)}[-E(t)]^2 = \epsilon_0\chi^{(2)}E^2(t) = P^{(2)}(t) \qquad (2.6)$$

However, simplifying the expression we find that $-P^{(2)} = P^{(2)}$. In centrosymmetric media, to satisfy Eq. 2.6, $\chi^{(2)} = 0$ and there is no net polarization response to drive SHG. For isotropic liquids, this means that the bulk solution will not generate second harmonic light, but the interface, which naturally has broken inversion symmetry, can produce a second harmonic signal, and thus highlights the surface specificity of this technique.
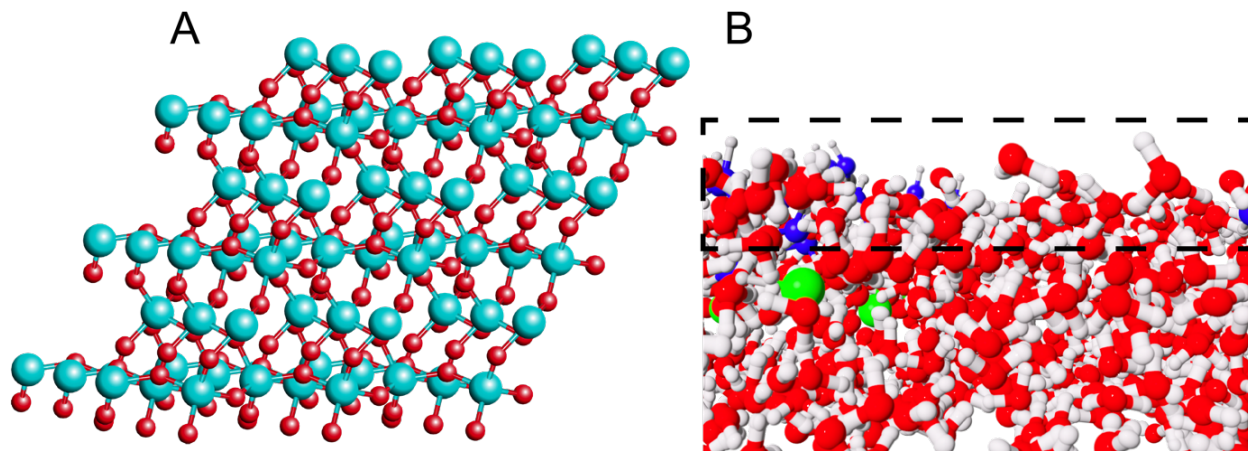
Figure 2.1 Non-centrosymmetric environments where SHG is allowed. **A)** Quartz crystal structure exhibiting no inversion center. **B)** Molecular picture of the air-water interface, the region in the dashed rectangle exhibits broken inversion symmetry.

2.2. Resonant Deep Ultraviolet SHG (DUV-SHG)

SHG can be produced in certain crystals and environments that lack inversion symmetry, including the surface of neat water. However, SHG becomes a particularly powerful interfacial molecular probe when resonant with a transition specific to the chromophore being studied. The link between SHG and molecular information lies within the second-order susceptibility. A dielectric's polarization response to an electric field can be visualized as a collection of atoms exhibiting a dipole response to the applied field. We can express the macroscopic second-order susceptibility as the sum of N atoms each with their own molecular analogue of $\chi^{(2)}$, viz. the hyperpolarizability, β:

$$\chi^{(2)} = \sum_n \beta_n \propto \sum_n \frac{|\mu_{0,n}(\alpha_{0,n})|}{\omega_n - \omega_{SHG} - i\Gamma_n} \tag{2.7}$$

Under two-photon resonant conditions, the SHG wavelength is resonant with a transition of the chromophore and can enhance the signal according to the right side of Eq. 2.7. Here, $\mu_{0,n}$, $\alpha_{0,n}$, ω_n, ω_{SHG}, and Γ_n correspond to the transition dipole moment matrix, two-photon absorption polarizability tensor, resonant transition frequency, SHG frequency, and the lifetime of the resonant transition. Tuning the input wavelength so that the SHG wavelength overlaps with the resonant transition decreases the term in the denominator, increasing the effective second-order susceptibility and consequently the SHG signal as well. Additionally, Eq 2.7 highlights the selection rules of resonance-enhanced SHG, which are that the resonant transition must be both one and two-photon active as the numerator term must be nonzero. A bulk UV-Vis spectrum is useful in identifying the position and strength of one-photon active transitions; however, these may not necessarily be two-photon active as well. If the resonant transition is specific to a single chromophore and no other molecules have overlapping transitions at the resonant wavelength, then the increased SHG signal becomes a direct probe of the chromophore. This allows us to experimentally confirm an ion's presence at the air-water interface using SHG, as depicted in Figure 2.2. Under the electric dipole approximation, we assume bulk quadrupole and higher-order multipole signals do not significantly contribute to the measured SHG signal.
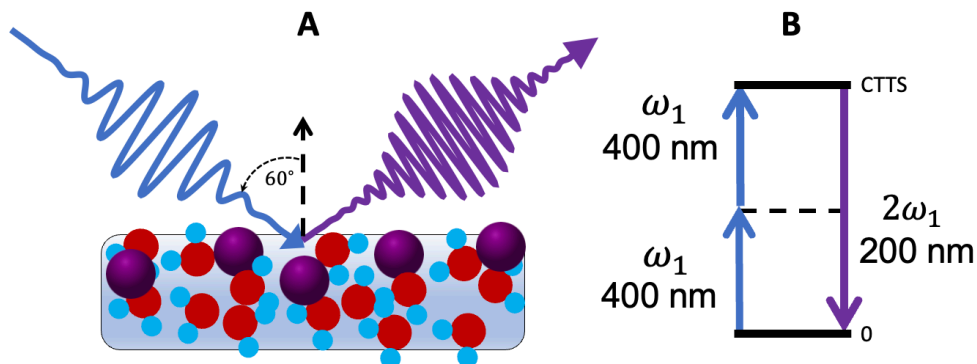
Figure 2.2 Resonant DUV-SHG at the aqueous interface. **A)** DUV-SHG in reflection geometry at the air-water interface. **B)** Diagram of the SHG process where two photons are used to generate an upconverted third photon resonant with a transition.

2.3. Langmuir Isotherm

Since $\chi^{(2)}$ for resonant SHG is proportional to the sum of interfacial atoms; if we assume that the orientation of the interfacial molecules remains invariant to changes in the interfacial population, then the orientationally averaged hyperpolarizability is assumed to remain constant. In this case, the SHG signal becomes directly proportional to the interfacial population of ions (N) and their effective hyperpolarizability, $\langle \beta \rangle_{orient.}$.

$$\chi^{(2)} = \sum_n \beta_n = N \times \langle \beta \rangle_{orient.} \tag{2.8}$$

We can expect the above to hold naturally for spherical ions and small molecules known to adsorb to the interface with a defined orientation, but large molecules may deviate from this assumption[10–12]. As more ions partition to the interface, we expect the SHG response will scale accordingly. This allows the SHG signal response as a function of concentration to be modeled by a Langmuir adsorption isotherm. Although several adsorption models have been used in literature to fit SHG data, this dissertation relies on the simplicity of a Langmuir model as it fits the data presented well[13–15].

We start by noting that the SHG intensity is proportional to the squared input intensity and the susceptibility of the interface, which consists of water molecules and ions:

$$I_{2\omega} \propto \left| \chi^{(2)}_{water} + \chi^{(2)}_{ion} \right|^2 \times I_\omega^2 \tag{2.9}$$

By subbing in the expression for $\chi^{(2)}$ from Eq. 2.8 and dividing the SHG intensity by the input intensity squared, we obtain:

$$\frac{I_{2\omega}}{I_\omega^2} \propto |N_{water} \times \langle \beta \rangle_{water} + N_{ion} \times \langle \beta \rangle_{ion}|^2 \tag{2.10}$$

The experiments presented in this dissertation were done assuming laser irradiation to be far from any water resonances, and therefore that the response of water is a purely real signal. However, since the SHG wavelength is typically tuned to a resonant transition, $\chi^{(2)}_{ion}$ is resonantly enhanced following Eq. 2.7 and therefore it is a complex value with both real and imaginary components:

$$\frac{I_{2\omega}}{I_\omega^2} \propto (N_{water} \times Re\{\langle \beta \rangle_{water}\} + N_{ion} \times Re\{\langle \beta \rangle_{ion}\})^2 + (N_{ion} \times Im\{\langle \beta \rangle_{ion}\})^2 \tag{2.11}$$

Dividing the above equation by N_{water} replaces N_{ion} with N_s, the surface concertation of ions:

$$\frac{I_{2\omega}}{I_\omega^2} \propto (A + N_s \times B)^2 + (N_s \times C)^2 \tag{2.12}$$

The real and imaginary portions of Eq. 2.11 are grouped into the new variables A, B, and C.

In a Langmuir model, we assume that ions and water molecules exchange positions from the interface to the bulk:

$$water_{surface} + ion_{bulk} \leftrightarrow water_{bulk} + ion_{surface} \tag{2.13}$$
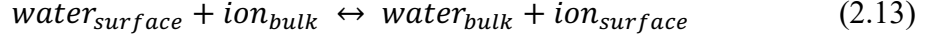
Using Eq. 2.13, we generate the equilibrium expression below:

$$K_{ads} = \frac{[water]_{bulk} \times [ion]_{surface}}{[water]_{surface} \times [ion]_{bulk}} \tag{2.14}$$

Using the Langmuir isotherm assumption that there exists a maximum number of surface sites, $[sites]_{max}$, then $[sites]_{max} = [water]_{surface} + [ion]_{surface}$. We use this relation to substitute for $[water]_{surface}$ and then solve Eq. 2.14 for $[ion]_{surf}$ which is equal to N_s:

$$[ion]_{surf} = [sites]_{max} \times \frac{[ion]_{bulk}}{[water]_{bulk} \times K_{ads}^{-1} + [ion]_{bulk}} = N_s \tag{2.15}$$

We convert concentrations to mole fraction (X_{ion}), and relate the equilibrium constant to the Gibbs free energy ($K_{ads} = e^{\frac{-\Delta G}{RT}}$). The maximum number of surface sites term is incorporated into the B and C parameters. The final fitting expression is used to extract Gibbs free energies of adsorption for ions at the air-water interface from normalized SHG intensities:

$$\frac{I_{2\omega}}{I_\omega^2} = \left(A + B \frac{X_{ion}}{(1-X_{ion})e^{\frac{\Delta G}{RT}} + X_{ion}} \right)^2 + \left(C \frac{X_{ion}}{(1-X_{ion})e^{\frac{\Delta G}{RT}} + X_{ion}} \right)^2 \tag{2.16}$$

2.4. Experimental DUV-SHG Setup

A Ti-Sapphire regenerative amplifier (Spectra-Physics, Spitfire Ace, 2 mJ, 1 kHz, 100 fs) is seeded by an 800 nm Ti-Sapphire oscillator (Spectra-Physics, Mai Tai, 1 W, 80 MHz, 100 fs) and pumped by a high power Nd:YLF laser (Spectra-Physics, Empower, 22 W, 1 kHz). The output wavelength of the Spitfire is centered at 800 nm and is used to generate the fundamental. input beam in all SHG experiments presented in this dissertation. For fundamental light at 400 nm, the Spitfire output is directed through a type-I beta barium borate crystal (Edmund Optics, β-BBO). For measurements at fundamental wavelengths below and above 400 nm, the Spitfire output is directed into an optical parametric amplifier (TOPAS Prime), typically generating pulse energies of ≥10 μJ at most wavelengths.

The maximum input power of the fundamental is typically set between $8 - 12$ μJ per pulse using neutral density filters. During experiments, the input power is further modulated by a rotating circular variable neutral density filter operating at 1 Hz. Input polarization is controlled by a half-wave plate and polarizer. A beam sampler directs 1 % of the input beam into a photodiode to

measure a reference intensity. A 10 cm lens focuses the *p*-polarized fundamental beam onto liquid samples at an angle of 60º relative to the sample surface normal. The colinearly reflected fundamental and *p*-polarized SHG signal are collimated with a 10 cm lens, then separated spectrally in series by a dichroic mirror, Pellin-Broca prism, and monochromator (Acton, SpectraPro 2150i). A solar-blind photomultiplier tube (Hamamatsu, R7154PHA) and boxcar integrator (Stanford Research Systems, SR250) serve as the photon counting detector. All sample measurements are normalized to the SHG response of pure water samples taken daily between sample measurements to account for day-to-day fluctuations in the setup. Figure 2.3 depicts the DUV-SHG experimental setup.
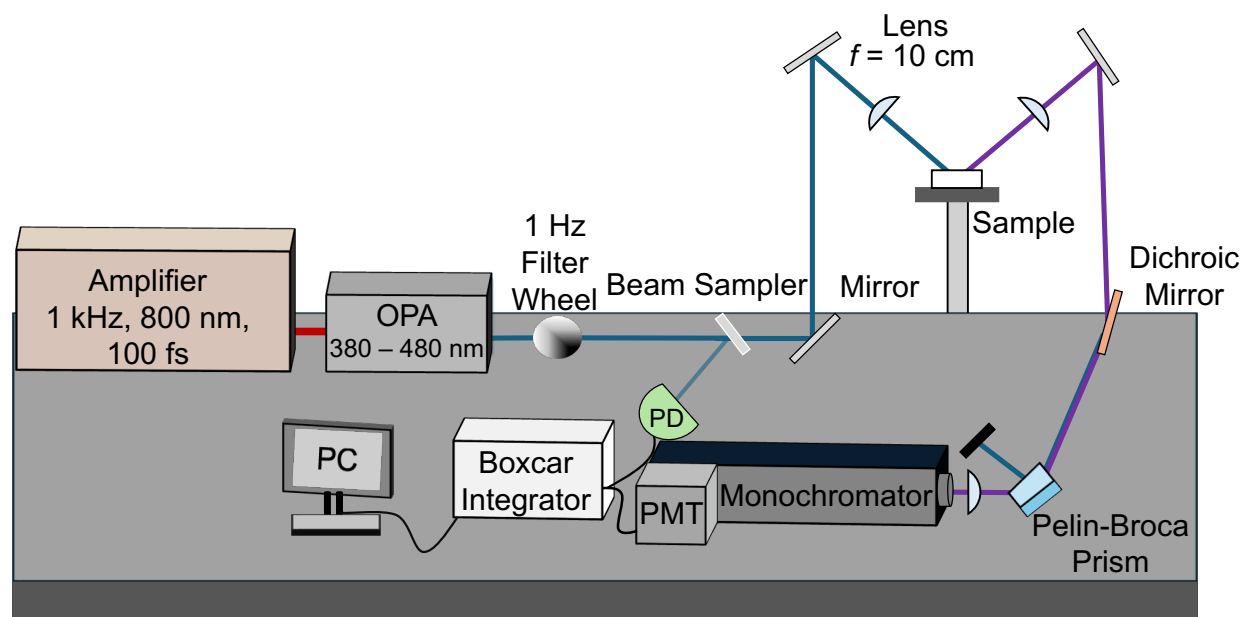
Figure 2.3 Experimental setup for DUV-SHG spectroscopy. For experiments that use a 400 nm fundamental, a BBO crystal is used instead of the OPA.

For all studies presented in this dissertation, salt solutions were prepared on the same day they were tested. All glassware used to prepare solutions is left in an Alnochromix bath for at least 12 hours to ensure trace amounts of organic contaminants. Glassware is thoroughly rinsed with ultrapure water (MilliporeSigma, 18 MΩ) before the addition of chemicals. Solutions are then prepared using more ultrapure water, vigorously shaken, and aged for at least an hour before testing. By allowing the solutions to age before use, we allow trace organic contaminants from unbaked salts to rise to the surface. Disposable borosilicate serological pipettes are used to transfer aliquots of solution from volumetric flasks to rinsed Petri dishes. Solutions are pipetted from the bottom of the flasks to avoid surface contaminants, and for this reason, no more than ¾ of the total volume is used for experiments.

All DUV-SHG measurements reported this dissertation followed a similar protocol. All detector equipment was turned on and allowed to warm up before preparing solutions. Immediately

before testing solutions, all critical parameters of the experimental setup, such as fundamental input power, fundamental center wavelength, data collection time, monochromator settings, and boxcar outputs, are recorded. Laser alignment is checked with a GaAs crystal and a plain water sample. Experiment collection times are set to 3 minutes per sample including reference water scans. Boxcar integrator settings are confirmed to be well-overlapped with the reference and SHG signal, as shown in Figure 2.4. Water and solution scans are taken in alternating fashion. Approximately 12 mL of solution are pipetted into rinsed Petri dishes for measurements, after which a new Petri dish is used for the next solution aliquot.
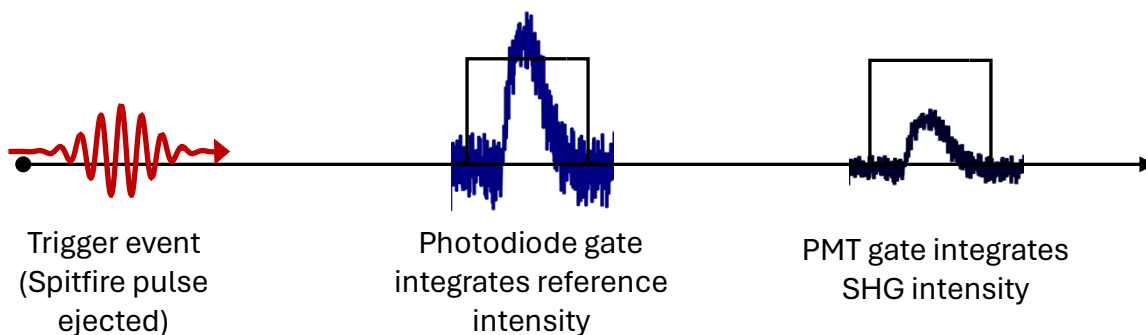
Figure 2.4 Boxcar signal acquisition protocol. The output of the amplifier triggers the gate generator in the boxcar. Gate width and time delay are adjusted to overlap with the reference and SHG intensity signals. Reference and SHG signals require separate boxcar modules.

2.5. Data Analysis

Given the 1kHz repetition rate of our Spitfire amplifier and 3 min collection windows, we record 180,000 photon events per scan, or once each millisecond. From Eq. 2.9, by measuring the SHG intensity via a PMT and the reference intensity via a photodiode, we can calculate the effective second-order susceptibility. To improve statistics in our measurements, we modulate the input power of the fundamental with a rotating neutral density filter and correlate the intensity of each input pulse with the generated SHG pulse. Figure 2.5.A and 2.5.B depict the correlated raw reference and SHG signal intensities, respectively.
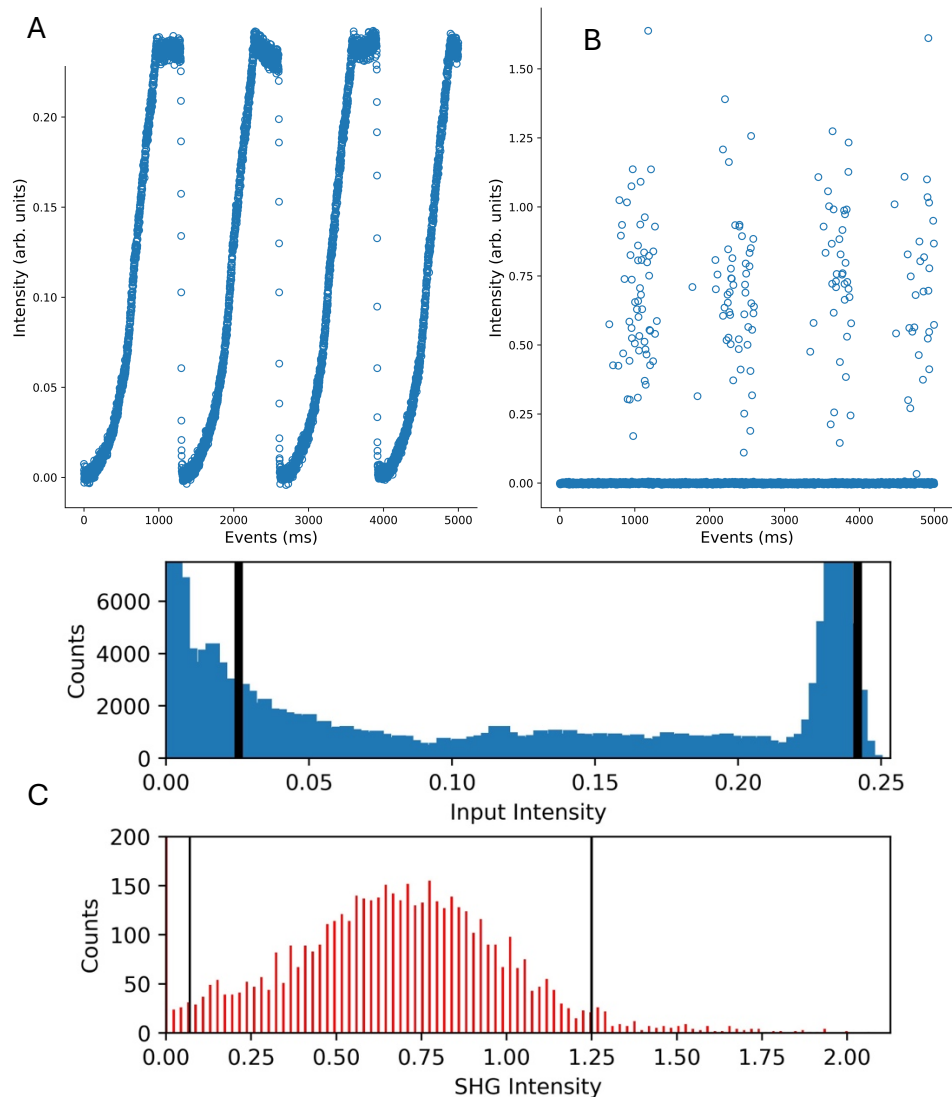
Figure 2.5 SHG signal collection. **A)** Reference channel raw data. Clear oscillations in the intensity are due to the rotating filter modulating the input power. **B)** SHG signal channel raw data. SHG conversion efficiency is weak and is highlighted here, as most of the SHG signal consists of a flat zero response. **C)** Histograms of the reference and SHG photon counts binned by intensity.

After a scan is complete, the reference and SHG data points are binned by intensity. The black bars in Figure 2.5.C indicate cutoffs used to minimize false counts. For each reference intensity bin, we count the number of reference intensity pulses that fit inside the bin width. Since each reference pulse is paired to an SHG signal pulse, we also determine if the paired SHG pulse lies within the histogram bounds. Once we have established the total number of reference and SHG counts in a bin, subtracting the two values tells us the number of zero counts. This is particularly important for Poisson statistics, which we use to determine the expected number of SHG photon counts per bin based on our measurements:

$$P(k = 0) = \frac{\lambda^0 e^{-\lambda}}{0!} = e^{-\lambda} = \frac{N_{pulses}^{k=0}}{N_{pulses}^{total}} \qquad (2.17)$$

$$\lambda = -\ln \frac{N_{pulses}^{k=0}}{N_{pulses}^{total}} \propto I_{2\omega} \qquad (2.18)$$

From the above, the probability that no SHG photon is present in our bin is expressed as the ratio of zero SHG counts ($N_{pulses}^{k=0}$) over the total number of counts (N_{pulses}^{total}) and is related to the exponential of the expected number of SHG counts (λ). Solving for λ we obtain the expected number of SHG counts for each intensity bin, which is directly proportional to the second harmonic intensity $I_{2\omega}$.

After calculating $I_{2\omega}$ at each intensity bin using Poisson statistics, we plot $I_{2\omega}$ vs I_ω^2 as shown in Figure 2.6. A simple linear regression is used to extract the slope of the data, which represents the $\left|\chi_{effective}^{(2)}\right|^2$ of the solution. The magnitude of the slope is dependent on the surface ion concentration and oscillator strength.
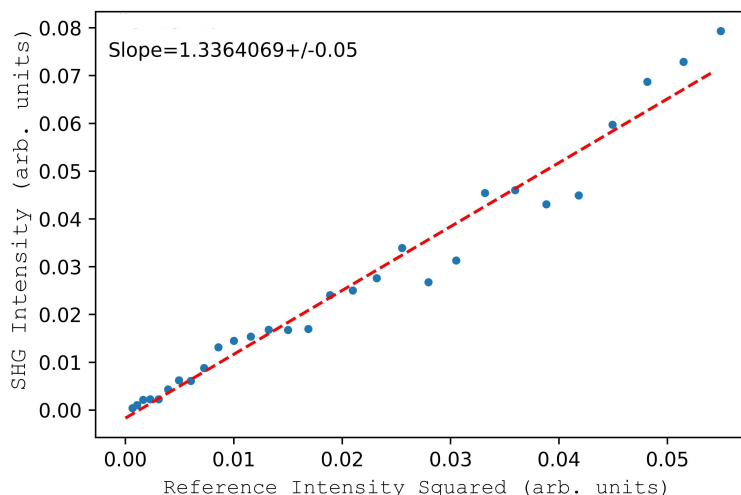
Figure 2.6 Plot of $I_{2\omega}$ vs I_ω^2 used extract the effective susceptibility of the solution through linear regression.

Once an entire concentration range is studied, the SHG response ($I_{2\omega}/I_\omega^2$) is normalized by the response of pure water. The normalized SHG response is plotted against mole fraction of the solution and fit using Eq. 2.16 to extract the Gibbs free energy of adsorption. Figure 2.7 displays a representative fit for an ion with a ΔG_{ads} = -8 kJ/mol. Additional thermodynamic values such as ΔS_{ads} and ΔH_{ads} can be extracted by repeating the above experimental methodology as a function of temperature. Further support from theoretical studies can help elucidate the detailed molecular mechanism by which ions adsorb to the interface.
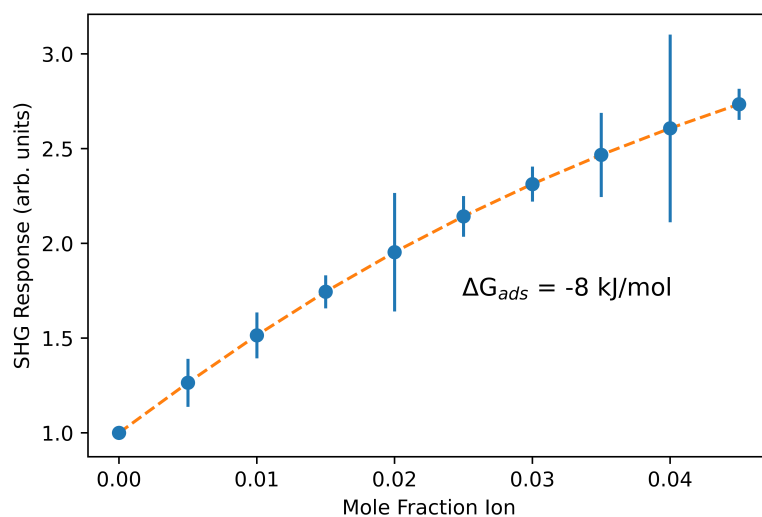
Figure 2.7 Plot of SHG response vs mole fraction for an ion with -8 kJ/mol Gibbs free energy of adsorption. A, B, C parameters from Eq. 2.16 were set to 1 to generate this example.

Most of the data analysis was done in Python using code previously developed in the Saykally group. A detailed description of the specific packages and scripts used was previously outlined by McCaffrey[16].

References
(1)   Maiman, T. H. Stimulated Optical Radiation in Ruby. *Nature* **1960**, *187* (4736), 493–494. https://doi.org/10.1038/187493a0.
(2)   Franken, P. A.; Hill, A. E.; Peters, C. W.; Weinreich, G. Generation of Optical Harmonics. *Phys. Rev. Lett.* **1961**, *7* (4), 118–119. https://doi.org/10.1103/PhysRevLett.7.118.
(3)   Heinz, T. F. Chapter 5 - Second-Order Nonlinear Optical Effects at Surfaces and Interfaces. In *Modern Problems in Condensed Matter Sciences*; Ponath, H.-E., Stegeman, G. I., Eds.; Nonlinear Surface Electromagnetic Phenomena; Elsevier, 1991; Vol. 29, pp 353–416. https://doi.org/10.1016/B978-0-444-88359-9.50011-9.
(4)   Boyd, R. W. *Nonlinear Optics, Third Edition*, 3rd ed.; Academic Press, Inc.: USA, 2008.
(5)   Shen, Y. R. Optical Second Harmonic Generation at Interfaces. *Annu. Rev. Phys. Chem.* **1989**, *40* (1), 327–350. https://doi.org/10.1146/annurev.pc.40.100189.001551.
(6)   Shen, Y. R. *Fundamentals of Sum-Frequency Spectroscopy*; Cambridge University Press: Cambridge, 2016. https://doi.org/10.1017/CBO9781316162613.
(7)   Moad, A. J.; Simpson, G. J. A Unified Treatment of Selection Rules and Symmetry Relations for Sum-Frequency and Second Harmonic Spectroscopies. *J. Phys. Chem. B* **2004**, *108* (11), 3548–3562. https://doi.org/10.1021/jp035362i.
(8)   Petersen, P. B.; Saykally, R. J. ON THE NATURE OF IONS AT THE LIQUID WATER SURFACE. *Annu. Rev. Phys. Chem.* **2006**, *57* (1), 333–364. https://doi.org/10.1146/annurev.physchem.57.032905.104609.

(9)   Petersen, P. B.; Saykally, R. J.; Mucha, M.; Jungwirth, P. Enhanced Concentration of Polarizable Anions at the Liquid Water Surface: SHG Spectroscopy and MD Simulations of Sodium Thiocyanide. *J. Phys. Chem. B* **2005**, *109* (21), 10915–10921. https://doi.org/10.1021/jp050864c.

(10)   Mason, P. E.; Neilson, G. W.; Enderby, J. E.; Saboungi, M.-L.; Dempsey, C. E.; MacKerell, A. D. Jr.; Brady, J. W. The Structure of Aqueous Guanidinium Chloride Solutions. *J. Am. Chem. Soc.* **2004**, *126* (37), 11462–11470. https://doi.org/10.1021/ja040034x.

(11)   Viswanath, P.; Motschmann, H. Oriented Thiocyanate Anions at the Air−Electrolyte Interface and Its Implications on Interfacial Water - A Vibrational Sum Frequency Spectroscopy Study. *J. Phys. Chem. C* **2007**, *111* (12), 4484–4486. https://doi.org/10.1021/jp0702649.

(12)   Petersen, P. B.; Saykally, R. J. Probing the Interfacial Structure of Aqueous Electrolytes with Femtosecond Second Harmonic Generation Spectroscopy. *J. Phys. Chem. B* **2006**, *110* (29), 14060–14073. https://doi.org/10.1021/jp0601825.

(13)   Eckenrode, H. M.; Jen, S.-H.; Han, J.; Yeh, A.-G.; Dai, H.-L. Adsorption of a Cationic Dye Molecule on Polystyrene Microspheres in Colloids: Effect of Surface Charge and Composition Probed by Second Harmonic Generation. *J. Phys. Chem. B* **2005**, *109* (10), 4646–4653. https://doi.org/10.1021/jp045610q.

(14)   Castro, A.; Bhattacharyya, K.; Eisenthal, K. B. Energetics of Adsorption of Neutral and Charged Molecules at the Air/Water Interface by Second Harmonic Generation: Hydrophobic and Solvation Effects. *J. Chem. Phys.* **1991**, *95* (2), 1310–1315. https://doi.org/10.1063/1.461113.

(15)   Ng, K. C.; Adel, T.; Lao, K. U.; Varmecky, M. G.; Liu, Z.; Arrad, M.; Allen, H. C. Iron(III) Chloro Complexation at the Air–Aqueous FeCl3 Interface via Second Harmonic Generation Spectroscopy. *J. Phys. Chem. C* **2022**. https://doi.org/10.1021/acs.jpcc.2c02489.

(16)   McCaffrey, D. L. Deep UV Second Harmonic Generation Studies of Thiocyanate at Hydrophobe/Water Interfaces, UC Berkeley, 2016. https://escholarship.org/uc/item/852659pr (accessed 2022-01-14).

Chapter 3 – Strong Adsorption of Guanidinium Cations to the Air-Water Interface

The following is adapted from F. Bernal, A. Dodin, C. Kyprianou, D. T. Limmer, R. J. Saykally, "Adsorption of Guanidinium Cations to the Air-Water Interface". (2024). arXiv:2408.15423

3.1. Introduction

Chemistry at aqueous interfaces underlies vital applications ranging from electrochemistry and catalysis to biological membrane processes and atmospheric aerosol reactions.[1–3] Characterizing the detailed behavior of ions at aqueous interfaces is thus critical in advancing our fundamental understanding of many phenomena. The study of ions at the air-water interface has undergone dramatic evolution since the early theoretical work of Onsager and Samaras exploited electrostatic arguments to describe the air-water interface as being devoid of ions.[4] Under classical electrostatic theory, the boundary between two dielectric media of dissimilar permittivity (e.g. air-water) engenders an image charge repulsion for solvated ions from the medium of lowest dielectric constant, therefore excluding all ions from the first few outermost water layers of an air-water or hydrocarbon-water interface.[5] However, studies have challenged the completeness of this description with the observation of several anions at the air-water interface and have rigorously established the mechanistic details driving this ion adsorption.[6–9] When an ion comes within a few water layers of the interface, the continuum picture of Onsager and Samaras begins to break down. At these length scales, the thermodynamics of ion adsorption increasingly reflects the molecular rearrangements of the solvent required to accommodate it rather than the polarization of a continuous dielectric medium. Surface active anions, which can be bulky, and highly polarizable, with solvation cavities that do not fit naturally into bulk water structure, are more easily accommodated at the interface than in the bulk. While most cations do not share these properties, and therefore do not adsorb to the interface, we show by establishing the surface activity of the guanidinium cation, that the same molecular picture of interfacial anions can also lead to cation adsorption.

Second-order nonlinear spectroscopic techniques, like second harmonic generation (SHG) and sum frequency generation (SFG), have emerged as powerful tools for studying interfacial ions, given their inherent surface specificity.[10,11] These techniques have now been used to establish the interfacial presence of anions such as I^-, N_3^-, and SCN^- in both aqueous solutions and hydrocarbon solutions.[12–18] It has been generally concluded that large, singly charged, weakly hydrated, and highly polarizable anions exhibit surface enrichment at the air-water interface. However, recent studies have prompted a reassessment of this simple picture. X-ray photoelectron spectroscopy (XPS) and SHG results have shown that the doubly-charged CO_3^{2-} ion exhibits a strongly increased propensity for the air-water interface relative to singly-charged HCO_3^-.[9,19] Cation co-solutes are

typically less polarizable, better solvated, and thus are expected to be excluded from the interface.[20] However, XPS measurements on LiI solution liquid jets by Perrine et al. uncovered a surprising surface activity of the Li^+ cation, a behavior that was not found for K^+ in KI solutions.[21] Ng et al. used UV-VIS SHG measurements to study various ferric chloride complexes at the air-water interface.[22] These authors use symmetry and resonance arguments to attribute their SHG signal to the neutral complexes $[FeCl_3(H_2O)_x]$, residing at the interface. These results highlight the fact that our understanding of ions at the air-water interface is still evolving. In the present study, we provide both theoretical and nonlinear spectroscopic evidence for an important surface-active molecular *cation.*

We consider the guanidinium cation, (Gdm^+), a powerful protein denaturant widely employed in protein stability studies.[23] Several theoretical reports have investigated its surface activity, given its position within the Hofmeister series, it exhibits similarities to well-known surface-active anions.[24–30] XPS measurements on aqueous guanidinium chloride and ammonium chloride solutions found a greater interfacial population of Gdm^+ relative to NH_4^+, indicated by photoemission signals more than four times higher for Gdm^+.[29] While XPS provides atom specificity, the technique itself is ambiguous regarding probe depth. Here we employ interface-specific SHG spectroscopy in the deep-UV (DUV-SHG) to directly probe Gdm^+ at the air-water interface, sampling solutions of guanidinium chloride (GdmCl). This enables us to minimize signal contribution from ions in the bulk, and by studying a series of concentrations, we can extract thermodynamic information. These experiments are highly sensitive and allow us to track small changes in SHG intensity with respect to bulk ion concentration, allowing us to fit SHG intensity to a Langmuir model and extract the Gibbs free energy of adsorption (ΔG_{ads}) for Gdm^+. We find a notable similarity between the ΔG_{ads} values for Gdm^+ and SCN^- at the air-water interface. Simulations are used to clarify the molecular origins of this strong driving force for adsorption and to provide further structural details on the solvation of Gdm^+ at the air-water interface.

3.2. Methods

3.2.1. Sample Preparation

All glassware was left overnight in a bath of Alnocromix (Alconox Inc) and concentrated sulfuric acid (Sigma Aldrich) to remove organic debris, then rinsed with ultrapure 18.2 MΩ water (Millipore MilliQ) before use. The salts GdmCl (Sigma Aldrich, >98% purity), NaCl (Sigma Aldrich, > 99% purity), and NaSCN (Sigma Aldrich, >98% purity) were used as is with ultrapure water to make stock solutions. NaCl solutions were pH adjusted using reagent grade HCl (Sigma Aldrich). Aliquots of each solution were drawn from the bottom of stocks using borosilicate serological pipettes to avoid organics on the surface and deposited into Petri dishes immediately before measurement.

3.2.2. Experimental Design

The laser setup has been described previously. Briefly, the output of a Ti-Sapphire amplifier (Spectra Physics Spitfire Ace, 2 mJ, 1 kHz, 100 fs) centered at 800 nm is directed through a type-I beta barium borate (Edmund Optics, β-BBO) crystal to produce the fundamental 400 nm beam. For measurements at fundamental wavelengths below and above 400 nm, the 800 nm output is directed into an optical parametric amplifier (TOPAS Prime). Input power is modulated by a rotating circular variable neutral density filter operating at 1 Hz and input polarization is controlled by a half-wave plate and polarizer. A 10 cm lens focuses the *p*-polarized fundamental beam onto liquid samples at an angle of 60° relative to the sample surface normal. The colinearly reflected fundamental and *p*-polarized SHG signal are collimated with a 10 cm lens then separated spectrally in series by a dichroic mirror, Pellin-Broca prism, and monochromator (Acton, SpectraPro 2150i). A solar-blind photomultipler tube (Hamamatsu, R7154PHA) and boxcar integrator (Stanford Research Systems, SR250) serve as the photon counting detector. All sample measurements are normalized to the SHG response of pure water samples taken daily between sample measurements to account for day-to-day fluctuations of the setup. Bulk UV-Vis measurements were made using a Shimadzu UV-2600 spectrometer.

3.3. Results and Discussion

3.3.1. Bulk Absorption Spectroscopy

The bulk UV absorption spectrum of GdmCl (black trace) and NaCl (green trace) in water are shown in Figure 3.1. The charge-transfer-to-solvent (CTTS) transition of Cl$^-$ has been previously characterized, with a peak centered near ca. 180 nm.[31,32] Antol et al. theoretically calculated the UV spectrum of Gdm$^+$ and found a strongly absorbing π-π* transition in the DUV region.[33] Pointwise DUV-SHG measurements taken at various wavelengths for 3 M GdmCl solutions were normalized to pure water and plotted relative to the maximum intensity (black squares) in Figure 3.1. A steady increase in SHG signal is seen from 220 – 200 nm, matching the low energy shoulder of the bulk absorption spectrum. It is difficult to generate a precise interfacial spectrum via SHG due to the nature of the technique, which relies on single wavelength measurements.
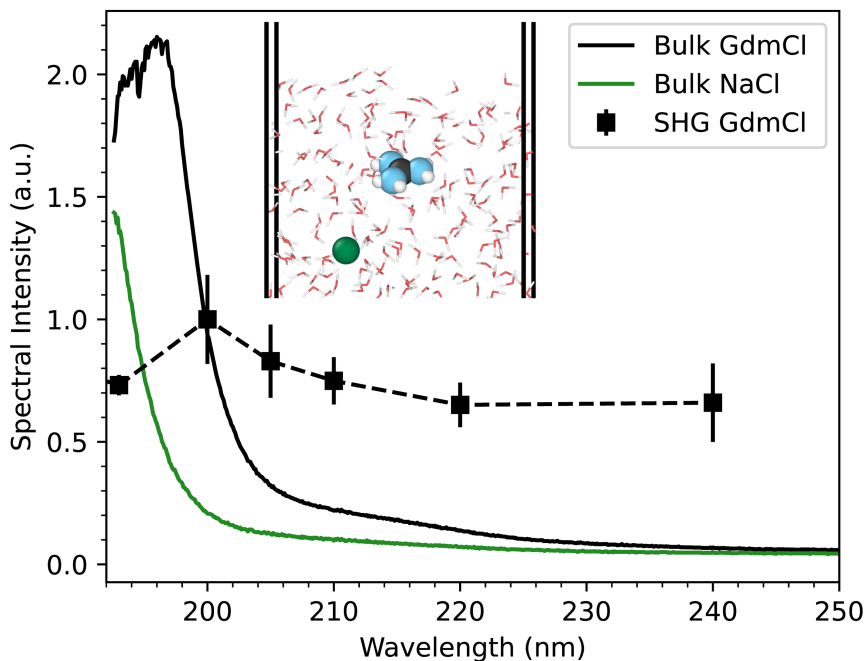
Figure 3.1 DUV absorption spectra of bulk GdmCl (black trace) and NaCl (green trace) solutions. The π-π* transition of Gdm^+ is clearly visible along with the onset of the Cl^- charge-transfer-to-solvent (CTTS) transition. SHG response of 3 M GdmCl (black squares), normalized to pure water at varying SHG wavelengths, is shown joined with a dashed line serving as a guide to the eye. (Inset) Snapshot from MD Simulation showing GdmCl near a liquid-vapor interface.

Many of the anions studied by DUV-SHG have strong CTTS transitions with large molar absorption coefficients (ε) in the 10^2 - 10^4 $M^{-1}cm^{-1}$ range[31], making them ideal candidates for resonant signal enhancement. SHG studies have shown that these transitions may shift by ca. 5 - 20 nm at the interface relative to the bulk, a result of the sensitivity of CTTS transitions to a chromophore's local solvation environment.[13,14,34,35] At 200 nm, the molar absorption coefficient of Gdm^+ was much larger than that of Cl^-, viz. ε= 375 vs 59 $M^{-1}cm^{-1}$, respectively. Previous DUV-SHG studies reported a low average SHG response for pure NaCl solutions across the 200 – 225 nm wavelength range.[12] This indicates that we should expect negligible resonant signal enhancement at these wavelengths due to the Cl^- CTTS transition. Our DUV-SHG experiments were conducted with a 400 nm input (200 nm SHG) wavelength, where resonant signal enhancement contributions are primarily due to the Gdm^+ $π-π^*$ transition.

3.3.2. Langmuir Adsorption Model

A Langmuir adsorption model is used to extract the Gibbs free energy of adsorption from concentration-dependent DUV-SHG intensities. Although modified adsorption models are not uncommon in literature for fitting SHG intensities[22,36,37], a Langmuir model proves to be the simplest and fits the data presented here well. A thorough discussion of the Langmuir model used in SHG studies can be found elsewhere[12,13] and in Chapter 2; here only a brief description is provided.

DUV-SHG is a second-order nonlinear optical process and under the electric dipole approximation, signal from the centrosymmetric bulk environment is forbidden and quadrupole and magnetic dipole contributions are assumed negligible.[10,38] Thus, the signal generated from DUV-SHG arises from the few outermost molecular layers where inversion symmetry is broken, typically expected to be 1 nm depth. By tuning the input energy so that the generated second harmonic field is resonant with an electronic transition of a chromophore, we gain signal enhancement and directly probe the number of interfacial chromophores. The intensity of the second harmonic signal ($I_{2\omega}$) is proportional to the second order nonlinear susceptibility of the interfacial species ($\chi^{(2)}_{water}, \chi^{(2)}_{Gdm^+}$) and the squared intensity of the driving field ($I_\omega{}^2$):

$$I_{2\omega} \propto \left| \chi^{(2)}_{water} + \chi^{(2)}_{Gdm^+} \right|^2 \times I_\omega{}^2 \tag{3.1}$$

Nonlinear susceptibilities become complex quantities when resonant with a transition. At the frequencies used here, $\chi^{(2)}_{water}$ is non-resonant and real, but $\chi^{(2)}_{Gdm^+}$ is resonant and therefore a complex quantity with both real and imaginary components. Nonlinear susceptibilities can be described as an ensemble of molecular hyperpolarizabilities, i.e. the degree to which each molecule responds to a driving electric field:

$$\chi^{(2)}_{Gdm^+} = \sum_i \beta_i = N_s \times \langle \beta \rangle_{orient.} \tag{3.2}$$

Which is further denoted as the product between the number of molecules (N_s) and their orientationally averaged hyperpolarizability ($\langle \beta \rangle_{orient.}$). It is assumed that the magnitude of $\langle \beta \rangle_{orient.}$ remains constant during the experiment and therefore that the orientations of the interfacial molecules remain unperturbed by ion-ion interactions as the bulk concentration changes. Vibrational SFG studies on the orientation of SCN⁻ found that the linear molecule remains tilted at 44° from surface normal at the air-water interface between a wide range of molar concentrations.[39] Similarly, simulations show that Gdm⁺ preferentially adsorbs to the interface in a single orientation with minimal fluctuation, and is independent of bulk concentration.[25,40] Thus, changes in the SHG signal become directly proportional to the number of surface molecules adsorbing to the interface, and this permits the use of a Langmuir adsorption model:

$$\frac{I_{2\omega}}{I_\omega^2} = \left(A + B \frac{X_{Gdm+}}{(1-X_{Gdm+})e^{\frac{\Delta G}{RT}} + X_{Gdm+}} \right)^2 + \left(C \frac{X_{Gdm+}}{(1-X_{Gdm+})e^{\frac{\Delta G}{RT}} + X_{Gdm+}} \right)^2 \qquad (3.3)$$

where A represents the real water susceptibility, and B and C are the real and imaginary contributions to the Gdm^+ susceptibility, respectively. SHG intensities are fit using Eq. 3.3 and allowing A, B, and C, to vary when extracting the Gibbs free energy of adsorption (ΔG_{ads}). A full derivation of Eq. 3.3 can be found in Chapter 2.

3.3.3. DUV-SHG

SHG intensities of NaCl solutions normalized to pure water are plotted against bulk concentration in Figure 3.2. The pH of NaCl solutions was adjusted to the pH of GdmCl solutions at each respective concentration via HCl. A weak linear response in SHG intensity with electrolyte concentration is seen here. This response has been previously attributed to an interfacial thickening of the water layer.[41] As the bulk concentration of the solution increases, interfacial water molecules rearrange, effecting a change in their hyperpolarizability resulting in a linear increase in the SHG intensity, normalized to neat water. Attempts to fit the data in Figure 3.2 to Eq. 3.3 were unsuccessful as it does not conform to a typical adsorption pattern. Although we expect to be off-resonance with the Cl^- CTTS transition, ions adsorbing to the interface should still elicit changes in the SHG response as the interfacial concentration increases, as noted in other non-resonant SHG studies.[41,42] Since we observe a predominantly flat response from pH-adjusted NaCl solutions, we suspect that the chloride anion resides beyond the probe depth of our DUV-SHG measurements.
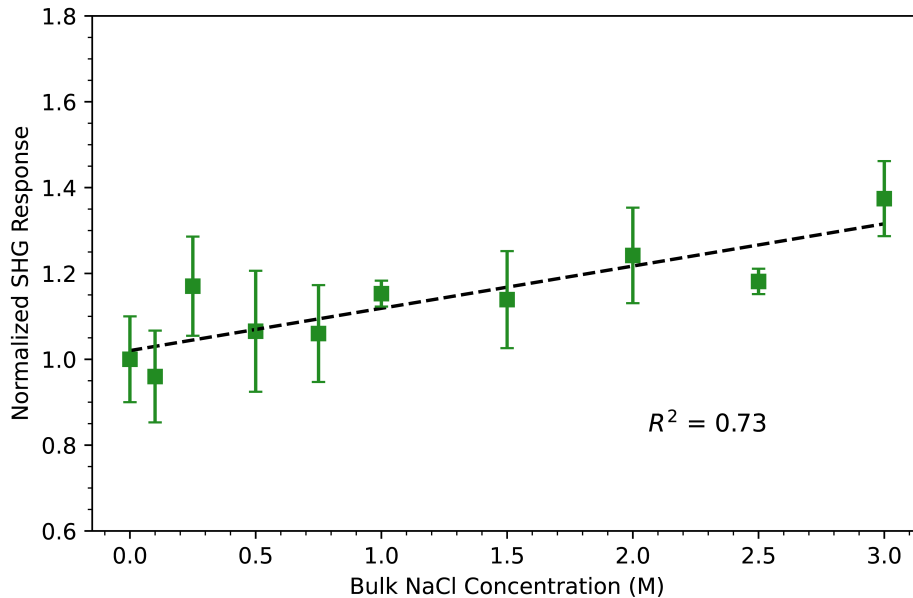
Figure 3.2 SHG response (ω_{SHG} = 200 nm) of pH-adjusted NaCl solutions normalized to pure water plotted against bulk concentration. The dashed line represents a linear fit with an R^2 = 0.73 and serves as a guide to the eye.

The results in Figure 3.2 are unsurprising, since it has been demonstrated before that the chloride anion exhibits a weak surface-affinity for the air-water interface compared to larger halides. This is evidenced by density profile plots of Cl⁻ lacking a large population increase at the interface[43] and by SHG studies reporting a weak response from pure NaCl solutions[12]. Recently, Seki et al. reported heterodyne-detected SFG measurements that quantified a salting-out effect that Cl⁻ induces on co-solvated anions such as SCN⁻.[44] Their work finds a maximum 50% increase in the surface population of known surface-active anions after the addition of NaCl. This effect is attributed to Cl⁻ exhibiting hydrophilic character in solution, thereby residing mainly in the bulk and promoting a greater number of hydrophobic anions to the interface.
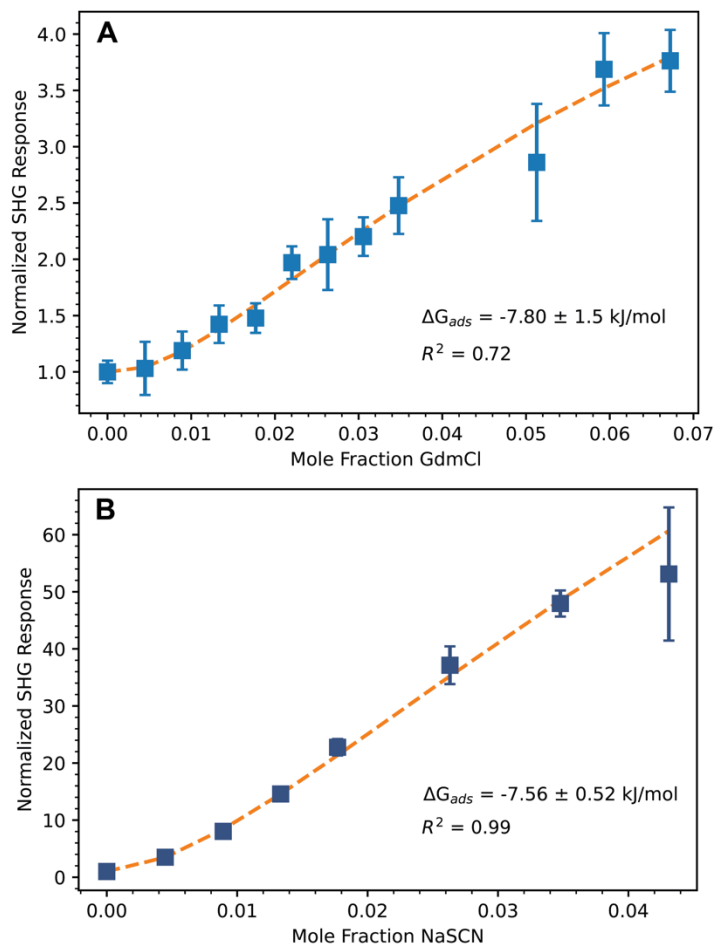
Figure 3.3 Comparison of interfacial adsorption for cations and anions at the air-water interface. **A**) Normalized DUV-SHG response ($\omega_{SHG} = 200$ nm) of GdmCl solutions at the air-water interface (blue squares) plotted against bulk concentration. Data are fit to a Langmuir adsorption model (orange dashed line) with an extracted Gibbs free energy of -7.8 ± 1.54 kJ/mol. **B**) Normalized SHG intensity ($\omega_{SHG} = 200$ nm) for NaSCN solutions at the air-water interface (dark-blue squares)

plotted against bulk concentration. Data are fit to a Langmuir adsorption model (orange dashed line) with an extracted Gibbs free energy of -7.56 ± 0.52 kJ/mol. Uncertainties reported are one σ.

Figure 3.3.A shows the SHG intensities of GdmCl solutions normalized to the pure water response and plotted with respect to bulk concentration. There is a clear signal dependance on concentration that was not seen for NaCl solutions, which we attribute to the presence of Gdm^+ at the interface. For comparison, we have also reexamined the prototypical SCN^- anion via DUV-SHG in Figure 3.3.B. The maximum normalized SHG response is relatively low for Gdm^+ compared to SCN^-. Analyzing the SHG response in Figure 3.1, the signal at the resonant wavelength is only 1/3 greater than the off-resonance signal, likely due to the π-π^* transition contributing minimal signal enhancement. Spectral shifts in the resonant transition can affect the SHG intensity; however, as noted above, there is no obvious shift in the peak Gdm^+ SHG response compared to the bulk absorption.

Investigating the parameters generated from fitting SHG intensities to Eq. 3.3, we find that both systems share similar A values, as expected, since it is due to the real water response. However, the B and C parameters, which are due to the ion resonances, differ between the two systems, with both parameters being lower for Gdm^+. Examining the magnitude of the susceptibility of both ions ($\sqrt{B^2 + C^2}$), we find the net $\chi^{(2)}_{Gdm^+}$ to be 82 % less than $\chi^{(2)}_{SCN^-}$, as reflected in the SHG intensities plotted in Figure 3.3. We recognize that these fit parameters were extracted for studies at a single resonant wavelength and that a more rigorous approach in determining the resonant and non-resonant ion contributions involves additional concentration dependent measurements at off-resonant wavelengths. Given the already low resonant SHG response of Gdm^+, tracking the off-resonance response would prove challenging, given our current sensitivity, and would likely be better suited to heterodyne-detected methods. Irrespective of this, we can clearly discern changes in the resonant SHG signal with GdmCl concentration, hence our fit to a Langmuir model strongly-supports previous studies concluding that Gdm^+ resides at the air-water interface.[28,29]

Despite the order of magnitude difference in SHG oscillator strength between both systems, the extracted ΔG_{ads} for both ions are surprisingly within error. The Gibbs free energy of adsorption for SCN^- at hydrophobe-water interfaces has been extensively measured by DUV-SHG experiments and is well-reproduced here for the air-water interface using a 400 nm incident wavelength (ΔG_{ads} = -7.56 ± 0.52 kJ/mol). For Gdm^+ ions, this study produced ΔG_{ads} = -7.80 ± 1.5 kJ/mol, indicating that both ions share a similar propensity for adsorbing to the interface. These ions are two well-studied protein denaturants that are situated on the far-chaotropic end of the Hofmeister series[45], and therefore might be expected to exhibit similar ion effects and properties in water. Litman et al. recently reported strong perturbations in the vibrational SFG water O-H signal with increasing perchlorate concentration, an effect they expect to extend to SCN^- and other chaotropic ions.[46] The recently reevaluated hydration free energy of Gdm^+ is -328 kJ/mol, a value 35 kJ/mol larger than that for SCN^-.[47,48] In solution, both monovalent ions achieve stability through charge delocalization, engendering 'soft' ion character. Given the similarities between these ions,

it begs the question: Would the properties of each ion, including the ΔG_{ads}, differ if both ions were co-solvated in water? Balos et al. examined the interaction of Gdm^+ and SCN^- with a model amide, and observed competing interactions between the two ions in solution.[49] The overall ion-amide interaction rotational effects were non-additive for GdmSCN, implying that individual SCN^--amide and Gdm^+-amide interactions were not compounded when both ions were present in solution, indicating a contest between both ions for the amide. Signal from DUV-SHG measurements of GdmSCN solutions would likely be dominated by SCN^- ions and lack a straightforward route to deconvoluting the respective signal contributions.

3.3.4. Molecular Dynamics

In order to gain molecular insight into the driving forces for Gdm^+ adsorption, we performed molecular dynamics simulations with the LAMMPS software package.[50] All simulations were performed in an ensemble with fixed number of particles, temperature, and volume, using a Langevin thermostat at 300 K and a relaxation time of 200 fs, and in a periodic 18.5 Å X 18.5Å X 130 Å simulation cell. All simulations contained 450 water molecules and a variable number of GdmCl ion pairs in a slab geometry with a large vapor region in the z direction. Simulations with a larger simulation cell demonstrate that this relatively small simulation is sufficient to avoid significant finite size artifacts in the Gdm surface adsorption. GdmCl ions were modeled using a previously parametrized force field.[23] To prevent the global translation of the slab in the z direction, the center of mass is subject to a harmonic constraint at $z_{CoM} = 0$. Water was modeled using the non-polarizable tip4p/2005 model[51], the polarizable swm4-ndp model (denoted Drude) which employs Drude oscillators to explicitly capture water polarizability[52–54], and a hybrid water model that adds a Drude oscillator to the tip4p/2005 model (denoted tip4p/drude). This hybrid water model is artificially constructed to increase the cohesive interactions between water molecules in the swm4-ndp (Drude) water model, effectively decreasing the temperature of the simulation. Drude oscillator simulations were performed using the LAMMPS DRUDE package, with a dual Langevin thermostat fixing the temperature of fictitious Drude particles to 1K with a relaxation time of 100 fs and a timestep of 1 fs. Symmetrized Drude force fields were used to improve numerical stability.[55] Non-polarizable simulations were performed with a timestep of 2 fs. Water molecules were held rigid using the symplectic rigid body integrator in the LAMMPS RIGID package.[56]
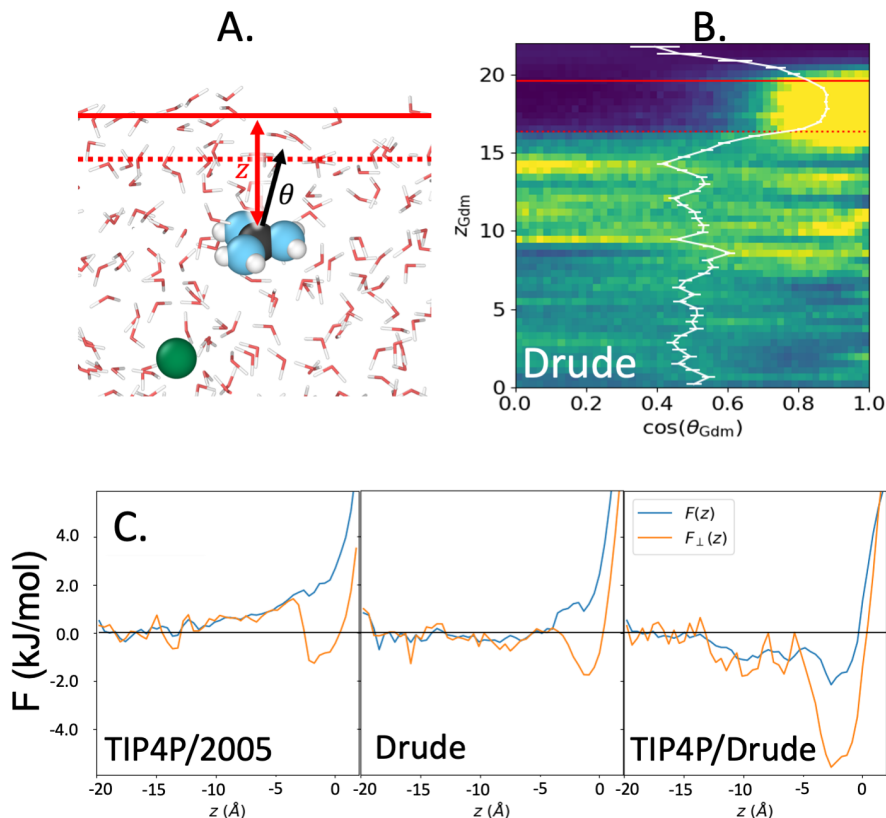
Figure 3.4 Molecular dynamics simulations of GdmCl with varying water models. **A)** MD Snapshot showing the definition of z and θ. **B)** Orientation histogram of Gdm^+ in explicitly polarizable water as a function of distance from the Gibbs dividing surface (solid red line). The dashed red trace indicates the boundary of the subsurface layer. The white trace shows the average orientation as a function of z. **C)** Potentials of mean force of Gdm^+ ions approaching the liquid-vapor interface in the dilute limit for three models for water polarizability – the TIP4P/2005 model, the Drude SWM4-NDP, and a hybrid model adding a Drude Oscillator to the TIP4P/2005 water model. The PMF's averaging over all orientations of the Gdm^+ cation are shown in blue, while the orange traces show the PMF's conditioned on Gdm^+ approaching coplanar to the interface.

Potentials of mean force (PMF's) are constructed using an umbrella sampling scheme[57] in which the Gdm^+ ions are subject to a series of harmonic bias potential $U_{bias} = \frac{k}{2}(z - z_0)^2$. Drude oscillator simulations were performed using 51 Umbrella windows, spaced 0.5 Å apart in the interval 0 Å < z < 25 Å with spring constants of 10 kCal/mol/Å². Non-polarizable simulations were performed using 18 windows spaced 1 Å apart in the interval 0 Å < z < 18 Å with k = 2.5 kCal/mol/Å², and 9 windows spaced 0.5 Å apart in the interval 18 Å < z < 22 Å with k = 1 kCal/mol/Å². All umbrella simulations were equilibrated for 500 ps with a production run of 4 ns. In all cases, the Gibbs dividing surface was at approximately z = 20 Å. Biased simulations were then reweighted into the unbiased ensemble using the Grossfield implementation[58] of the Weighted

Histogram Analysis method[59–61] with 50 equally spaced bins in the range 0 Å < z < 23 Å for non-polarizable simulations and the range 0 Å < z < 25 Å for Drude oscillator simulations.

The PMF of Gdm^+ in the dilute limit relevant to the Langmuir isotherm is shown in Figure 3.4.C as a function of distance from the average interface, defined as the Gibbs dividing surface where the density falls to half its bulk value. In stark contrast to our spectroscopic measurements, the non-polarizable tip4p water models predicts that the Gdm^+ is repelled more than a nm away from the interface. Accounting for the explicit polarizability of water using the Drude model mitigates this effect, repelling the cation only from the subsurface layer ~3 Å from the Gibbs dividing surface. The only model that predicts an interfacial enhancement of Gdm^+ is the fictitious tip4p/Drude model that overestimates cohesive water interactions with a ΔG_{ads} = -3.59 ± 0.17 kJ/mol.

However, the SHG spectra do not probe the total interfacial concentration of Gdm^+ cations. Instead, they probe the subpopulation of cations that break inversion symmetry by taking on a specific orientation. To investigate the subpopulation of Gdm^+ cations that contribute to the SHG signal, we also calculate how the orientational distribution of the planar Gdm^+ cation changes near the interface's broken symmetry. In Figure 3.4.B, we consider the joint probability distribution of the angle between the normal vector to the Gdm^+ plane and the normal of the interface, and its distance to the average interface, for the Drude water model. In all three water models, we see that a strong orientational bias emerges in the subsurface layer, where the ions lie coplanar with the interface. In this subsurface layer, the cation remains fully solvated, with a single water molecule between it and the gas phase. In contrast to the PMF where the repulsion or attraction to the interface extends for over a nanometer, the orientational bias is strongly localized within the subsurface layer. Below this subsurface layer, the orientation of Gdm^+ cations is isotropic and will contribute nothing to the SHG signal. Therefore, the SHG experiment is not probing all Gdm ions but rather only those that are coplanar to the interface. This is consistent with a previous simulation study of GdmCl that predicted a repulsion of Gdm^+ from the liquid-vapor interface, and proposed that any surface enhancement of Gdm^+ must be attributed to specific orientations of the ion near the interface.[25] The PMF for this coplanar sub-population can be computed as the conditional PMF, $F_\perp(z) = -kT \log\left[\int_{0.8}^{1} d\cos\theta\ P(z, \cos\theta)\right]$ and is plotted for each water model as the orange traces in Figure 3.4.C. These coplanar conditional PMF's predict a surface enhancement of Gdm^+ for all three water models with ΔG_{ads}~ 1 kJ/mol, 2 kJ/mol and 5 kJ/mol for the tip4p/2005, Drude and tip4p/Drude water models respectively. While these results are qualitatively consistent with experiment, and allow us to identify the population of Gdm^+ responsible for the SHG signal, the physical tip4p/2005 and Drude water models underestimate the magnitude of this surface adsorption.

At the interface, where molecules tend to be poorly solvated relative to the bulk, the most energetically favorable configuration of Gdm^+ is that wherein its face is normal to the air-water boundary.[40] This orientational preference was rationalized by considering the weakly hydrated faces of the planar Gdm^+ and the location of its hydrogen bonding N-H groups in the molecular plane. Bulk density profiles for Gdm^+ in solution evidence only a small percentage of cations at

the interface, a result of the strong interfacial orientational preference excluding all but a single Gdm$^+$ orientation.[25] Since $\chi^{(2)}_{Gdm+}$ is dependent on the interfacial density of ions and their hyperpolarizabilities, we speculate that there is a probable low interfacial concentration of Gdm$^+$ at the interface contributing to the signal intensity. This reasoning also fits with surface tension measurements of GdmCl solutions, which indicate that ions should be net depleted from the interface, and indeed only a small subpopulation of Gdm$^+$ demonstrates an affinity for the interface.[62] Thus, the ΔG_{ads} extracted from experiment is a result of probing only a small percentage of specifically oriented Gdm$^+$ that at high concentrations exhibit ion-ion correlations. The lack of quantitative agreement between computational and experimental predictions of ΔG_{ads} may then arise due to a breakdown in the assumptions of the Langmuir model for correlated electrolytes. By introducing an interaction energy parameter, the Frumkin-Fowler-Guggenheim (FFG) isotherm accounts for lateral interactions between the adsorbates. We applied an FFG model to the DUV-SHG data of GdmCl as outlined in previous works.[12,22] We find that the FFG model results in a similar ΔG_{ads} (ca. - 8 kJ/mol) as the Langmuir model along with a small interaction energy of ca. ± 1 kJ/mol which suggests ion-ion effects are indeed present. Although the use of a Langmuir model may seem unsuitable for this system, it appears to fit the DUV-SHG data as well as the more complex FFG model. Further studies aimed at experimentally elucidating the nature of the ion-ion correlations and their effect on SHG signal may be critical to bridging our theoretical and experimental results.

.

3.4. Conclusions

Using DUV-SHG spectroscopy, we provide the first direct experimental evidence for a polyatomic *cation* adsorbing to the air-water interface. By fitting concentration-dependent SHG data to a simple Langmuir adsorption model, we have determined the Gibbs free energy of adsorption for Gdm$^+$ ions to be -7.80 ± 1.5 kJ/mol (one sigma uncertainty). We highlight that this ion appears to adsorb to the interface just as strongly as does the prototypical chaotropic anion, SCN$^-$. The exact underlying mechanistic details of Gdm$^+$ interfacial adsorption remain to be determined, but future studies will undoubtably provide new insight that may even extend to intriguing Gdm$^+$-protein interactions. Our previous work elucidated the mechanism by which SCN$^-$ adsorbs to the air-water interface. We found ions partitioning to the interface to be enthalpically driven via displacement of interfacial water molecules into the bulk, where more favorable hydrogen bonding occurs due to increased coordination, but entropically impeded due to suppression of interfacial capillary waves.[7] It is not unreasonable to suggest that Gdm$^+$ may follow a similar mechanism, but we cannot be certain without further theory and experiments to uncover additional features of Gdm$^+$ ion adsorption (ΔH_{ads}, ΔS_{ads}). Considering that experiments have shown SCN$^-$ adsorbing to both oil-water and graphene-water interfaces with similar ΔG_{ads} to have underlying mechanistic differences,[35] and the publication of new studies highlighting the likelihood of like-charge contact ion-paring of Gdm$^+$ ions in solution,[30,63] we clearly do not yet have a complete description of Gdm$^+$ behavior at the air-water interface. Nevertheless, this work

unambiguously illustrates that cations can also exhibit a strong propensity for the air-water interface.

References

(1)   Ruiz-Lopez, M. F.; Francisco, J. S.; Martins-Costa, M. T. C.; Anglada, J. M. Molecular Reactions at Aqueous Interfaces. *Nat. Rev. Chem.* **2020**, *4* (9), 459–475. https://doi.org/10.1038/s41570-020-0203-2.

(2)   Law, Z. X.; Tsai, D.-H. Design of Aerosol Nanoparticles for Interfacial Catalysis. *Langmuir* **2022**, *38* (30), 9037–9042. https://doi.org/10.1021/acs.langmuir.2c01155.

(3)   Limmer, D. T.; Götz, A. W.; Bertram, T. H.; Nathanson, G. M. Molecular Insights into Chemical Reactions at Aqueous Aerosol Interfaces. *Annu. Rev. Phys. Chem.* **2024**, *75* (1), 111–135. https://doi.org/10.1146/annurev-physchem-083122-121620.

(4)   Onsager, L.; Samaras, N. N. T. The Surface Tension of Debye-Hückel Electrolytes. *J. Chem. Phys.* **1934**, *2* (8), 528–536. https://doi.org/10.1063/1.1749522.

(5)   Wagner, C. The Surface Tension of Dilute Solutions of Electrolytes. *Phys Z* **1924**, *25*, 474–477.

(6)   Jungwirth, P.; Tobias, D. J. Surface Effects on Aqueous Ionic Solvation: A Molecular Dynamics Simulation Study of NaCl at the Air/Water Interface from Infinite Dilution to Saturation. *J. Phys. Chem. B* **2000**, *104* (32), 7702–7706. https://doi.org/10.1021/jp000941y.

(7)   Otten, D. E.; Shaffer, P. R.; Geissler, P. L.; Saykally, R. J. Elucidating the Mechanism of Selective Ion Adsorption to the Liquid Water Surface. *Proc. Natl. Acad. Sci.* **2012**, *109* (3), 701–705. https://doi.org/10.1073/pnas.1116169109.

(8)   Geissler, P. L. Water Interfaces, Solvation, and Spectroscopy. *Annu. Rev. Phys. Chem.* **2013**, *64* (1), 317–337. https://doi.org/10.1146/annurev-physchem-040412-110153.

(9)   Devlin, S. W.; Jamnuch, S.; Xu, Q.; Chen, A. A.; Qian, J.; Pascal, T. A.; Saykally, R. J. Agglomeration Drives the Reversed Fractionation of Aqueous Carbonate and Bicarbonate at the Air–Water Interface. *J. Am. Chem. Soc.* **2023**, *145* (41), 22384–22393. https://doi.org/10.1021/jacs.3c05093.

(10)   Shen, Y. R. Optical Second Harmonic Generation at Interfaces. *Annu. Rev. Phys. Chem.* **1989**, *40* (1), 327–350. https://doi.org/10.1146/annurev.pc.40.100189.001551.

(11)   Yamaguchi, S.; Tahara, T. Precise Electronic χ(2) Spectra of Molecules Adsorbed at an Interface Measured by Multiplex Sum Frequency Generation. *J. Phys. Chem. B* **2004**, *108* (50), 19079–19082. https://doi.org/10.1021/jp045306x.

(12)   Petersen, P. B.; Saykally, R. J. Probing the Interfacial Structure of Aqueous Electrolytes with Femtosecond Second Harmonic Generation Spectroscopy. *J. Phys. Chem. B* **2006**, *110* (29), 14060–14073. https://doi.org/10.1021/jp0601825.

(13)   Petersen, P. B.; Saykally, R. J. Confirmation of Enhanced Anion Concentration at the Liquid Water Surface. *Chem. Phys. Lett.* **2004**, *397* (1–3), 51–55. https://doi.org/10.1016/j.cplett.2004.08.049.

(14)   Petersen, P. B.; Saykally, R. J.; Mucha, M.; Jungwirth, P. Enhanced Concentration of Polarizable Anions at the Liquid Water Surface: SHG Spectroscopy and MD Simulations of Sodium Thiocyanide. *J. Phys. Chem. B* **2005**, *109* (21), 10915–10921. https://doi.org/10.1021/jp050864c.

(15)   Bhattacharyya, D.; Mizuno, H.; Rizzuto, A. M.; Zhang, Y.; Saykally, R. J.; Bradforth, S. E. New Insights into the Charge-Transfer-to-Solvent Spectrum of Aqueous Iodide: Surface

versus Bulk. *J. Phys. Chem. Lett.* **2020**, *11* (5), 1656–1661.
https://doi.org/10.1021/acs.jpclett.9b03857.

(16)   Mizuno, H.; Rizzuto, A. M.; Saykally, R. J. Charge-Transfer-to-Solvent Spectrum of Thiocyanate at the Air/Water Interface Measured by Broadband Deep Ultraviolet Electronic Sum Frequency Generation Spectroscopy. *J. Phys. Chem. Lett.* **2018**, *9* (16), 4753–4757.
https://doi.org/10.1021/acs.jpclett.8b01966.

(17)   Viswanath, P.; Motschmann, H. Oriented Thiocyanate Anions at the Air−Electrolyte Interface and Its Implications on Interfacial Water - A Vibrational Sum Frequency Spectroscopy Study. *J. Phys. Chem. C* **2007**, *111* (12), 4484–4486. https://doi.org/10.1021/jp0702649.

(18)   Devlin, S. W.; McCaffrey, D. L.; Saykally, R. J. Characterizing Anion Adsorption to Aqueous Interfaces: Toluene–Water versus Air–Water. *J. Phys. Chem. Lett.* **2022**, *13* (1), 222–228. https://doi.org/10.1021/acs.jpclett.1c03816.

(19)   Lam, R. K.; Smith, J. W.; Rizzuto, A. M.; Karslıoğlu, O.; Bluhm, H.; Saykally, R. J. Reversed Interfacial Fractionation of Carbonate and Bicarbonate Evidenced by X-Ray Photoemission Spectroscopy. *J. Chem. Phys.* **2017**, *146* (9), 094703.
https://doi.org/10.1063/1.4977046.

(20)   Petersen, P. B.; Saykally, R. J. ON THE NATURE OF IONS AT THE LIQUID WATER SURFACE. *Annu. Rev. Phys. Chem.* **2006**, *57* (1), 333–364.
https://doi.org/10.1146/annurev.physchem.57.032905.104609.

(21)   Perrine, K. A.; Parry, K. M.; Stern, A. C.; Van Spyk, M. H. C.; Makowski, M. J.; Freites, J. A.; Winter, B.; Tobias, D. J.; Hemminger, J. C. Specific Cation Effects at Aqueous Solution−vapor Interfaces: Surfactant-like Behavior of Li+ Revealed by Experiments and Simulations. *Proc. Natl. Acad. Sci.* **2017**, *114* (51), 13363–13368.
https://doi.org/10.1073/pnas.1707540114.

(22)   Ng, K. C.; Adel, T.; Lao, K. U.; Varmecky, M. G.; Liu, Z.; Arrad, M.; Allen, H. C. Iron(III) Chloro Complexation at the Air–Aqueous FeCl3 Interface via Second Harmonic Generation Spectroscopy. *J. Phys. Chem. C* **2022**. https://doi.org/10.1021/acs.jpcc.2c02489.

(23)   England, J. L.; Haran, G. Role of Solvation Effects in Protein Denaturation: From Thermodynamics to Single Molecules and Back. *Annu. Rev. Phys. Chem.* **2011**, *62* (1), 257–277.
https://doi.org/10.1146/annurev-physchem-032210-103531.

(24)   Vazdar, M.; Vymětal, J.; Heyda, J.; Vondrášek, J.; Jungwirth, P. Like-Charge Guanidinium Pairing from Molecular Dynamics and Ab Initio Calculations. *J. Phys. Chem. A* **2011**, *115* (41), 11193–11201. https://doi.org/10.1021/jp203519p.

(25)   Wernersson, E.; Heyda, J.; Lund, M.; Mason, P. E.; Jungwirth, P. Orientational Dependence of the Affinity of Guanidinium Ions to the Water Surface. *J. Phys. Chem. B* **2011**, *115* (43), 12521–12526. https://doi.org/10.1021/jp207499s.

(26)   Boudon, S.; Wipff, G.; Maigret, B. Monte Carlo Simulations on the Like-Charged Guanidinium-Guanidinium Ion Pair in Water. *J. Phys. Chem.* **1990**, *94* (15), 6056–6061.
https://doi.org/10.1021/j100378a078.

(27)   Houriez, C.; Meot-Ner (Mautner), M.; Masella, M. Solvation of the Guanidinium Ion in Pure Aqueous Environments: A Theoretical Study from an "Ab Initio"-Based Polarizable Force Field. *J. Phys. Chem. B* **2017**, *121* (50), 11219–11228. https://doi.org/10.1021/acs.jpcb.7b07874.

(28)   Ekholm, V.; Vazdar, M.; Mason, P. E.; Bialik, E.; Walz, M.-M.; Öhrwall, G.; Werner, J.; Rubensson, J.-E.; Jungwirth, P.; Björneholm, O. Anomalous Surface Behavior of Hydrated Guanidinium Ions Due to Ion Pairing. *J. Chem. Phys.* **2018**, *148* (14), 144508.
https://doi.org/10.1063/1.5024348.

(29)   Werner, J.; Wernersson, E.; Ekholm, V.; Ottosson, N.; Öhrwall, G.; Heyda, J.; Persson, I.; Söderström, J.; Jungwirth, P.; Björneholm, O. Surface Behavior of Hydrated Guanidinium and Ammonium Ions: A Comparative Study by Photoelectron Spectroscopy and Molecular Dynamics. *J. Phys. Chem. B* **2014**, *118* (25), 7119–7127. https://doi.org/10.1021/jp500867w.

(30)   Vazdar, M.; Heyda, J.; Mason, P. E.; Tesei, G.; Allolio, C.; Lund, M.; Jungwirth, P. Arginine "Magic": Guanidinium Like-Charge Ion Pairing from Aqueous Salts to Cell Penetrating Peptides. *Acc. Chem. Res.* **2018**, *51* (6), 1455–1464. https://doi.org/10.1021/acs.accounts.8b00098.

(31)   Blandamer, M. J.; Fox, M. F. Theory and Applications of Charge-Transfer-to-Solvent Spectra. *Chem. Rev.* **1970**, *70* (1), 59–93. https://doi.org/10.1021/cr60263a002.

(32)   Marin, T. W.; Janik, I.; Bartels, D. M. Ultraviolet Charge-Transfer-to-Solvent Spectroscopy of Halide and Hydroxide Ions in Subcritical and Supercritical Water. *Phys. Chem. Chem. Phys.* **2019**, *21* (44), 24419–24428. https://doi.org/10.1039/C9CP03805A.

(33)   Antol, I.; Glasovac, Z.; Crespo-Otero, R.; Barbatti, M. Guanidine and Guanidinium Cation in the Excited State—Theoretical Investigation. *J. Chem. Phys.* **2014**, *141* (7), 074307. https://doi.org/10.1063/1.4892569.

(34)   Petersen, P. B.; Johnson, J. C.; Knutsen, K. P.; Saykally, R. J. Direct Experimental Validation of the Jones–Ray Effect. *Chem. Phys. Lett.* **2004**, *397* (1), 46–50. https://doi.org/10.1016/j.cplett.2004.08.048.

(35)   Devlin, S. W.; Benjamin, I.; Saykally, R. J. On the Mechanisms of Ion Adsorption to Aqueous Interfaces: Air-Water vs. Oil-Water. *Proc. Natl. Acad. Sci.* **2022**, *119* (42), e2210857119. https://doi.org/10.1073/pnas.2210857119.

(36)   Eckenrode, H. M.; Jen, S.-H.; Han, J.; Yeh, A.-G.; Dai, H.-L. Adsorption of a Cationic Dye Molecule on Polystyrene Microspheres in Colloids: Effect of Surface Charge and Composition Probed by Second Harmonic Generation. *J. Phys. Chem. B* **2005**, *109* (10), 4646–4653. https://doi.org/10.1021/jp045610q.

(37)   Castro, A.; Bhattacharyya, K.; Eisenthal, K. B. Energetics of Adsorption of Neutral and Charged Molecules at the Air/Water Interface by Second Harmonic Generation: Hydrophobic and Solvation Effects. *J. Chem. Phys.* **1991**, *95* (2), 1310–1315. https://doi.org/10.1063/1.461113.

(38)   Heinz, T. F. Chapter 5 - Second-Order Nonlinear Optical Effects at Surfaces and Interfaces. In *Modern Problems in Condensed Matter Sciences*; Ponath, H.-E., Stegeman, G. I., Eds.; Nonlinear Surface Electromagnetic Phenomena; Elsevier, 1991; Vol. 29, pp 353–416. https://doi.org/10.1016/B978-0-444-88359-9.50011-9.

(39)   Hao, H.; Xie, Q.; Ai, J.; Wang, Y.; Bian, H. Specific Counter-Cation Effect on the Molecular Orientation of Thiocyanate Anions at the Aqueous Solution Interface. *Phys. Chem. Chem. Phys.* **2020**, *22* (18), 10106–10115. https://doi.org/10.1039/D0CP00974A.

(40)   Heiles, S.; Cooper, R. J.; DiTucci, M. J.; Williams, E. R. Hydration of Guanidinium Depends on Its Local Environment. *Chem. Sci.* **2015**, *6* (6), 3420–3429. https://doi.org/10.1039/C5SC00618J.

(41)   Bian, H.; Feng, R.; Xu, Y.; Guo, Y.; Wang, H. Increased Interfacial Thickness of the NaF, NaCl and NaBr Salt Aqueous Solutions Probed with Non-Resonant Surface Second Harmonic Generation (SHG). *Phys. Chem. Chem. Phys.* **2008**, *10* (32), 4920–4931. https://doi.org/10.1039/B806362A.

(42)   Rehl, B.; Rashwan, M.; DeWalt-Kerian, E. L.; Jarisz, T. A.; Darlington, A. M.; Hore, D. K.; Gibbs, J. M. New Insights into χ(3) Measurements: Comparing Nonresonant Second

Harmonic Generation and Resonant Sum Frequency Generation at the Silica/Aqueous Electrolyte Interface. *J. Phys. Chem. C* **2019**, *123* (17), 10991–11000. https://doi.org/10.1021/acs.jpcc.9b01300.

(43)   Jungwirth, P.; Tobias, D. J. Ions at the Air/Water Interface. *J. Phys. Chem. B* **2002**, *106* (25), 6361–6373. https://doi.org/10.1021/jp020242g.

(44)   Seki, T.; Yu, C.-C.; Chiang, K.-Y.; Greco, A.; Yu, X.; Matsumura, F.; Bonn, M.; Nagata, Y. Ions Speciation at the Water–Air Interface. *J. Am. Chem. Soc.* **2023**, *145* (19), 10622–10630. https://doi.org/10.1021/jacs.3c00517.

(45)   Okur, H. I.; Hladílková, J.; Rembert, K. B.; Cho, Y.; Heyda, J.; Dzubiella, J.; Cremer, P. S.; Jungwirth, P. Beyond the Hofmeister Series: Ion-Specific Effects on Proteins and Their Biological Functions. *J. Phys. Chem. B* **2017**, *121* (9), 1997–2014. https://doi.org/10.1021/acs.jpcb.6b10797.

(46)   Litman, Y.; Chiang, K.-Y.; Seki, T.; Nagata, Y.; Bonn, M. Surface Stratification Determines the Interfacial Water Structure of Simple Electrolyte Solutions. *Nat. Chem.* **2024**, 1–7. https://doi.org/10.1038/s41557-023-01416-6.

(47)   Neal, J. F.; Saha, A.; Zerkle, M. M.; Zhao, W.; Rogers, M. M.; Flood, A. H.; Allen, H. C. Molecular Recognition and Hydration Energy Mismatch Combine To Inform Ion Binding Selectivity at Aqueous Interfaces. *J. Phys. Chem. A* **2020**, *124* (49), 10171–10180. https://doi.org/10.1021/acs.jpca.0c09568.

(48)   Benjamin, I. Structure, Thermodynamics, and Dynamics of Thiocyanate Ion Adsorption and Transfer across the Water/Toluene Interface. *J. Phys. Chem. B* **2022**, *126* (30), 5706–5714. https://doi.org/10.1021/acs.jpcb.2c03956.

(49)   Balos, V.; Bonn, M.; Hunger, J. Anionic and Cationic Hofmeister Effects Are Non-Additive for Guanidinium Salts. *Phys. Chem. Chem. Phys.* **2017**, *19* (15), 9724–9728. https://doi.org/10.1039/C7CP00790F.

(50)   Thompson, A. P.; Aktulga, H. M.; Berger, R.; Bolintineanu, D. S.; Brown, W. M.; Crozier, P. S.; in 't Veld, P. J.; Kohlmeyer, A.; Moore, S. G.; Nguyen, T. D.; et al. LAMMPS - a Flexible Simulation Tool for Particle-Based Materials Modeling at the Atomic, Meso, and Continuum Scales. *Comput. Phys. Commun.* **2022**, *271*, 108171. https://doi.org/10.1016/j.cpc.2021.108171.

(51)   Abascal, J. L. F.; Vega, C. A General Purpose Model for the Condensed Phases of Water: TIP4P/2005. *J. Chem. Phys.* **2005**, *123* (23), 234505. https://doi.org/10.1063/1.2121687.

(52)   Lamoureux, G.; Roux, B. Modeling Induced Polarization with Classical Drude Oscillators: Theory and Molecular Dynamics Simulation Algorithm. *J. Chem. Phys.* **2003**, *119* (6), 3025–3039. https://doi.org/10.1063/1.1589749.

(53)   Lamoureux, G.; Harder, E.; Vorobyov, I. V.; Roux, B.; MacKerell, A. D. A Polarizable Model of Water for Molecular Dynamics Simulations of Biomolecules. *Chem. Phys. Lett.* **2006**, *418* (1–3), 245–249. https://doi.org/10.1016/j.cplett.2005.10.135.

(54)   Lemkul, J. A.; Huang, J.; Roux, B.; MacKerell, A. D. Jr. An Empirical Polarizable Force Field Based on the Classical Drude Oscillator Model: Development History and Recent Applications. *Chem. Rev.* **2016**, *116* (9), 4983–5013. https://doi.org/10.1021/acs.chemrev.5b00505.

(55)   Dodin, A.; Geissler, P. L. Symmetrized Drude Oscillator Force Fields Improve Numerical Performance of Polarizable Molecular Dynamics. *J. Chem. Theory Comput.* **2023**, *19* (10), 2906–2917. https://doi.org/10.1021/acs.jctc.3c00278.

(56)   Kamberaj, H.; Low, R. J.; Neal, M. P. Time Reversible and Symplectic Integrators for Molecular Dynamics Simulations of Rigid Molecules. *J. Chem. Phys.* **2005**, *122* (22), 224114. https://doi.org/10.1063/1.1906216.

(57)   Kästner, J. Umbrella Sampling. *WIREs Comput. Mol. Sci.* **2011**, *1* (6), 932–942. https://doi.org/10.1002/wcms.66.

(58)   Grossfield, A. WHAM: The Weighted Histogram Analysis Method, 2002. http://membrane.urmc.rochester.edu/wordpress/?page_id=126.

(59)   Kumar, S.; Rosenberg, J. M.; Bouzida, D.; Swendsen, R. H.; Kollman, P. A. Multidimensional Free-Energy Calculations Using the Weighted Histogram Analysis Method. *J. Comput. Chem.* **1995**, *16* (11), 1339–1350. https://doi.org/10.1002/jcc.540161104.

(60)   Kumar, S.; Rosenberg, J. M.; Bouzida, D.; Swendsen, R. H.; Kollman, P. A. The Weighted Histogram Analysis Method for Free-Energy Calculations on Biomolecules. I. The Method. *J. Comput. Chem.* **1992**, *13* (8), 1011–1021. https://doi.org/10.1002/jcc.540130812.

(61)   Souaille, M.; Roux, B. Extension to the Weighted Histogram Analysis Method: Combining Umbrella Sampling with Free Energy Calculations. *Comput. Phys. Commun.* **2001**, *135* (1), 40–57. https://doi.org/10.1016/S0010-4655(00)00215-0.

(62)   Breslow, R.; Guo, T. Surface Tension Measurements Show That Chaotropic Salting-in Denaturants Are Not Just Water-Structure Breakers. *Proc. Natl. Acad. Sci.* **1990**, *87* (1), 167–169. https://doi.org/10.1073/pnas.87.1.167.

(63)   Shih, O.; England, A. H.; Dallinger, G. C.; Smith, J. W.; Duffey, K. C.; Cohen, R. C.; Prendergast, D.; Saykally, R. J. Cation-Cation Contact Pairing in Water: Guanidinium. *J. Chem. Phys.* **2013**, *139* (3), 035104. https://doi.org/10.1063/1.4813281.

Chapter 4 – Strong Adsorption of Divalent Thiosulfate Anions to the Air-Water Interface

4.1. Introduction

Sulfur oxyanions have gained increased attention as they have been identified as contaminants of emerging concern (CECs) due to their indirect aquatic toxicity.[1,2] Human mining activity and incomplete wastewater treatments have led to increased concentrations of these ions into oceans and streams, where they acidify natural waters.[3] Additionally, these pollutants may escape into the atmosphere via aqueous aerosols and contribute to negative environmental phenomena, such as acid rain, downstream sulfate generation, and climate forcing.[4,5] Much work has been done to characterize the adsorption of sulfur oxyanions into atmospheric aerosols and their reactivity with relevant environmental gasses, such as ozone.[6,7] Although the number of sulfur oxyanions and their potential reaction routes are vast, here we focus on a small subset of sulfur species involved in the oxidation reaction of thiosulfate by ozone in efforts to quantify their surface activity and reaction kinetics. The air-water interface is a ubiquitous environment that is present from global to microscopic scales. Developing a molecular picture of ions at these interfaces can improve reactivity models and advance our fundamental understanding.

Our experimental approach is twofold and consists of spectroscopic measurements to quantify the surface adsorption of sulfur oxyanions coupled with mass spectrometry of microdroplets to track reaction kinetics. Deep-UV second harmonic generation (DUV-SHG) spectroscopy has developed into a powerful molecular probe of interfacial ions that we leverage here to extract a Gibbs free energy of adsorption. Given the surface specificity of DUV-SHG, we can directly confirm the interfacial presence of ions at the air-water interface within the experimental probe depth of ca. 1 nm (1-3 molecular layers).[8] Additionally, with microdroplet mass spectrometry, we trap solution microdroplets in a reaction-controlled environment before analyzing their composition using a mass spectrometer. By bridging surface-specific and bulk characterization techniques, we can infer a microscopic picture of a simple microdroplet partitioned into surface and bulk regions; we can then vary conditions in the microdroplet trap to induce reactions within the droplets and track the detected species as a function of time to better understand reaction kinetics. We analyze microdroplets of thiosulfate solution as they react with ozone and use DUV-SHG experiments to determine relative surface propensities of sulfur oxyanions. We find a surprisingly strong surface propensity for the thiosulfate ion, develop a new reaction mechanism for thiosulfate ozonolysis, and advance our general fundamental understanding of ions at interfaces.

4.2. Methods

4.2.1. DUV-SHG

We directly probe sulfur oxyanions at the air-water interface using resonantly enhanced DUV-SHG spectroscopy. As a second-order nonlinear spectroscopy, DUV-SHG is a powerful surface specific molecular probe that, under the electric dipole approximation, generates signal from only the topmost molecular layers of the air-water interface. The full experimental details have been covered in Chapter 2 and elsewhere; here only essential details are provided[8,9]. The 800 nm output of a Ti:Sapphire amplifier (Spectra Physics, Spitfire) is directed to an optical parametric amplifier (TOPAS Prime) where the fundamental input wavelength is generated (386 – 440 nm). Solutions of $Na_2S_2O_3$ (Sigma Aldrich, Reddi-Dri 99%), Na_2SO_3 (Fisher, ≥98%), and Na_2SO_4 (Sigma Aldrich, Reddi-Dri 99%) were made using ultrapure 18.2 MΩ water (Millipore, Milli-Q). The fundamental beam was directed at solutions held in Petri dishes at an angle 60° relative to the solution surface normal. DUV-SHG signal reflected from the solution interface is spectrally filtered from the colinear fundamental and detected by a photomultiplier tube (Hamamatsu, R7154PHA). Figure 4.1 A,C depicts the experimental configuration and SHG process, respectively.

In DUV-SHG, two photons are simultaneously annihilated and generate a third upconverted photon at twice the input frequency.[10] The input wavelength is chosen such that the second harmonic is resonant with the charge-transfer-to-solvent (CTTS) transition of the anions for greater signal enhancement. Much work has been done to characterize the energy and magnitude of CTTS transitions of common ions, including the sulfur oxyanions studied here[11]. Despite the broad absorption typical of these transitions, the center absorption wavelengths are well-separated for each of the three species studied here and therefore require different input wavelengths. UV spectra highlighting the CTTS transitions are plotted in Figure 4.1B for the sulfur oxyanions studied. Since DUV-SHG is a parametric process, no energy is transferred to the chromophores, minimizing the risk of generating photoproducts at the SHG wavelength.
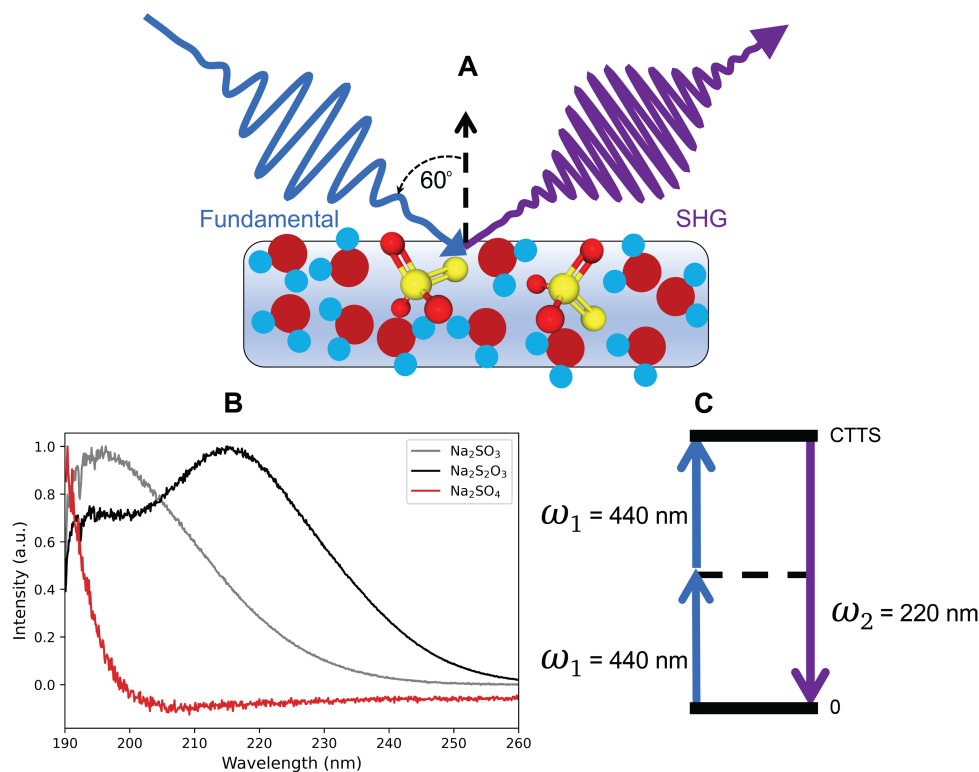
Figure 4.1. DUV-SHG experimental configuration used for probing thiosulfate at the air-water interface. **A)** Molecular depiction of SHG produced at the air-water interface, containing contributions from both water molecules and resonant thiosulfate anions. **B)** UV-Visible spectra of sulfur oxyanions. The CTTS transition peaks of sulfite and thiosulfate are clearly visible, along with the low energy tail of the sulfate transition. **C)** Energy-level diagram highlighting the nonlinear SHG parametric process. The fundamental at 440 nm is two-photon resonant with the CTTS transition of thiosulfate.

4.2.2. Mass Spectrometry

Microdroplets are generated by a piezoelectric dispenser (Microfab, MJ-ABP-01) with a 30 μm orifice and charged with a +450 V DC bias by an induction electrode. Individual levitated microdroplets were trapped using a quadrupole electrodynamic trap (QET) and ejected into an open-port sampling interface (OPSI) for analysis in a mass spectrometer (MS).[12,13] A schematic of the mass spectrometry experiments is shown in Figure 4.2. The QET is housed within a constant temperature (295 K) control chamber and droplets are subjected to a constant flow (550 cm^3 min^{-1}) of humidified N_2, O_2, and O_3. The droplets were generated from a 0.25 M solution of sodium thiosulfate at pH 5, 9, or 13. Solutions at pH 5 and 9 were buffered using malonic acid-NaOH and glycine-HCl, respectively. Solutions at pH 13 were adjusted using only NaOH due to a lack of compatible buffers in this region. Single droplets were ejected sequentially and their contents at each time point were analyzed using OPSI-MS, providing concentrations of reactants, intermediates, and products over time.
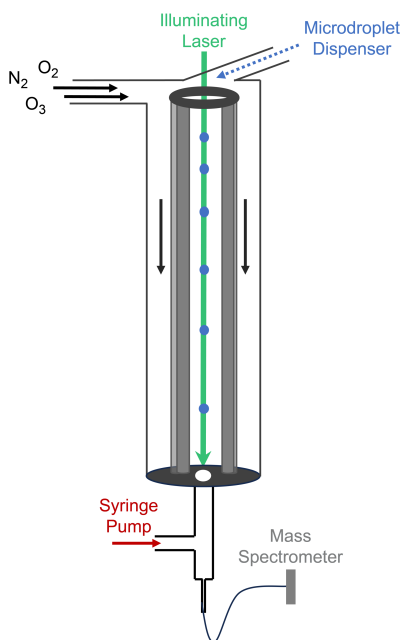
Figure 4.2 Experimental diagram of the QET chamber leading to the OPSI-MS. Microdroplets are generated and introduced into the QET along with reactive gasses. After a fixed amount of time in the control chamber, microdroplets are dispensed into the OPSI-MS for analysis.

4.2.3. Kinetic Modeling

To simulate kinetic mechanisms, we use the software Kinetiscope©, which employs a Monte Carlo-based approach.[14] In these simulations, concentrations are propagated in time using probabilities for each reaction step. We enter a proposed mechanism into Kinetiscope© as a series of discrete reaction and diffusion steps with associated constants constrained by literature values. Geometric corrections accounting for surface-to-volume ratios of microdroplets and partitioning of solutes between the bulk and interface are implemented in the simulations.[15] All simulated species in the reaction mechanism are allowed to adsorb to the interface from the liquid bulk and interfacial gas regions. Species are then able to react and desorb into the liquid bulk or gas regions. There is limited information regarding the surface propensity of sulfur oxyanions; therefore, DUV-SHG results are used to determine the relative surface partitioning of thiosulfate, sulfate, and sulfite anions.

4.3. Results and Discussion

The concentrations of interfacial molecules are influenced by the molecule's surface activity, measured as the free energy of adsorption to the interface (ΔG_{ads}) or the equilibrium constant for surface adsorption (K_{eq}^{ads}). Few studies have measured either ΔG_{ads} or K_{eq}^{ads} for the sulfur oxyanions involved in the ozonation of thiosulfate. Here, we use DUV-SHG to study sodium thiosulfate ($Na_2S_2O_3$), sodium sulfate (Na_2SO_4), and sodium sulfite (Na_2SO_3) solutions. Figure 4.3 plots the normalized SHG response of each solution against bulk concentration.
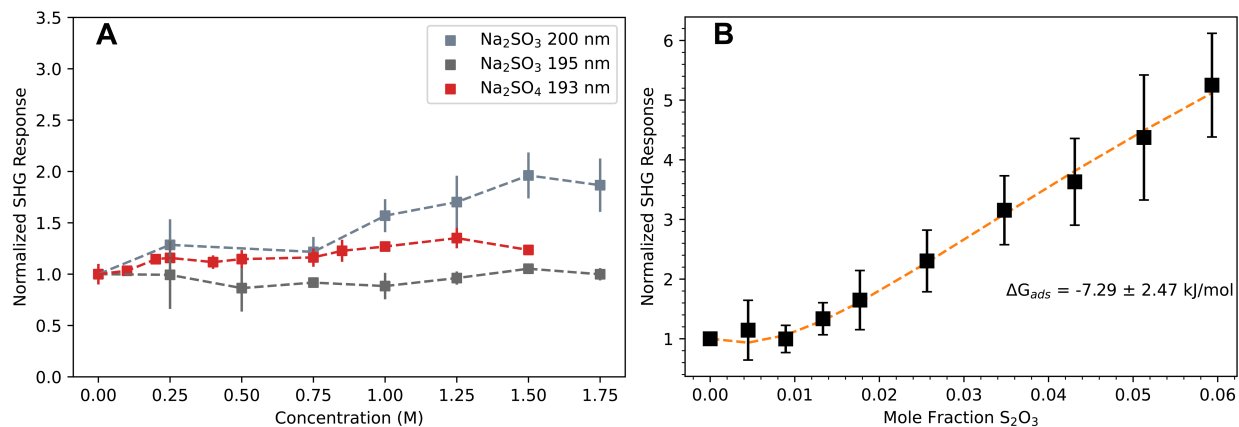
Figure 4.3. Normalized DUV-SHG response of sulfur oxyanions at the air-water interface. **A)** Response of sodium sulfite and sodium sulfate solutions exhibiting a weak concentration-dependent signal response. Dashed lines act as a visual guide. **B)** Response of sodium thiosulfate exhibiting a clear concentration dependent DUV-SHG signal. Orange dashed line represents the fit to a Langmuir model. Error bars represent one standard deviation.

As expected, sulfate solutions exhibit a flat SHG response across the measured concentration range. As part of the Hoffmeister series, sulfate is a known kosmotrope and several studies have found that it is well-solvated in water, with no significant interfacial presence.[16–19] Previous Raman thermometry measurements on 3 M aqueous $(NH_4)_2SO_4$ microdroplets observed no change in the evaporation rate relative to pure water, which suggests that neither ammonium nor sulfate significantly impact the exchange of water molecules across the air-water interface.[16] Additionally, recent phase-sensitive vibrational-SHG measurements observed minimal perturbation of the free O-H stretch band of interfacial water molecules in $MgSO_4$ and Na_2SO_4 solutions.[17] It should be noted that our measurements of sulfate solutions were made with the second harmonic ca. 20 nm away from the expected CTTS transition maximum due to limitations in our optics and to avoid resonant water molecule transitions; therefore, we expect a weak signal enhancement. Still, SHG is sensitive enough to capture signal changes under non-resonant conditions and our results agree with previous studies.[20]

Sodium sulfite measurements collected at 200 nm display a weak signal increase above 1 M. Previous SHG work has attributed this weak linear response to an interfacial thickening of the water layer due to an increased solute concentration, which alters the hyperpolarizability of interfacial water moleucles.[9,20,21] Given the broad linewidth of CTTS transitions, we additionally probed sodium sulfite at 390 nm (195 nm SHG), and observe a clear uniform response similar to sulfate measurements. If sulfite ions were indeed surface active, a 5 nm shift away from the resonant transition center would not completely diminish the SHG response. That the response from sulfite ions is similar to sulfate ions indicates a lack of surface enhancement.

Unlike sodium sulfate and sodium sulfite solutions, Figure 4.3B depicts a strong concentration-dependent SHG signal for solutions of sodium thiosulfate. Fitting the normalized SHG response to a Langmuir isotherm, we extract a ΔG_{ads} of -7.28 kJ/mol for thiosulfate anions

at the air-water interface. These results indicate that thiosulfate, also a doubly charged anion, exhibits a propensity for the interface not seen in similarly charged sulfur oxyanions. This behavior is striking, since early theories of ions at interfaces by Onsager and Samaras predict a strong surface repulsion of doubly charged ions based on electrostatic arguments.[22] As early experimental and theoretical studies began to support theories of interfacial ions, it was thought that only large, highly polarizable anions could be surface enhanced and excluded multicharged anions and cations.[23] However, much recent progress has been made in our understanding of interfacial ions and we now have compelling evidence that supports a broader set of surface-active ions.

Recent X-ray photoelectron spectroscopy and DUV-SHG studies found that the carbonate ion similarly preferentially adsorbs to the air-water interface more strongly than the singly charged bicarbonate ion.[21,24] MD simulations found carbonate ions form near-neutral clusters with surrounding water molecules and sodium counterions, which is better accommodated at the interface than in the bulk. Similarly, studies indicate that like-charge ion pairing is also involved in the surface adsorption of guanidinium cations.[9,25] While we do not yet have a detailed mechanism to explain the surface adsorption of thiosulfate, it is not unreasonable to propose that favorable ion-pairing effects are likely involved. Without MD simulations we lack a theoretical route to validate the measured ΔG_{ads} of thiosulfate and instead turn to kinetic studies to help confirm these results.
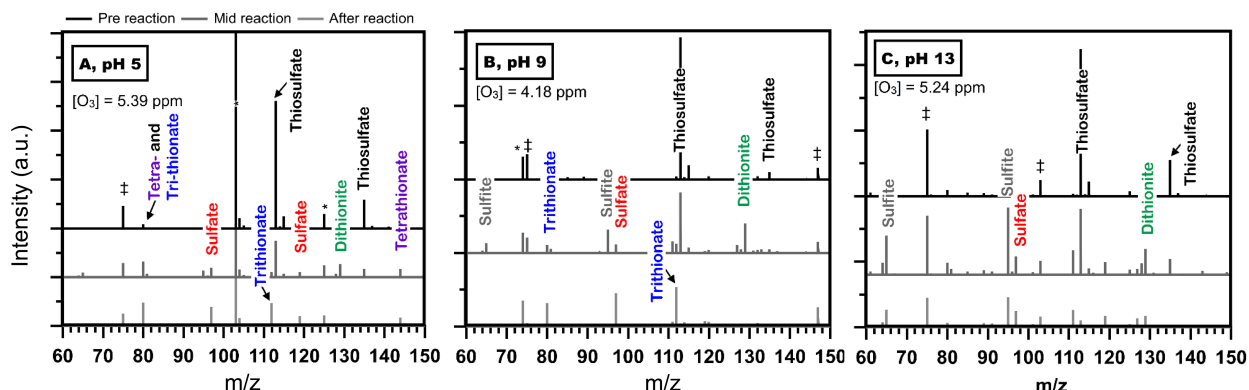
Figure 4.4. Representative mass spectra from the ozone oxidation of a 0.25 M thiosulfate microdroplets at (A) pH 5, (B) pH 9, and (C) pH 13. In each panel a mass spectrum is shown that is before reaction (t = 0 min), during reaction (t = 5 min), and after reaction (t = 20 min). Spectra are offset along the y-axis for clarity.

Using OPSI-MS, we record the concentrations of species in sodium thiosulfate microdroplets as a function ozone reaction time in the control chamber at three different solution pH values. Figure 4.4 highlights the representative OPSI-MS data within a 20 min interval for thiosulfate microdroplets at three pH values and timestamps. We find that as microdroplet pH increases, the reactions generate a stronger sulfite signal (m/z = 65 and 95) and less thiosulfate (m/z = 113 and 135) is consumed. For a detailed measure of the reaction kinetics, droplets are further analyzed every 1-2 minutes and repeated over five trials for increased signal-to-noise. OPSI-MS intensities are converted to concentrations using reference calibration curves[26]. All

species in Figure 4.5 are plotted as a function of reaction time along with the inclusion of an "S Loss" term, which is an umbrella term for unaccounted for sulfur products that may have been lost to gas-phase evaporation, elemental sulfur formation, or experimental uncertainty. The top panels of Figure 4.5 track the concentration of thiosulfate (dark gray points) and highlight the fact that thiosulfate is indeed consumed slower at high pH.
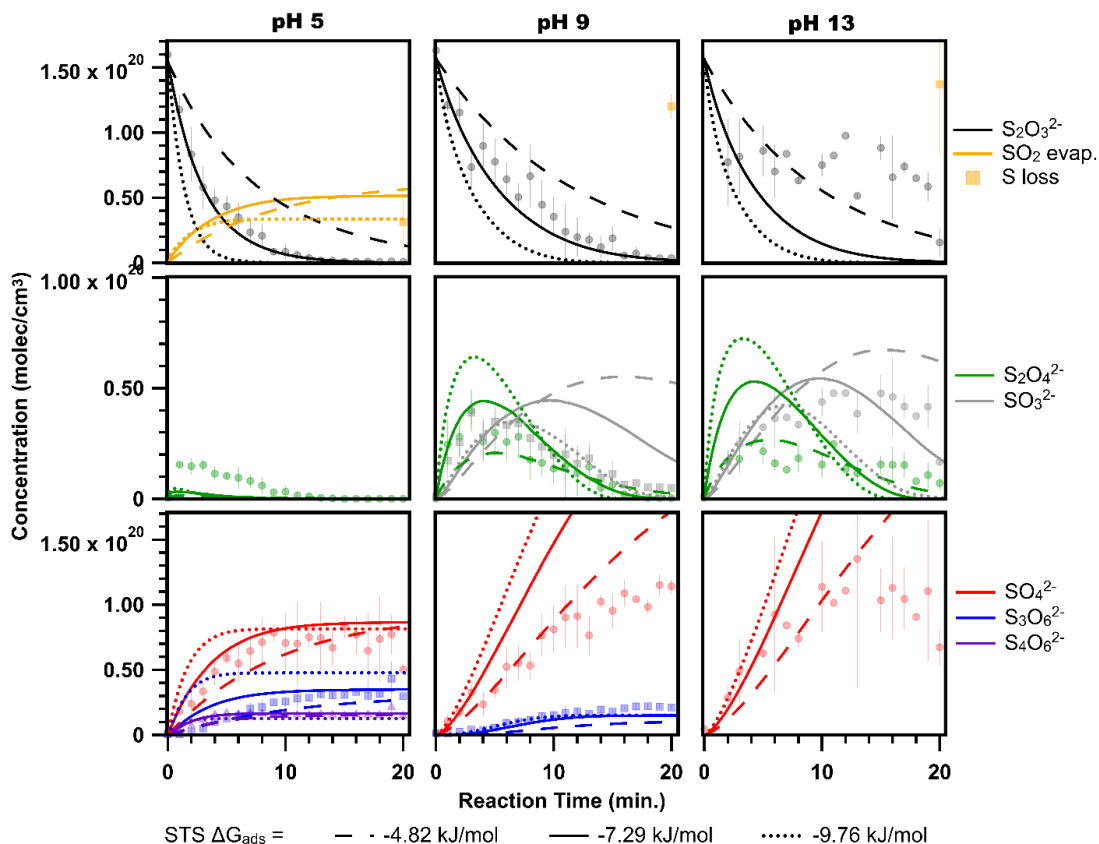
Figure 4.5. Reaction kinetics for the ozone oxidation of sodium thiosulfate in pH 5 (left), pH 9 (middle), and pH 13 (right) solutions compared with simulation results, using three values for thiosulfate anion surface activity. Experimental data are plotted as points with error bars representing one standard deviation. Simulation results are generated assuming the average value for the adsorption free energy (ΔG = -7.29 kJ/mol; solid lines), minimum favorable adsorption free energy (ΔG = -4.82 kJ/mol; dashed lines), and maximum favorable adsorption free energy (ΔG = -9.76 kJ/mol; dotted lines).

In the middle panels of Figure 4.5, the green points represent the sum of dithionite ($S_2O_4^{2-}$) and hydrogen dithionite ($HS_2O_4^-$) and grey points represent the sum of sulfite and bisulfite (HSO_3^-), as we cannot distinguish protonated from deprotonated species in the mass spectra. We can, however, make some assumptions about the speciation using the known pKa values for each species. Given that the pKa for dithionite is 2.44, we do not expect a significant amount of the protonated form to be present at the pH values studied here.[27] The pKa for sulfite is 7.2, so there may be a significant concentration of bisulfite in the pH 5 experiments, although we are unable to detect bisulfite directly.[28] Regardless of exact speciation, a significant amount of dithionite is

detected across the pH values, and a significant amount of sulfite is detected at pH 9 and pH 13. Although sulfite is known to react rapidly with ozone to form sulfate, here it would need to compete with thiosulfate for available ozone, resulting in more sulfite being present. Dithionite is known to decompose in water with relatively slow reaction rates and would explain why it is present across all pH measurements.[7]

The bottom panels in Figure 4.5 show that sulfate (red) is detected at all pH values, but tetrathionate ($S_4O_6^{2-}$, purple) is only detected at pH 5, and neither trithionate ($S_3O_6^{2-}$, blue) nor tetrathionate is detected at pH 13. This suggests that the formation of both trithionate and tetrathionate is pH-dependent, which is not readily explained by the current reaction mechanisms. Additionally, the currently accepted reaction mechanism invokes a disproportionation reaction between tetrathionate and sulfite to produce trithionate.[29] This could explain the presence of trithionate at pH 5, but appears inconsistent with the pH 9 data, which show trithionate without tetrathionate. It is possible that any tetrathionate produced immediately reacted to form trithionate, resulting in tetrathionate concentrations below our detection limit. Therefore, we conclude that the currently accepted mechanism does not adequately explain the relative production of trithionate and tetrathionate across the pH range studied here.

Given the experimental results of Figure 4.5, we propose a new mechanism for thiosulfate ozonation in Scheme 4.1. This mechanism includes dithionite as a reaction intermediate, is pH dependent, includes a production pathway for trithionate that is independent of tetrathionate, and changes the tetrathionate production pathway away from a single step to a multistep mechanism. This proposed mechanism is largely based on known species and reactions, incorporates much of the currently accepted chemistry, and can better explain the pH-dependent changes in the ozone oxidation of thiosulfate. By inputting Scheme 1 into Kinetiscope©, we simulate the reaction kinetics, which are plotted in Figure 4.5 as lines for direct comparison to the experimental results.

Scheme 4.1. Updated mechanism proposed for the ozone oxidation of thiosulfate.
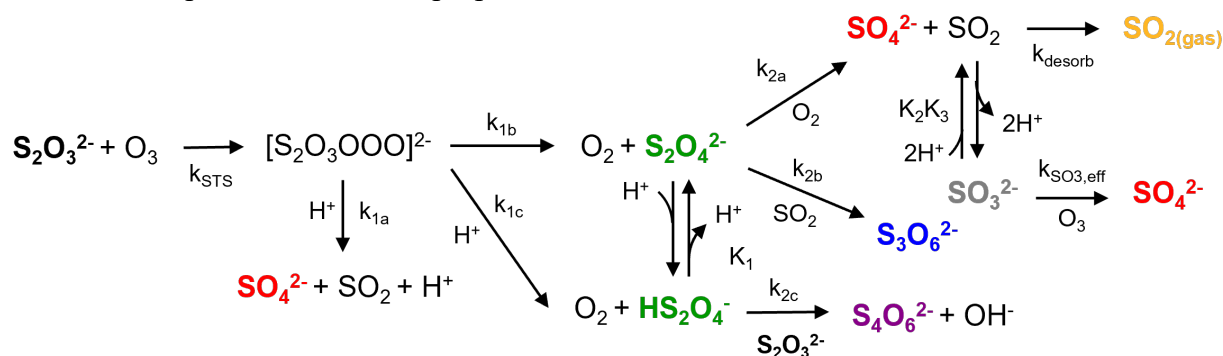
Given the uncertainty in the extracted ΔG_{ads} for thiosulfate anions, we generate kinetic models utilizing the average, maximum, and minimum free energy values extracted from DUV-SHG results. The surface activities of all other solutes are set relative to thiosulfate, with sulfate and sulfite being less surface active, as indicated by DUV-SHG. Hydrogen dithionate, trithionate, and tetrathionate are equally surface active while dithionite is more surface active. In Figure 4.5,

simulation results (lines) are compared to the experimental data. We see that the average value for the adsorption free energy (ΔG = -7.29 kJ/mol) most closely recreates the experimental data at pH 5 and pH 9. Specifically, the simulated thiosulfate (black) decay, trithionate production (blue), and tetrathionate production (purple) show excellent agreement with experimental data. The simulated sulfate production (red) also shows excellent agreement with experimental data at pH 5, but overestimates the amount of observed sulfate production at pH 9. This discrepancy at pH 9 is likely due to the high sulfur loss, which the kinetic model does not reliably account for. Comparing the simulated and experimental results for dithionite and sulfite is complicated due to uncertainties in the concentrations for each of these species. Dithionite is not stable in aqueous solution, as it decomposes into sulfite and sulfate, and therefore calibration curves were not obtained for dithionite and the concentrations shown here are qualitative rather than quantitative. Furthermore, because dithionite decomposes into sulfite, the sulfite signal at pH 9 may be skewed. Despite these issues, we find that the kinetic simulations accurately recreate the kinetic behavior of dithionite at pH 5 and pH 9.

Interestingly, simulations using the minimum favorable adsorption free energy of thiosulfate (ΔG_{ads} = -4.82 kJ/mol) more closely match the experimental data at pH 13. This seems to suggest that thiosulfate is less surface active in this highly alkaline environment. Therefore, we perform additional DUV-SHG measurements of thiosulfate solutions adjusted to pH 13 to determine potential changes in the interfacial response. A suppression of thiosulfate ions at the interface would manifest as decreased SHG intensity and may exhibit a non-Langmuir response. Figure 4.6A displays the normalized SHG response of thiosulfate at pH 13, and the extracted ΔG_{ads} of thiosulfate appears to shift in agreement with the kinetic model. However, the uncertainty in these measurements remains large and the intensity of the SHG response is not significantly different than the pH 6 measurements. Why then does the highly alkaline environment data predict a less favorable free energy?
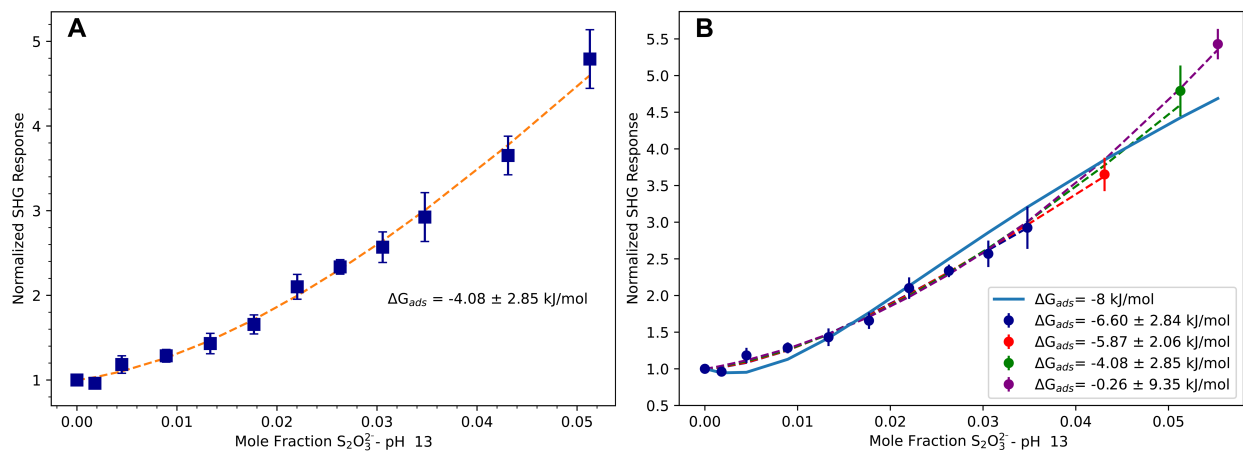
Figure 4.6. Normalized DUV-SHG response of sodium thiosulfate solutions at pH 13. **A)** DUV-SHG response of thiosulfate fit to a Langmuir model exhibiting a less favorable ΔG_{ads}. **B)** The extracted ΔG_{ads} recorded as high concentration points are included in the fit. For reference, a fixed ΔG_{ads} Langmuir fit is provided (solid blue line).

Analyzing the data in Figure 4.6A closer, we find that the high concentration points significantly affect the value of the extracted free energy. This observation is highlighted in Figure 4.6B, where we track the ΔG_{ads} as more points are included in the fit. There is an overall decrease in the magnitude of the free energy that becomes more pronounced with included concentrations over 2 M. Previous SHG studies observed increased SHG signal at high concentrations that was not well-fit using a Langmuir model.[30] This response was attributed to ion pairing effects that become more prominent with increased solute concentration. Additionally, studies indicate that hydroxide ions are repelled from the air-water interface and accumulate in a subsurface layer.[31] It is unclear how this accumulated hydroxide layer may interact with cosolvated ions such as thiosulfate. Seki et al. saw an increased surface activity (< 50%) in hydrophobic ions with the addition of cosolvated hydrophilic ions.[19] Their work finds that the addition of hydrophilic ions affects ion speciation across the interfacial landscape. This reasoning does not explain the high pH results found here, since we would then expect a greater response from thiosulfate if hydrophilic hydroxide ions were substantially promoting more thiosulfate to the interface. Thus, while our data suggest that the ΔG_{ads} of thiosulfate at the air-water interface is lower at increased solution pH, we do not have the complete molecular details required to explain this effect. The SHG response appears to shift away from a Langmuir shape and may be indicative of ion-pairing contributions. A modified adsorption isotherm may provide a better fit to the data here; however, we retain a simple Langmuir model, as we have found that the free energy extracted is typically not substantially different from that with other models.[8,9]

It is unclear if the observed decrease in thiosulfate surface propensity is a result of cosolvated ion interactions. Given that we suspect ion pairing effects are involved in promoting thiosulfate ions to the interface, we do not yet know the nature of these effects and whether they may be disrupted by hydroxide ions. Future work aimed at studying the SHG response of known surface enhanced ions, such as thiocyanate, as a function of pH may provide further clarification. Previous work detailing the mechanism of ion adsorption found that surface active ions displace interfacial water molecules into the bulk where they are fully coordinated which acts as the driving force for ions partitioning to the interface. Therefore, additional temperature dependent SHG measurements at these different pH environments may help uncover changes in the enthalpic and entropic contributions. Theoretical MD simulations would undoubtably be necessary to extract meaningful mechanistic details.

4.4. Conclusions

In summary, we complement interfacial studies of sulfur oxyanions with microdroplet kinetic measurements to better understand the mechanism of thiosulfate oxidation by ozone. Using DUV-SHG, we find that thiosulfate anions favorably adsorb to the air-water interface and extract a Gibbs free energy of adsorption. That this doubly charged anion demonstrates a greater surface propensity than similarly charged sulfur oxyanions is surprising. Given recent studies of interfacial ions, ion-paring effects may be involved, but without accompanying theoretical calculations we are not able to provide further molecular details. OPSI-MS was used to study microdroplets of

thiosulfate solution exposed to ozone in a control chamber and extract kinetic data. We find that the thiosulfate ozonolysis reaction is pH dependent, a feature not explained by current kinetic models. By combining our DUV-SHG and OPSI-MS measurements, we develop an updated reaction mechanism for thiosulfate oxidation and use Kinetiscope to simulate the kinetics. Our proposed reaction mechanism is pH dependent, highlights a new reaction intermediate, and reasonably recreates the observed experimental kinetics. Future work will focus on elucidating the molecular mechanism of thiosulfate adsorption to the air-water interface.

References
(1)   Ryskie, S.; Neculita, C. M.; Rosa, E.; Coudert, L.; Couture, P. Active Treatment of Contaminants of Emerging Concern in Cold Mine Water Using Advanced Oxidation and Membrane-Related Processes: A Review. *Minerals* **2021**, *11* (3), 259. https://doi.org/10.3390/min11030259.
(2)   Neculita, C. M.; Coudert, L.; Rosa, E.; Mulligan, C. N. Future Prospects for Treating Contaminants of Emerging Concern in Water and Soils/Sediments. In *Advanced Nano-Bio Technologies for Water and Soil Treatment*; Filip, J., Cajthaml, T., Najmanová, P., Černík, M., Zbořil, R., Eds.; Springer International Publishing: Cham, 2020; pp 589–605. https://doi.org/10.1007/978-3-030-29840-1_29.
(3)   Miranda-Trevino, J. C.; Pappoe, M.; Hawboldt, K.; Bottaro, C. The Importance of Thiosalts Speciation: Review of Analytical Methods, Kinetics, and Treatment. *Critical Reviews in Environmental Science and Technology* **2013**, *43* (19), 2013–2070. https://doi.org/10.1080/10643389.2012.672047.
(4)   Penner, J. E.; Chuang, C. C.; Grant, K. Climate Forcing by Carbonaceous and Sulfate Aerosols. *Climate Dynamics* **1998**, *14* (12), 839–851. https://doi.org/10.1007/s003820050259.
(5)   Deike, L. Mass Transfer at the Ocean–Atmosphere Interface: The Role of Wave Breaking, Droplets, and Bubbles. *Annual Review of Fluid Mechanics* **2022**, *54* (Volume 54, 2022), 191–224. https://doi.org/10.1146/annurev-fluid-030121-014132.
(6)   Enami, S.; Vecitis, C. D.; Cheng, J.; Hoffmann, M. R.; Colussi, A. J. Electrospray Mass Spectrometric Detection of Products and Short-Lived Intermediates in Aqueous Aerosol Microdroplets Exposed to a Reactive Gas. *J. Phys. Chem. A* **2007**, *111* (50), 13032–13037. https://doi.org/10.1021/jp075505r.
(7)   Hsu, S.-H.; Lin, F.-Y.; Huang, G. G.; Chang, Y.-P. Accelerated Sulfur Oxidation by Ozone on Surfaces of Single Optically Trapped Aerosol Particles. *J. Phys. Chem. C* **2023**, *127* (13), 6248–6261. https://doi.org/10.1021/acs.jpcc.2c06831.
(8)   Petersen, P. B.; Saykally, R. J. Probing the Interfacial Structure of Aqueous Electrolytes with Femtosecond Second Harmonic Generation Spectroscopy. *J. Phys. Chem. B* **2006**, *110* (29), 14060–14073. https://doi.org/10.1021/jp0601825.
(9)   Bernal, F.; Dodin, A.; Kyprianou, C.; Limmer, D. T.; Saykally, R. J. Adsorption of Guanidinium Cations to the Air-Water Interface, 2024. https://arxiv.org/abs/2408.15423.
(10)   Shen, Y. R. Optical Second Harmonic Generation at Interfaces. *Annual Review of Physical Chemistry* **1989**, *40* (1), 327–350. https://doi.org/10.1146/annurev.pc.40.100189.001551.
(11)   Blandamer, M. J.; Fox, M. F. Theory and Applications of Charge-Transfer-to-Solvent Spectra. *Chem. Rev.* **1970**, *70* (1), 59–93. https://doi.org/10.1021/cr60263a002.

(12)   Jacobs, M. I.; Davies, J. F.; Lee, L.; Davis, R. D.; Houle, F.; Wilson, K. R. Exploring Chemistry in Microcompartments Using Guided Droplet Collisions in a Branched Quadrupole Trap Coupled to a Single Droplet, Paper Spray Mass Spectrometer. *Anal. Chem.* **2017**, *89* (22), 12511–12519. https://doi.org/10.1021/acs.analchem.7b03704.

(13)   Van Berkel, G. J.; Kertesz, V. An Open Port Sampling Interface for Liquid Introduction Atmospheric Pressure Ionization Mass Spectrometry. *Rapid Communications in Mass Spectrometry* **2015**, *29* (19), 1749–1756. https://doi.org/10.1002/rcm.7274.

(14)   *Kinetiscope - A stochastic kinetics simulator*. https://hinsberg.net/kinetiscope/ (accessed 2024-11-07).

(15)   Willis, M. D.; Rovelli, G.; Wilson, K. R. Combining Mass Spectrometry of Picoliter Samples with a Multicompartment Electrodynamic Trap for Probing the Chemistry of Droplet Arrays. *Anal. Chem.* **2020**, *92* (17), 11943–11952. https://doi.org/10.1021/acs.analchem.0c02343.

(16)   Drisdell, W. S.; Saykally, R. J.; Cohen, R. C. On the Evaporation of Ammonium Sulfate Solution. *Proceedings of the National Academy of Sciences* **2009**, *106* (45), 18897–18901. https://doi.org/10.1073/pnas.0907988106.

(17)   Litman, Y.; Chiang, K.-Y.; Seki, T.; Nagata, Y.; Bonn, M. Surface Stratification Determines the Interfacial Water Structure of Simple Electrolyte Solutions. *Nat. Chem.* **2024**, 1–7. https://doi.org/10.1038/s41557-023-01416-6.

(18)   Pegram, L. M.; Record, M. T. Hofmeister Salt Effects on Surface Tension Arise from Partitioning of Anions and Cations between Bulk Water and the Air−Water Interface. *J. Phys. Chem. B* **2007**, *111* (19), 5411–5417. https://doi.org/10.1021/jp070245z.

(19)   Seki, T.; Yu, C.-C.; Chiang, K.-Y.; Greco, A.; Yu, X.; Matsumura, F.; Bonn, M.; Nagata, Y. Ions Speciation at the Water–Air Interface. *J. Am. Chem. Soc.* **2023**, *145* (19), 10622–10630. https://doi.org/10.1021/jacs.3c00517.

(20)   Bian, H.; Feng, R.; Xu, Y.; Guo, Y.; Wang, H. Increased Interfacial Thickness of the NaF, NaCl and NaBr Salt Aqueous Solutions Probed with Non-Resonant Surface Second Harmonic Generation (SHG). *Phys. Chem. Chem. Phys.* **2008**, *10* (32), 4920–4931. https://doi.org/10.1039/B806362A.

(21)   Devlin, S. W.; Jamnuch, S.; Xu, Q.; Chen, A. A.; Qian, J.; Pascal, T. A.; Saykally, R. J. Agglomeration Drives the Reversed Fractionation of Aqueous Carbonate and Bicarbonate at the Air–Water Interface. *J. Am. Chem. Soc.* **2023**, *145* (41), 22384–22393. https://doi.org/10.1021/jacs.3c05093.

(22)   Onsager, L.; Samaras, N. N. T. The Surface Tension of Debye-Hückel Electrolytes. *The Journal of Chemical Physics* **1934**, *2* (8), 528–536. https://doi.org/10.1063/1.1749522.

(23)   Jungwirth, P.; Tobias, D. J. Ions at the Air/Water Interface. *J. Phys. Chem. B* **2002**, *106* (25), 6361–6373. https://doi.org/10.1021/jp020242g.

(24)   Lam, R. K.; Smith, J. W.; Rizzuto, A. M.; Karslıoğlu, O.; Bluhm, H.; Saykally, R. J. Reversed Interfacial Fractionation of Carbonate and Bicarbonate Evidenced by X-Ray Photoemission Spectroscopy. *J. Chem. Phys.* **2017**, *146* (9), 094703. https://doi.org/10.1063/1.4977046.

(25)   Ekholm, V.; Vazdar, M.; Mason, P. E.; Bialik, E.; Walz, M.-M.; Öhrwall, G.; Werner, J.; Rubensson, J.-E.; Jungwirth, P.; Björneholm, O. Anomalous Surface Behavior of Hydrated Guanidinium Ions Due to Ion Pairing. *J. Chem. Phys.* **2018**, *148* (14), 144508. https://doi.org/10.1063/1.5024348.

(26)   Deal, A. M.; Prophet, A. M.; Bernal, F.; Saykally, R. J.; Wilson, K. R. A Detailed Reaction Mechanism for Thiosulfate Oxidation by Ozone in Aqueous Environments. *Environ. Sci. Technol.* **2024**. https://doi.org/10.1021/acs.est.4c06188.

(27)   Wayman, M.; Lem, W. J. Decomposition of Aqueous Dithionite. Part II. A Reaction Mechanism for the Decomposition of Aqueous Sodium Dithionite. *Can. J. Chem.* **1970**, *48* (5), 782–787. https://doi.org/10.1139/v70-127.

(28)   Erickson, R. E.; Yates, L. M.; Clark, R. L.; Mcewen, D. The Reaction of Sulfur Dioxide with Ozone in Water and Its Possible Atmospheric Significance. *Atmospheric Environment (1967)* **1977**, *11* (9), 813–817. https://doi.org/10.1016/0004-6981(77)90043-9.

(29)   Varga, D.; Horváth, A. K. Kinetics and Mechanism of the Decomposition of Tetrathionate Ion in Alkaline Medium. *Inorg. Chem.* **2007**, *46* (18), 7654–7661. https://doi.org/10.1021/ic700992u.

(30)   Onorato, R. M.; Otten, D. E.; Saykally, R. J. Adsorption of Thiocyanate Ions to the Dodecanol/Water Interface Characterized by UV Second Harmonic Generation. *Proceedings of the National Academy of Sciences* **2009**, *106* (36), 15176–15180. https://doi.org/10.1073/pnas.0904800106.

(31)   Petersen, P. B.; Saykally, R. J. Is the Liquid Water Surface Basic or Acidic? Macroscopic vs. Molecular-Scale Investigations. *Chemical Physics Letters* **2008**, *458* (4), 255–261. https://doi.org/10.1016/j.cplett.2008.04.010.

Chapter 5 – Searching for Liquid Carbon: MeV-UED and RIXS Studies of Laser Irradiated Diamond

The following is adapted from:

Bernal, F.; Riffe, E. J.; Devlin, S. W.; Hamel, S.; Lindsey, R. K.; Reid, A. H.; Mo, M.; Luo, D.; Kramer, P.; Shen, X.; et al. Response of Fs-Laser-Irradiated Diamond by Ultrafast Electron Diffraction. *J. Phys. Chem. C* **2024**. https://doi.org/10.1021/acs.jpcc.4c05999.

Riffe, E. J.; Bernal, F.; Kamal, C.; Mizuno, H.; Lindsey, R. K.; Hamel, S.; Raj, S. L.; Hull, C. J.; Kwon, S.; Park, S. H.; et al. Time-Resolved X-Ray Emission Spectroscopy and Resonant Inelastic X-Ray Scattering Spectroscopy of Laser Irradiated Carbon. *J. Phys. Chem. B* **2024**, *128* (26), 6422–6433. https://doi.org/10.1021/acs.jpcb.4c02862.

5.1. Introduction

Novel carbon materials are of much current interest, as their applications could engender profound advances in the areas of catalysis, energy storage, CO_2 conversion, and nuclear waste management.[1–4] Theoretical studies have suggested that the liquid phase of carbon may be the precursor to new exotic carbon nanostructures.[5,6] However, without reliable experimental evidence addressing the structure of liquid carbon, present day theoretical models remain limited in their ability to understand and predict the formation of novel forms of carbon. Given the planetary core-level pressures and temperatures required to successfully melt carbon without sublimation, characterizing its liquid state by table-top experiments has remained challenging.[7] Experimental evidence of melted carbon was first reported by Bundy in 1963, who performed flash-heating experiments on graphite rods inside a high-pressure cell.[8] Since then, a variety of methods have been used to melt carbon, including shock compression, electrical heating, and laser irradiation.[8–11] Numerous types of carbon targets have been examined (e.g. amorphous carbon (a-C), highly ordered pyrolytic graphite (HOPG), and diamond), with sample thicknesses ranging from angstroms to millimeters.[8,11–13] Under laboratory conditions, as carbon samples are non-thermally melted, the liquid phase is claimed to exist only briefly before rapidly evaporating. Melting carbon samples via irradiation with ultrafast optical pulses has become a common approach; however, the observation window of the liquid state is also limited by hydrodynamic expansion and ablation.[14,15] Therefore, attempts to characterize the liquid have typically relied on optical measurements that operate on short timescales. Various groups have employed X-ray spectroscopy and optical reflectivity experiments to characterize non-thermally melted carbon samples; however, these studies have often reached conflicting conclusions.[12,14,16–18] New tools with state-of-the-art time resolution and enhanced signal-to-noise ratios are clearly necessary to unambiguously characterize the structure of the transient liquid carbon state.

Given diamond's unique thermal and optical properties, there is great potential for its applications for optics and electronics.[19] Advances in chemical vapor deposition (CVD) instrumentation have increased the production of highly-ordered diamond samples.[20] Consequently, much effort has been directed towards examining the resilience of lab-grown diamonds, including their damage threshold from laser sources.[21,22] With sufficient energy,

graphitization of diamond occurs whereby the diamond FCC lattice structure transforms into a graphite-like structure.[23] Reports of laser induced graphitization of diamond samples have established that a single laser pulse can generate a change in the diamond structure near the surface. For femtosecond laser pulses, the graphitization threshold has been reported to be ca. 0.3 - 4 J/cm^2.[24,25,23] Fluences greater than 30 J/cm^2 have been used for the graphitization of bulk diamond samples.[25] While this phase transition in the carbon structure has been extensively studied as a method for generating HOPG, the mechanistic details have only recently been explored.[26,23,27] Excitation from an ultrafast laser pulse results in absorption of energy occurring on the order of femtoseconds, which drives the diamond into a nonequilibrium state well before the surrounding structure can respond.[21] Probing such an excited diamond in the picosecond time regime after the absorbed energy has begun to dissipate into the bulk lattice should provide insight into the structural evolution of the graphitization process, and evidence of whether a transient liquid carbon phase is involved.

With the increased time resolution of modern megaelectronvolt-ultrafast diffraction, we are able to generate single-shot static diffraction images of materials and provide time-dependent snapshots of the transient atomic structure several picoseconds after excitation.[28] Changes to the atomic structure (i.e. solid-liquid or solid-solid phase transitions) induced by the excitation pulse are evidenced in the diffraction pattern.[29,30] Mo et al. have successfully demonstrated the utility of this technique by monitoring the heterogeneous and homogeneous melting regimes of gold thin films. Their study revealed the formation of Debye-Scherrer rings between 100 - 1000 ps at low energy densities, and between 10 - 20 ps at higher energy densities. In the case of diamond melting, we would similarly expect the rigid molecular structure to evolve into a disordered liquid state and the corresponding diffraction pattern to exhibit Debye-Scherrer rings.[29,31]

Additionally, with the recent advances in X-ray free electron lasers, facilities can now supply the time-resolution, spectral-resolution, and high flux required to study samples by more photon-hungry techniques such as X-ray emission spectroscopy (XES) and resonant inelastic X-ray spectroscopy (RIXS). Both XES and RIXS are excellent probes of the electronic structure of a material.[32] These techniques involve the absorption of an X-ray photon thereby promoting an electron from the core level into the continuum (XES) or an empty valence band (RIXS), and detecting the emitted photon as a core hole is filled by a valence electron. The resonance with a valence state in RIXS allows for the simultaneous determination of empty electronic states and occupied states. Here, we define RIXS as measurements resonant with states below the second band gap of the target material. Therefore, XES and RIXS are sensitive to the melting dynamics and changes in bonding character of a system, as observed for the water/ice phase transition[33] or the liquid-liquid transition in silicon.[34]

Here, we use 800 nm ultrafast pulses to excite diamond thin films and probe them using modern time-resolved MeV-UED, XES, and RIXS. Tracking the evolution of structural changes with these techniques at various time delays could provide details underlying the development and validation of high-energy density physical models, and could thus greatly advance our understanding of the formation of unique carbon materials.[35] Our findings herein highlight the remarkable resilience of the bulk diamond structure, as MeV-UED demonstrates the structure of diamond remains unaltered for up to 100 ps after excitation from two different laser fluences. XES and RIXS similarly suggest the electronic structure of diamond remains unchanged following excitation. These results indicate that a liquid state does not necessarily form in diamond samples following excitation from ultrafast near-IR pulses.

5.2. Experimental Methods

Ultrafast electron diffraction experiments were conducted at the MeV-UED facility at SLAC National Accelerator Laboratory and are depicted in Figure 5.1.A. A Ti:sapphire laser outputting 800 nm, ~75 fs pulses was used to excite individual diamond windows at fluences of 13 J/cm^2 (200 μm FWHM diameter) and 40 J/cm^2 (100 μm FWHM diameter). The fabrication process for producing ultra-thin Type IIa diamond membrane windows with an <100> orientation entailed a multi-step technique.[36] Each window has a length and width of 170 μm and a thickness < 300 nm. The MeV-UED facility provided accelerated electron pulses (3.7 MeV, ~100 μm diameter) that were directed normal to the diamond windows in transmission geometry. Pump and probe pulses were synchronized and kept spatially overlapped as the target windows were raster-scanned. Samples were probed at 10, 25, and 100 ps time delays following excitation at two different pump fluences (13 and 40 J/cm^2). Static and post-excitation diffraction pattern pairs were recorded by a phosphor-based detector, binned according to fluence and time delay, then averaged (typically 4-5 windows per time delay). All diamond windows used in the analysis were unaffected by the probe pulse and confirmed to have been fully destroyed after the excitation pulse.

Time-resolved RIXS/XES experiments were performed on ultrananocrystalline diamond (UNCD) films near the carbon K-edge, at the soft X-ray scattering and spectroscopy beamline at Pohang Accelerator Laboratory (PAL) X-ray FEL.[32] The UNCD films had a thickness of ca. 400 nm and were purchased from John Crane Inc. A Ti:sapphire laser system provided the 800 nm, 65 fs, 0.88 J/cm^2 non-thermal melting pulses used in these experiments. The pulses were roughly collinear with the PAL-XFEL pulses and were focused onto the sample surface with an incidence angle of ca. 45 degrees with respect to the sample surface normal, as shown in Figure 5.1.B. The samples were rastered and the scattered X-ray photons were collected in a reflection geometry using a RIXS/XES spectrometer with an Andor Newton DO 940 CCD detector. Time-resolved XES/RIXS spectra of non-thermally melted UNCD thin film samples were collected at incident energies of 294 eV, 303 eV, and 308 eV as a function of delay between the melting pulse and PAL-XFEL pulse, ranging from $\Delta t = -1$ to $+100$ ps.
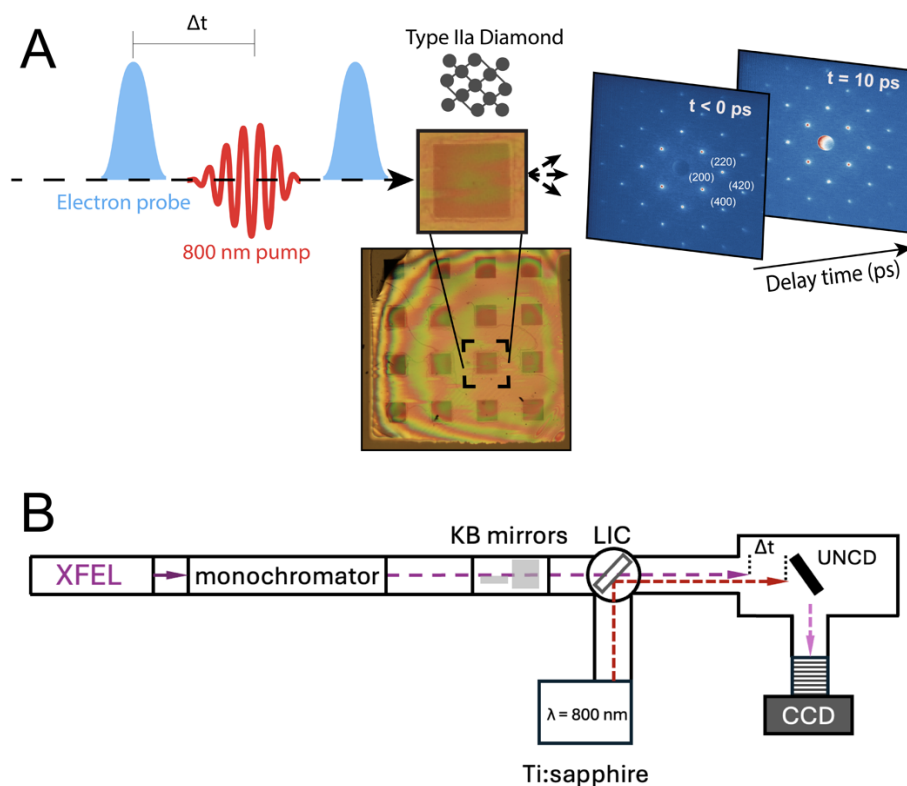
Figure 5.1. Experimental diagrams of MeV-UED and RIXS/XES experiments. **A)** MeV-UED experimental design. An electron pulse is first sent to characterize the pre-excited diamond, followed by synchronized pump-probe pulses. This generates pre- and post-excitation diffraction patterns. **B)** RIXS/XES experimental design. XFEL probe photons are filtered, focused, then spatially overlapped on to the beam path of the pump laser. The pump and probe beams are synchronized, and the reflected X-ray scatter is collected by a CCD detector.

5.3. Results and Discussion

5.3.1. MeV-UED

On initial observation of the static diffraction patterns, there were no obvious qualitative changes pre- and post-pump for all time delays studied. Intensities of each time-dependent diffraction image were subtracted from initial static images to generate the diffraction patterns in Figure 5.2.A-C at 10, 25, and 100 ps, respectively. From these differential diffraction images, the intensity of the diffraction peaks decreases after being exposed to the pump pulse (13 J/cm^2). Previous studies have attributed scattering intensity decreases in single crystalline materials to strongly driven electronic phase transitions occurring on the order of ca. 100 fs post-excitation.[37] Additionally, thermal effects leading to increased atomic vibrations are well-known to cause decreases in scattering intensity via the Debye-Waller factor.[38] Here, we observe no obvious streaking or positional shifts in the diffraction peaks after excitation, nor do we see any indication of Debye-Scherrer rings forming.
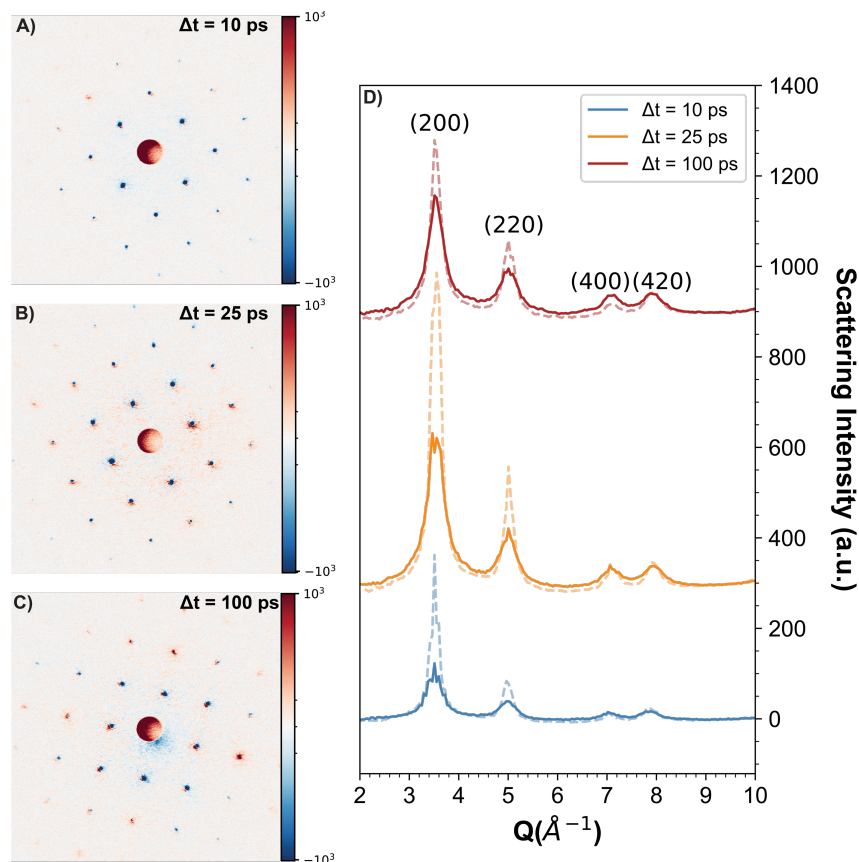
Figure 5.2. MeV-UED diffraction studies of diamond thin films before and after exposure to a non-thermal optical melting pulse (13 J/cm²). (**A** to **C**) Differential diffraction patterns at three time delays: 10, 25, and 100 ps, respectively. Blue and red color shifts represent a decrease and increase in signal intensity, respectively, compared to the static diffraction pattern. (**D**) Radially averaged patterns of diffraction data at each time delay. Dashed traces represent the initial signal at static conditions without the optical pump. The plots are offset from each other for clarity.

We radially averaged a collection of diffraction images at each time delay and converted to Q-space to generate the radial profile plots shown in Figure 5.2.D. The dashed lines represent the pre-excitation patterns and the solid lines are post-excitation; each pre- and post-excitation pair is offset from the next for clarity. As seen in the differential diffraction images, each time delay displays the strongest decrease in intensity at the two low-Q peaks in Figure 5.2.D, corresponding to the central peaks of the diffraction images ((200) and (220)). The two high-Q peaks exhibit little to no change in signal intensity post-excitation ((400) and (420)). The intensity decreases displayed here may be a result of strongly driven diamond undergoing initial bond breaking followed by further lattice effects (i.e. heating and ablation) at longer time delays. If the intensity decreases here were solely due to Debye-Waller effects, we would expect the local structures (high-Q peaks) to distort and diminish in intensity before the long-range structures (low-Q peaks).[29,37] It is unclear why the high-Q peaks remain post-excitation at the various time delays studied here, but this may be an indication of other non-Debye-Waller effects occurring. Overall, the radial profile plots display a lack of significant broadening or shifting in the peaks after excitation.

In Figure 5.3, we used a 40 J/cm² fluence to excite diamond thin films and probed their structure at the same time delays used in Figure 5.2. As shown previously for gold thin films,

increasing the pump fluence can affect melting dynamics and shorten the time needed for liquid state formation.[29] Therefore, studying diamond samples excited with a higher fluence allows access to structures at different pressure and temperature conditions. Again, we are not able to discern any noticeable changes to the diffraction patterns at all time delays, as is indicated by the differential diffraction patterns and radial profile plots in Figure 5.3. Here, the 100 ps data reveals a drastic decrease in intensity noticeable even in the high-Q peaks and may be evidence of increased sample ablation due to the increased fluence. If the melting dynamics are indeed accelerated at an increased fluence, it is surprising that the 10 and 25 ps data at both 13 and 40 J/cm^2 fluences remain similar. This suggests that the bulk diamond structure is largely unaffected by the excitation pulses used here.
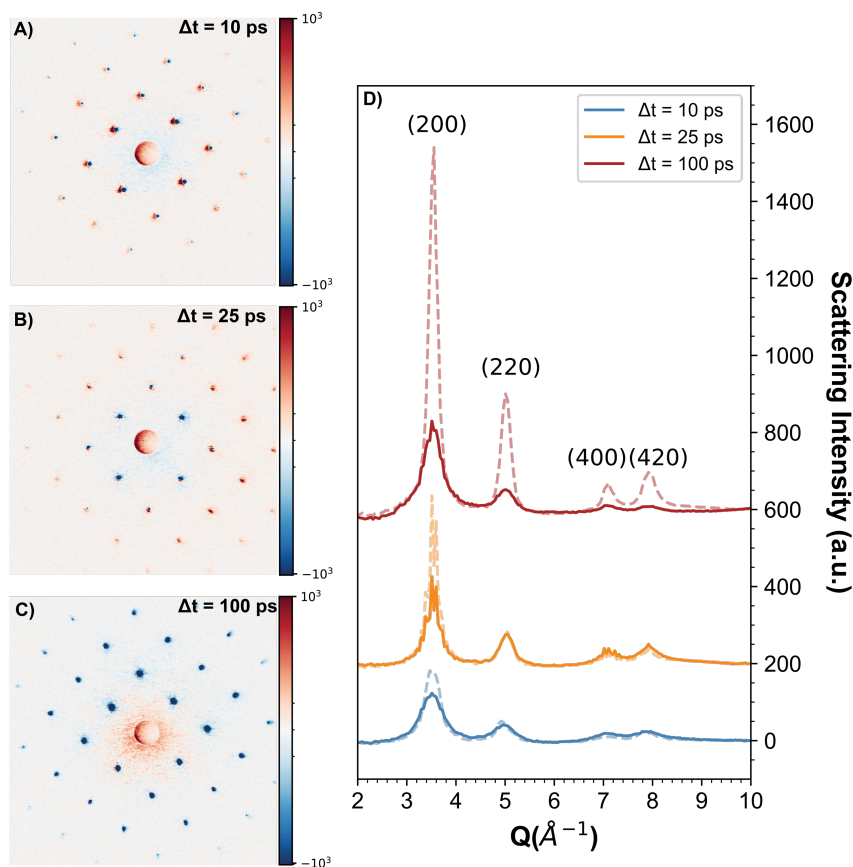
Figure 5.3. MeV-UED diffraction studies of diamond thin films before and after exposure to a non-thermal optical melting pulse (40 J/cm^2). (**A** to **C**) Differential diffraction patterns at three time delays: 10, 25, and 100 ps, respectively. Blue and red color shifts represent a decrease and increase in signal intensity, respectively, compared to the static diffraction pattern. (**D**) Radially averaged patterns of diffraction data at each time delay. Dashed traces represent the initial signal at static conditions without the optical pump. The plots are offset from each other for clarity.

For comparison, we generated radially averaged diffraction patterns using molecular dynamics (MD) simulations where the forces governing the dynamics were either calculated from the electronic structure using Density Functional Theory (DFT) or calculated using the ChIMES interatomic potential. Figure 5.4 shows the computed radial distribution function and scattering intensity from a DFT-MD calculation of carbon at 5000K and 2.27 g/cm^3 performed using the

VASP software as well as results from our previously reported simulations at 2.1g/cm^3 using the ChIMES-MD method as implemented in the LAMMPS simulation code at temperatures of 7000, 14000, and 17000 K.[39–41] The DFT simulation was carried out using the VASP code using the Perdew-Burke-Ernzerhof (PBE) functional.[42–47] A Fourier transform of the simulated radial distribution functions from VASP and LAMMPS was done to convert to reciprocal space (Figure 5.4.B). If the diamond was undergoing a solid-liquid phase transition, we would expect the single-crystal peaks to disappear in the profile plots and the emergence of a broad liquid peak near 5.5 Å^{-1}, as indicated by the simulated structure factor trace in Figure 5.4.B. From the simulations in Figure 5.4.A we observe increasing temperature suppresses the intensity of the peaks in the computed radial distribution functions and broadens the corresponding structure factor, a trend not seen in the experimental data.
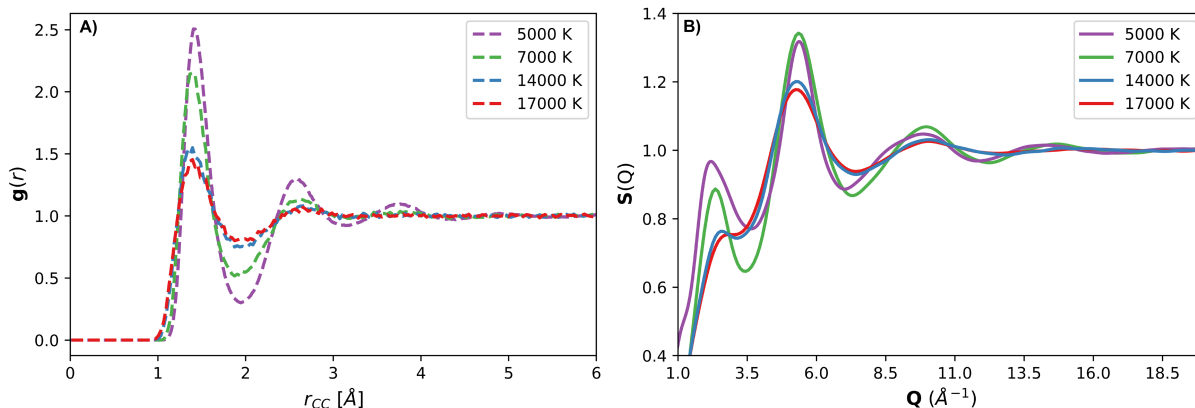
Figure 5.4. Carbon simulations using DFT-MD (5000K and 2.27 g/cm^3) and ChIMES-MD (7000, 14000, and 17000 K and 2.1 g/cm^3). **A)** Simulated radial distribution functions of carbon. **B)** Simulated structure factor of carbon. The small modulations < 3.5 Å^{-1} are artifacts of the Fourier transform and the finite size of the simulation.

These results are surprising, given previous reports of liquid carbon formation and diamond graphitization.[12,23] Both processes involve a transformation of the initial diamond structure, yet our data do not capture any significant differences between pre- and post-excited samples. Studies suggest that liquid carbon formation occurs within the first few picoseconds for laser excited amorphous carbon.[18] Therefore, a 10 ps time delay between the pump and probe would have provided enough time for any liquid carbon formed to equilibrate and begin to cool or evaporate. Longer time delays, 25 and 100 ps, may have provided insight into the lifetime of liquid carbon or the formation of new structures. However, it appears that our diamond samples were not melted using the fluences recorded here; to suggest that bulk diamond was melted by the excitation pulse and then cooled to its original structure within the first 10 ps is unphysical. We see no evidence for a bulk melted structure and any small volumes of surface generated liquid would have been displaced due to surface expansion and evaporation. In addition to the lack of observed melting, we surprisingly do not see structural indications of diamond graphitization.

We are aware of only a few studies addressing the successful melting of a diamond-like sample but that is not the case for diamond graphitization, which is well studied.[17] The pump pulses used here were well above the threshold for graphitization, although there is debate regarding the rate of graphitized diamond production per pulse. A single 100 fs, 10 J/cm^2 laser pulse has been demonstrated to cause graphitization in < 20 nm of diamond[48] and with fluences as high as 200

J/cm^2 reach a max ablation rate of about 100 nm per pulse. Clearly, the pulse energies needed to increase graphitization thickness do not scale linearly and are wavelength dependent[24]. This may account for the diamond scattering patterns in Figure 5.2 and Figure 5.3 exhibiting striking similarities despite the increase in fluence, as graphitization may not have extended as deeply into the bulk.

Since no substantial changes to the initial diffraction pattern of the diamond are observed after excitation with a 13 or 40 J/cm^2 fluences, this suggests that the samples are directly sublimating and not evolving through a phase transition. If a sizeable volume of diamond sample was graphitized by a single pulse, then we would expect to see traces of a hexagonal diffraction pattern in the differential diffraction images. Decreases in diamond scattering intensity have been previously attributed to reorganization of the crystal structure in addition to Debye-Waller effects, which could be an indication of trace amounts of graphitization occurring here[49], but the diffraction pattern remains consistent with that of diamond, and no signs of new peaks emerging due to graphite are found. It is unlikely that the higher fluence generates more graphite than the lower fluence here, since the observed decrease in diffraction intensity remains similar for both at early time delays. It is more likely that the diamond samples are ablated by the pump pulse, which would result in the diamond directly sublimating, thereby reducing the sample thickness and causing localized heating, two processes that would reduce the scattering intensity. This explanation would also agree with laser machined images of polycrystalline diamond samples, wherein femtosecond pulses formed a minimal graphitized layer compared to nanosecond pulses.[50] At long time delays, viz. 1 ms, no scattering intensity is detected, as samples damaged by the pump pulse catastrophically shattered likely due to their free-standing nature.

5.3.2. RIXS/XES

UNCD diamond samples were initially characterized using X-ray absorption spectroscopy (XAS). The XAS spectrum (Figure 5.5.A) of UNCD exhibits a pronounced dip in the spectrum at 303 eV and is indicative of the second band gap in the diamond band structure.[51] The shoulder at ca. 289 eV marks the C 1s core exciton resonance.[52] The broad features before the dip at 303 eV have been attributed to σ^* states of sp^3 bonded carbon.[53]
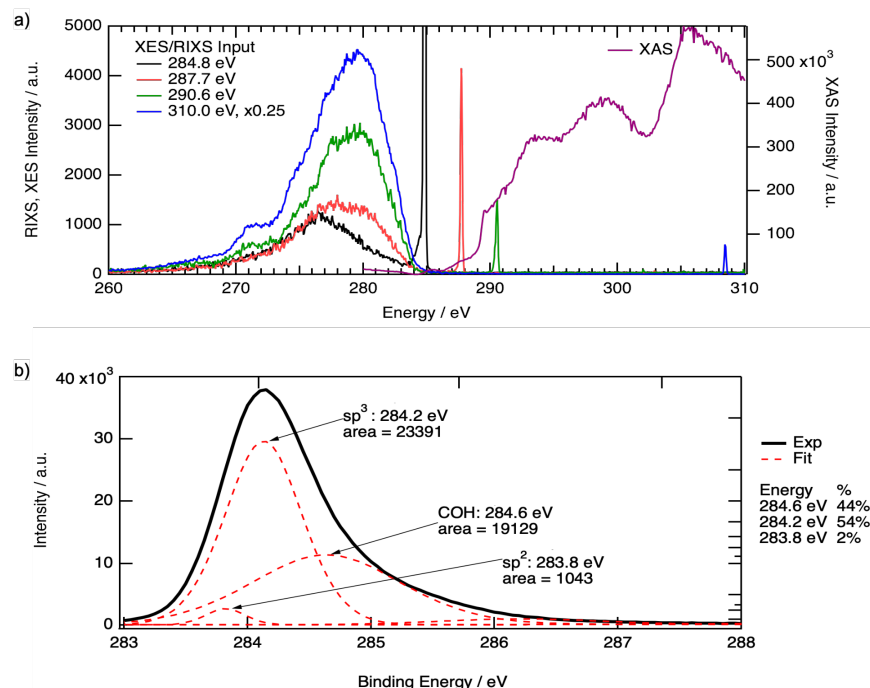
Figure 5.5. Spectra of UNCD samples. **A**) Carbon *K*-edge XES, RIXS, and XAS spectra of unmelted UNCD. The sharp peaks present in the RIXS and XES spectra are elastic scattering peaks. **B**) Deconvolution of X-ray photoelectron spectra of C 1s peaks of unmelted UNCD. Peaks at 283.8 eV and 284.2 eV correspond to sp^2- and sp^3 – carbon atoms. The sp3/sp2 ratio was calculated to be about 22. The peak at 284.6 eV corresponds to carbon-hydroxyl (COH) groups in the near-surface region.

The XES spectra of UNCD exhibit a broad feature near 279 eV, and a lower energy shoulder near 272 eV, observed only at higher input energies (290.6 eV and 310 eV). The intensities of these features are sensitive to the excitation energy. For example, the shoulder at 272 eV is nearly depleted at lower excitation energies of 284.8 and 287.7 eV, which correspond to the amorphous carbon K-edge. When we probe closer to features observed in the UNCD XAS (290.6 and 310 eV), the shoulder at 272 eV is prominent, indicating that we are observing emission from a path in the band structure unique to the sp^3-dominant diamond structure. The peak near 277 eV is stronger for excitation energies preceding the K-edge, and substantially weaker for excitation energies beyond the K-edge. These changes in peak intensity can be used for band structure mapping; the main features in the XES and XAS spectra can be assigned to critical symmetry points of the band structure, as outlined in Ma et al.[54] For example, excitation energies near the K-edge may promote electrons to the X_1 point of the conduction band, because momentum is conserved in RIXS; a valence electron at the X_4 area will relax into the core hole. At excitation energies just beyond the K-edge (290.6 eV), the absorption is assigned to the promotion of an electron to the K_3 point in the conduction band. The most energetically favorable relaxation is to the K_2 point of the valence band, which is assigned to energies near 280 eV.[54] As a result, we observe more intensity around 280 eV than in the 290.6 eV excited RIXS spectra (green line, Figure 4a). The spectra are in excellent agreement with previously reported spectra of diamond and act as a reference to the time resolved RIXS measurements.

60

Peaks in the XPS spectrum (Figure 5.5.B) of UNCD were fit to obtain a sp^3 carbon content percent of 53.7 with only 2.4% of the carbon being to sp^2 hybridized, giving a sp^3/sp^2 ratio of 22.4, and indicating that the sample is overwhelmingly 'diamond-like.' However, there is a large contribution from C-O-H in the near-surface region probed by XPS (284.6 eV), which is likely from surface termination and grain boundaries.[55] The grain boundaries of nanocrystalline diamond will contain sp^2-carbon, defects, and hydrogen, so the XPS spectrum is not expected to exactly match that of a pristine diamond crystal.[38] This should not have a significant effect on the bulk-sensitive XAS, XES, and RIXS measurements.
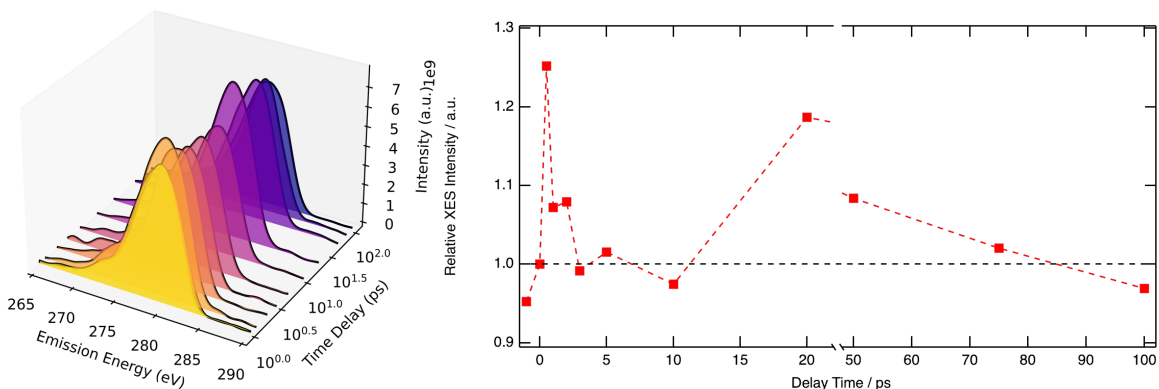
Figure 5.6. XES data of UNCD samples **A)** Time-resolved XES spectra of UNCD at 308 eV. **B)** Normalized intensities of UNCD XES spectra. Spectral changes are very minor across all time delays.

Time-resolved XES spectra from UNCD films were collected at 308 eV, beyond the second band gap in diamond (Figure 5.6.A). Changes in the XES spectra of UNCD are minimal, likely due to the thickness of the UNCD films, leading to a mismatch between pump and probe depth, i.e. not all of the sample was melted. The normalized integrated intensities of the XES spectra were plotted as a function of delay time to show the fluctuations more clearly (Figure 5.6.B). The intensity of the XES spectra increases within the first 0.5 ps by 25% and then slowly returns to the initial intensity 3 ps after the melting pulse. The intensity fluctuates, changing by less than 3% between 3 and 10 ps after the melting pulse. From 10 - 20 ps, the signal increases again, reaching an intensity about 18% greater than that at t = 0 ps. From 20 ps onward, the XES intensity slowly decays, dipping below the initial intensity after >80 ps. The overall loss in intensity was only 3%, less than the change of intensity between negative delay times and 0 ps (4.8%). This indicates that changes to the intensity that are less than about 5% are most likely negligible and cannot be separated from changes in the intensity resulting from instrumental noise (3 – 10 ps data). Our discussion will instead focus on the larger changes in intensity which occurred at 0.5 ps and 20 ps after the optical melting pulse. The increase in intensity at 0.5 ps may indicate that some change to the XES spectra was induced by the melting pulse, however; the change must only affect the intensity of the XES spectra at 308 eV and not induce changes to the peaks position or width. This eliminates most structural changes that might occur if the sample were transitioning to a liquid state. The normal mode analysis performed on the C_5 unit within the diamond lattice shows that vibrational distortions, such as C-C symmetrical stretching or bending can be responsible for oscillations in the intensity of the XES spectra.

While in this experiment, the increase in signal is not preceded by a decrease, which often represents the onset of sample ablation, it is valuable to remember that not all the sample is melted due to the thickness of the UNCD films, and unmelted sample will be contributing to the signal even after ablation. This means that at long times, when ablation has occurred, the signal will represent unmelted sample as well as whatever structures remain following the ablation. Interestingly, since another increase in signal is observed at a delay time of 20 ps, recovery in signal can be attributed to the formation of new structures, such as nanoscale structures in the ablation plume, previously described by the ultrafast grazing incidence X-ray scattering of laser-ablated silicon measured by Hull et al.[39] Those measurements showed the formation of nanoscale inhomogeneities, reminiscent of nanoparticle structures 20 ps after non-thermal melting.[39] Time-resolved RIXS spectra of UNCD were collected at incidence energies of 294 and 303 eV (Figure 5.7). At both energies the relative RIXS energy increases with increasing delay time from the melting pulse. At 294 eV, the increase follows a decrease in the short-time regime. This initial decrease (before 2 ps) may again be attributed to transition blocking. The resulting RIXS spectra don't show a decrease in signal relative to unmelted UNCD. Again, the increase in signal within a 20 ps delay time can be attributed to the formation of new structures, as the sample expands, cools, and ablates and considering that the sample is still thick enough to absorb all the X-rays after ablation.
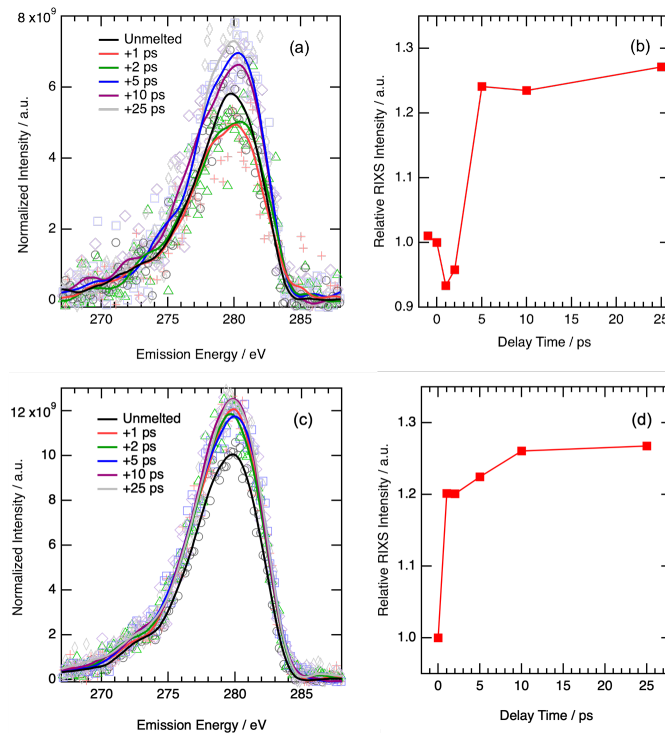
Figure 5.7. Time-resolved RIXS spectra of the unmelted UNCD films and the signal from the sample after varying delay times at input energy of (**A**) 294 eV and (**C**) 303 eV. The intensity of the integrated UNCD emission spectra as a function of delay time is also shown to exemplify the plateau in signal following an initial decrease when using an excitation energy of 303 eV (**D**) and the sharp increase and plateau when using a higher energy excitation of 294 eV (**B**).

To better understand and augment the experimental results, we carried out DFT based electronic structure calculations at the GGA (PBE) level to simulate the XES spectra for diamond using both ground state Kohn-Sham orbitals (GND) and transition potential with half-core holes (TPHH) methods, for which results are presented in Figure 5.8 (solid lines). It is clear that DFT calculations with the TPHH method produced spectra comparable to experiment, capturing the overall spectral features of diamond.

Since the melting pulse is expected to cause a structural change in the carbon samples and XES is sensitive to both the long and short (local) distance changes in the environment, additional TPHH calculations incorporating mechanical strain, both compressive and tensile, were performed. The resulting spectra demonstrate that diamond experiences a spectral red shift and broadening under compressive strain (-10%) and a spectral blue shift and narrowing under tensile strain (+10%) (Figure 5.8 colored traces). While the TPHH calculated spectra capture the unmelted samples well, they indicate spectral shifts-broadening, or narrowing-that are not observed at t > 0 ps in the experimental data, and therefore do not represent the observed transient RIXS and XES results.
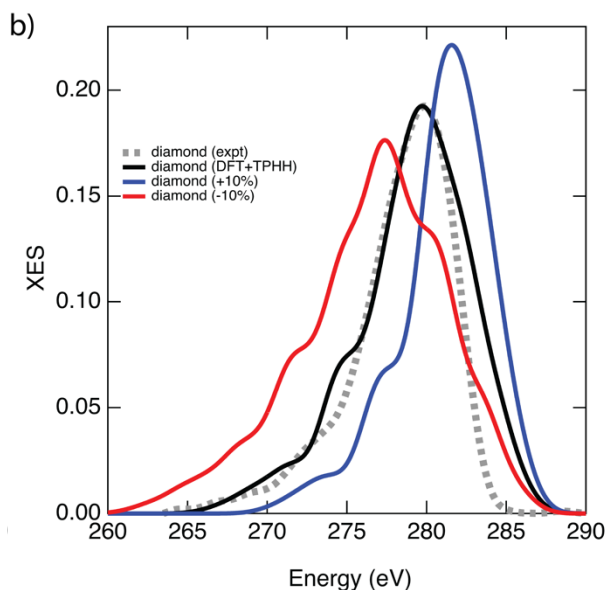
Figure 5.8. Resulting XES spectra for diamond at 308 eV with theoretical modeling of applied mechanical strains. Under tensile strain (+10% blue trace) the spectra narrow and undergo a blue shift. Under compressive strain (-10% red trace) the spectra broaden and undergo a red shift. PBE XC functional along with 6-311 GXX basis set was used for the modeled spectra. All modeled spectra are shifted by 1.2 eV.

In attempts to explain the intensity fluctuations observed in the transient spectra, we also perform the spectral simulations for a diamond cell with local distortions, which were based on normal modes of vibrations around a carbon atom with its first nearest neighbor (forming C_5 unit). XES spectra are sensitive to local structure, so localized distortions were applied along each of the 15 identified modes. In Figure 5.9.A, we see modes 10-12 had the strongest response, corresponding to the C-C-C symmetrical bend and C-C symmetrical stretch vibrations. The difference XES spectra (Figure 5.9.B) show the change in intensity as a function of energy between the undistorted

and distorted C_5 unit. Modes 10-12 show an obvious decrease in signal from 265-280 eV and an increase from 280-285 eV, which may explain the intensity variation observed in the experimental data. The spectral response due to the remaining modes (1-9, 13-15) is very small.
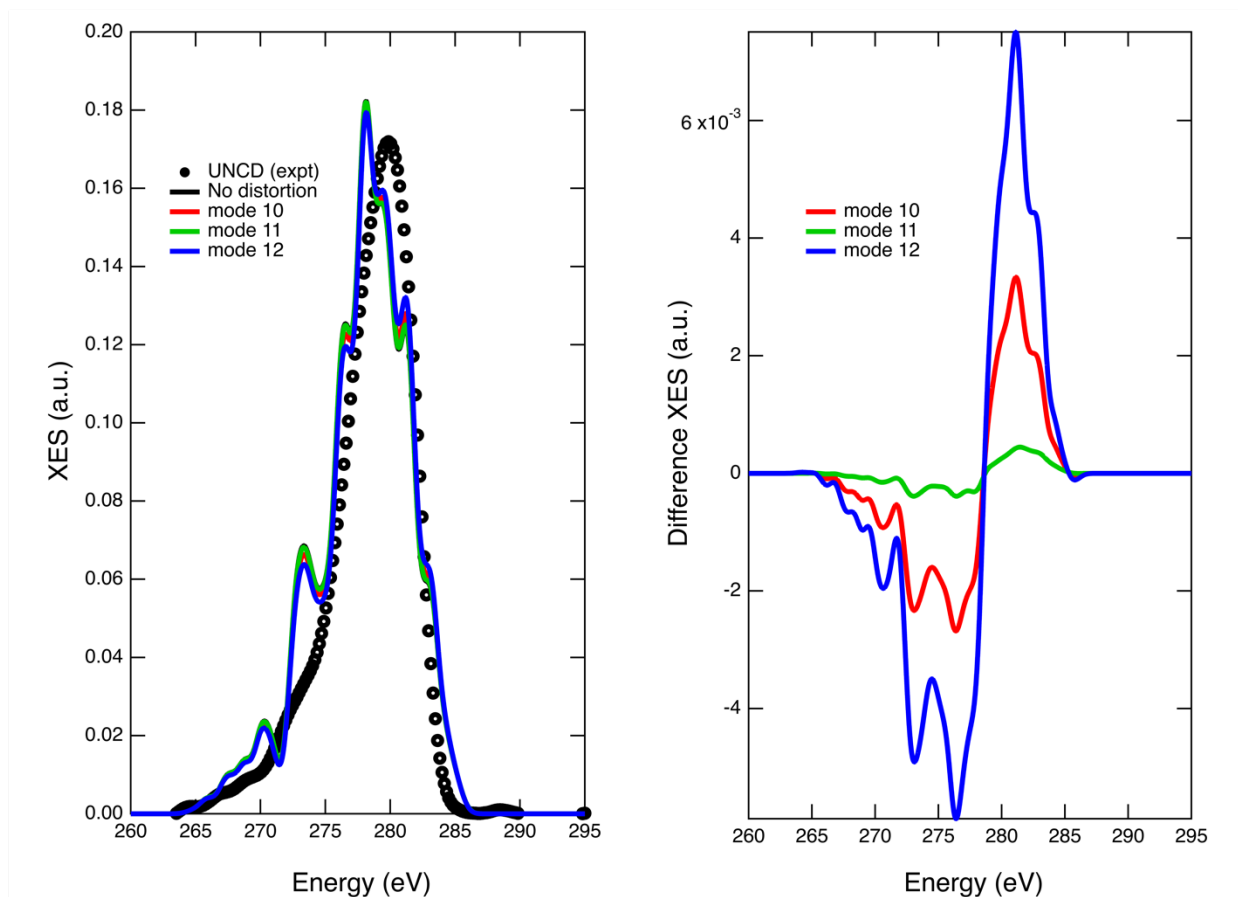
Figure 5.9. Calculated XES spectra following distortion of different normal modes with an amplitude of displacement. Modes 10-12 are expected to have the strongest XES spectral response and represent C-C-C symmetrical bending and C-C symmetrical stretching vibrations.

Comparing the theoretical spectra to the experimental results, it appears that we did not actually measure spectra of liquid carbon in the RIXS/XES experiments. The improved agreement between spectral simulations based on higher (3 or 4-fold) coordination and normal mode analysis indicates that the carbon in the experiments exists in a crystalline or nano-crystalline state. Our results thus appear to question the interpretation of previous studies wherein researchers observed indication of liquid carbon formation from diamond-like samples[16,17]. It is possible that these studies may have evidenced the effects of a plasma state or evaporation cloud formation which we do not see in the present experiment[12,58]. Our MeV-UED and RIXS/XES data suggest that bulk diamond does not undergo a solid-liquid phase transition or graphitization for the fluences and wavelengths used here. Recent studies report the formation of liquid carbon at sub-picosecond time scales via XAS for a-C samples[18]. However, the inference of the liquid state from the XAS data is indirect, and the observed spectral changes could also be consistent with rearrangements of the carbon atoms due to vibrational motion rather than melting. Indeed, our diffraction data of single crystal diamond shows potential signs of slight disordering in the crystal structure, and the

RIXS fluctuations may signal new structures in UNCD diamond, but we do not see a clear indicator of liquid formation.

Given diamond's flat spectral response in the visible spectrum, the excitation process is likely a multiphoton absorption event. It may be that the photon energy supplied by 800 nm pulses is insufficient to drive a significant portion of diamond into an excited state. If our experiments only generated a small volume of liquid carbon on the sample surface, then it is reasonable to suggest that our bulk probes would have difficulty in isolating an interfacial signal. We expect to ablate approximately 80 nm of diamond at the highest fluence used here for MeV-UED experiments based on a previous study. That amount corresponds to approximately 30 % of the sample depth. If a transient liquid state were involved during the ablation process, we see no evidence of it at these timescales. Therefore future studies should emphasize sub-picosecond time-resolution, higher frequency light sources, and thinner samples in order to further characterize the presence of liquid carbon.

5.4. Conclusions

In summary, we used an ultrafast optical pump to non-thermally excite Type IIa diamond and UNCD thin films, and characterized the atomic and electronic structure as a function of time delay using state-of-the-art time-resolved MeV-UED, RIXS, and XES. Type IIa diamond samples were excited with laser fluences of 13 and 40 J/cm^2 at 10, 25 and 100 ps time delays. We observe a reduction in the intensity of the diamond diffraction pattern between 10 and 100 ps with no streaking or shifts in the peak positions. These results are inconsistent with previous reports of liquid carbon formation and diamond graphitization. Time-resolved RIXS and XES spectra of UNCD samples found no evidence of substantial changes from 0.5 ps up to 100 ps after the melting pulse. Decreases in the time-resolved intensities for UNCD are attributed to transition blocking, subsequent relaxation, and eventual ablation of the samples. Normal mode analysis, which shows that vibrational stretching and bending modes of the diamond lattice generate small modulations in the XES spectra, provided evidence for the origin of the small fluctuations in intensity observed in the experimental data. Overall, our MeV-UED experiments see no structural changes and our RIXS/XES measurements find no electronic structure changes allowing us to determine with high certainty that no significant amount of our diamond samples transform into a liquid state or undergo graphitization. This work suggests that femtosecond near-IR pulses are not suitable for generating liquid carbon from diamond samples and future work should explore the use of higher photon energies and sub-picosecond time delays.

References

(1)   Lee, J.; Kim, J.; Hyeon, T. Recent Progress in the Synthesis of Porous Carbon Materials. *Adv. Mater.* **2006**, *18* (16), 2073–2094. https://doi.org/10.1002/adma.200501576.
(2)   Dai, L.; Karakas, O.; Cheng, Y.; Cobb, K.; Chen, P.; Ruan, R. A Review on Carbon Materials Production from Plastic Wastes. *Chem. Eng. J.* **2023**, *453*, 139725. https://doi.org/10.1016/j.cej.2022.139725.
(3)   Duan, X.; Xu, J.; Wei, Z.; Ma, J.; Guo, S.; Wang, S.; Liu, H.; Dou, S. Metal-Free Carbon Materials for CO2 Electrochemical Reduction. *Adv. Mater.* **2017**, *29* (41), 1701784. https://doi.org/10.1002/adma.201701784.

(4)   Belloni, F.; Kütahyali, C.; Rondinella, V. V.; Carbol, P.; Wiss, T.; Mangione, A. Can Carbon Nanotubes Play a Role in the Field of Nuclear Waste Management? *Environ. Sci. Technol.* **2009**, *43* (5), 1250–1255. https://doi.org/10.1021/es802764g.

(5)   Narayan, J.; Bhaumik, A. Novel Phase of Carbon, Ferromagnetism, and Conversion into Diamond. *J. Appl. Phys.* **2015**, *118* (21), 215303. https://doi.org/10.1063/1.4936595.

(6)   Galli, G.; Martin, R. M.; Car, R.; Parrinello, M. Ab Initio Calculation of Properties of Carbon in the Amorphous and Liquid States. *Phys. Rev. B* **1990**, *42* (12), 7470–7482. https://doi.org/10.1103/PhysRevB.42.7470.

(7)   Bundy, F. P. Pressure-Temperature Phase Diagram of Elemental Carbon. *Phys. Stat. Mech. Its Appl.* **1989**, *156* (1), 169–178. https://doi.org/10.1016/0378-4371(89)90115-5.

(8)   Bundy, F. P. Melting of Graphite at Very High Pressure. *J. Chem. Phys.* **1963**, *38* (3), 618–630. https://doi.org/10.1063/1.1733715.

(9)   Savvatimskiy, A. I. Measurements of the Melting Point of Graphite and the Properties of Liquid Carbon (a Review for 1963–2003). *Carbon* **2005**, *43* (6), 1115–1142. https://doi.org/10.1016/j.carbon.2004.12.027.

(10)   Eggert, J. H.; Hicks, D. G.; Celliers, P. M.; Bradley, D. K.; McWilliams, R. S.; Jeanloz, R.; Miller, J. E.; Boehly, T. R.; Collins, G. W. Melting Temperature of Diamond at Ultrahigh Pressure. *Nat. Phys.* **2010**, *6* (1), 40–43. https://doi.org/10.1038/nphys1438.

(11)   Brygoo, S.; Henry, E.; Loubeyre, P.; Eggert, J.; Koenig, M.; Loupias, B.; Benuzzi-Mounaix, A.; Rabec Le Gloahec, M. Laser-Shock Compression of Diamond and Evidence of a Negative-Slope Melting Curve. *Nat. Mater.* **2007**, *6* (4), 274–277. https://doi.org/10.1038/nmat1863.

(12)   Hull, C. J.; Raj, S. L.; Saykally, R. J. The Liquid State of Carbon. *Chem. Phys. Lett.* **2020**, *749*, 137341. https://doi.org/10.1016/j.cplett.2020.137341.

(13)   Kraus, D.; Vorberger, J.; Gericke, D. O.; Bagnoud, V.; Blažević, A.; Cayzac, W.; Frank, A.; Gregori, G.; Ortner, A.; Otten, A.; et al. Probing the Complex Ion Structure in Liquid Carbon at 100 GPa. *Phys. Rev. Lett.* **2013**, *111* (25), 255501. https://doi.org/10.1103/PhysRevLett.111.255501.

(14)   Mincigrucci, R.; Principi, E.; Bencivenga, F.; Foglia, L.; Gessini, A.; Kurdi, G.; Simoncig, A.; Masciovecchio, C. Transient EUV Reflectivity Measurements of Carbon upon Ultrafast Laser Heating. *Photonics* **2017**, *4* (2), 23. https://doi.org/10.3390/photonics4020023.

(15)   Perez, D.; Lewis, L. J. Ablation of Solids under Femtosecond Laser Pulses. *Phys. Rev. Lett.* **2002**, *89* (25), 255504. https://doi.org/10.1103/PhysRevLett.89.255504.

(16)   Reitze, D. H.; Ahn, H.; Downer, M. C. Optical Properties of Liquid Carbon Measured by Femtosecond Spectroscopy. *Phys. Rev. B* **1992**, *45* (6), 2677–2693. https://doi.org/10.1103/PhysRevB.45.2677.

(17)   Johnson, S. L.; Heimann, P. A.; MacPhee, A. G.; Lindenberg, A. M.; Monteiro, O. R.; Chang, Z.; Lee, R. W.; Falcone, R. W. Bonding in Liquid Carbon Studied by Time-Resolved X-Ray Absorption Spectroscopy. *Phys. Rev. Lett.* **2005**, *94* (5), 057407. https://doi.org/10.1103/PhysRevLett.94.057407.

(18)   Principi, E.; Krylow, S.; Garcia, M. E.; Simoncig, A.; Foglia, L.; Mincigrucci, R.; Kurdi, G.; Gessini, A.; Bencivenga, F.; Giglia, A.; et al. Atomic and Electronic Structure of Solid-Density Liquid Carbon. *Phys. Rev. Lett.* **2020**, *125* (15), 155703. https://doi.org/10.1103/PhysRevLett.125.155703.

(19)   Zhang, C.; Vispute, R. D.; Fu, K.; Ni, C. A Review of Thermal Properties of CVD Diamond Films. *J. Mater. Sci.* **2023**, *58* (8), 3485–3507. https://doi.org/10.1007/s10853-023-08232-w.

(20)   Lee, S.-T.; Lin, Z.; Jiang, X. CVD Diamond Films: Nucleation and Growth. *Mater. Sci. Eng. R Rep.* **1999**, *25* (4), 123–154. https://doi.org/10.1016/S0927-796X(99)00003-0.

(21)   Ali, B.; Litvinyuk, I. V.; Rybachuk, M. Femtosecond Laser Micromachining of Diamond: Current Research Status, Applications and Challenges. *Carbon* **2021**, *179*, 209–226. https://doi.org/10.1016/j.carbon.2021.04.025.

(22)   Hsu, E. M.; Mailman, N. A.; Botton, G. A.; Haugen, H. K. Microscopic Investigation of Single-Crystal Diamond Following Ultrafast Laser Irradiation. *Appl. Phys. A* **2011**, *103* (1), 185–192. https://doi.org/10.1007/s00339-010-5986-4.

(23)   Kononenko, V. V. Modification of Diamond Surface by Femtosecond Laser Pulses. *Photonics* **2023**, *10* (10), 1077. https://doi.org/10.3390/photonics10101077.

(24)   Preuss, S.; Stuke, M. Subpicosecond Ultraviolet Laser Ablation of Diamond: Nonlinear Properties at 248 Nm and Time-resolved Characterization of Ablation Dynamics. *Appl. Phys. Lett.* **1995**, *67* (3), 338–340. https://doi.org/10.1063/1.115437.

(25)   Kononenko, V. V.; Khomich, A. A.; Khomich, A. V.; Khmelnitskii, R. A.; Gololobov, V. M.; Komlenok, M. S.; Orekhov, A. S.; Orekhov, A. S.; Konov, V. I. Highly Oriented Graphite Produced by Femtosecond Laser on Diamond. *Appl. Phys. Lett.* **2019**, *114* (25), 251903. https://doi.org/10.1063/1.5097986.

(26)   Evans, T.; James, P. F.; Ditchburn, R. W. A Study of the Transformation of Diamond to Graphite. *Proc. R. Soc. Lond. Ser. Math. Phys. Sci.* **1997**, *277* (1369), 260–269. https://doi.org/10.1098/rspa.1964.0020.

(27)   Li, B.; Liu, B.; Luo, K.; Tong, K.; Zhao, Z.; Tian, Y. Discovery of Gradia between Graphite and Diamond. *Acc. Mater. Res.* **2024**, *5* (5), 614–624. https://doi.org/10.1021/accountsmr.4c00029.

(28)   Filippetto, D.; Musumeci, P.; Li, R. K.; Siwick, B. J.; Otto, M. R.; Centurion, M.; Nunes, J. P. F. Ultrafast Electron Diffraction: Visualizing Dynamic States of Matter. *Rev. Mod. Phys.* **2022**, *94* (4), 045004. https://doi.org/10.1103/RevModPhys.94.045004.

(29)   Mo, M. Z.; Chen, Z.; Li, R. K.; Dunning, M.; Witte, B. B. L.; Baldwin, J. K.; Fletcher, L. B.; Kim, J. B.; Ng, A.; Redmer, R.; et al. Heterogeneous to Homogeneous Melting Transition Visualized with Ultrafast Electron Diffraction. *Science* **2018**, *360* (6396), 1451–1455. https://doi.org/10.1126/science.aar2058.

(30)   Siwick, B. J.; Dwyer, J. R.; Jordan, R. E.; Miller, R. J. D. An Atomic-Level View of Melting Using Femtosecond Electron Diffraction. *Science* **2003**, *302* (5649), 1382–1385. https://doi.org/10.1126/science.1090052.

(31)   Takagi, M. Electron-Diffraction Study of Liquid-Solid Transition of Thin Metal Films. *J. Phys. Soc. Jpn.* **1954**, *9* (3), 359–363. https://doi.org/10.1143/JPSJ.9.359.

(32)   Park, S. H.; Yoon, J.; Kim, C.; Hwang, C.; Kim, D.-H.; Lee, S.-H.; Kwon, S. Scientific Instruments for Soft X-Ray Photon-in/Photon-out Spectroscopy on the PAL-XFEL. *J. Synchrotron Radiat.* **2019**, *26* (4), 1031–1036. https://doi.org/10.1107/S1600577519004272.

(33)   Gallo, P.; Amann-Winkel, K.; Angell, C. A.; Anisimov, M. A.; Caupin, F.; Chakravarty, C.; Lascaris, E.; Loerting, T.; Panagiotopoulos, A. Z.; Russo, J.; et al. Water: A Tale of Two Liquids. *Chem. Rev.* **2016**, *116* (13), 7463–7500. https://doi.org/10.1021/acs.chemrev.5b00750.

(34)   Beye, M.; Sorgenfrei, F.; Schlotter, W. F.; Wurth, W.; Föhlisch, A. The Liquid-Liquid Phase Transition in Silicon Revealed by Snapshots of Valence Electrons. *Proc. Natl. Acad. Sci.* **2010**, *107* (39), 16772–16776. https://doi.org/10.1073/pnas.1006499107.

(35)   Scott, H. A.; Hansen, S. B. Advances in NLTE Modeling for Integrated Simulations. *High Energy Density Phys.* **2010**, *6* (1), 39–47. https://doi.org/10.1016/j.hedp.2009.07.003.

(36)   Habib Piracha, A.; Ganesan, K.; M. Lau, D. W.; Stacey, A.; P. McGuinness, L.; Tomljenovic-Hanic, S.; Prawer, S. Scalable Fabrication of High-Quality, Ultra-Thin Single Crystal Diamond Membrane Windows. *Nanoscale* **2016**, *8* (12), 6860–6865. https://doi.org/10.1039/C5NR08348F.

(37)   Harb, M.; Ernstorfer, R.; Hebeisen, C. T.; Sciaini, G.; Peng, W.; Dartigalongue, T.; Eriksson, M. A.; Lagally, M. G.; Kruglik, S. G.; Miller, R. J. D. Electronically Driven Structure Changes of Si Captured by Femtosecond Electron Diffraction. *Phys. Rev. Lett.* **2008**, *100* (15), 155504. https://doi.org/10.1103/PhysRevLett.100.155504.

(38)   Vila, F. D.; Rehr, J. J.; Rossner, H. H.; Krappe, H. J. Theoretical X-Ray Absorption Debye-Waller Factors. *Phys. Rev. B* **2007**, *76* (1), 014301. https://doi.org/10.1103/PhysRevB.76.014301.

(39)   Lindsey, R. K.; Fried, L. E.; Goldman, N. ChIMES: A Force Matched Potential with Explicit Three-Body Interactions for Molten Carbon. *J. Chem. Theory Comput.* **2017**, *13* (12), 6222–6229. https://doi.org/10.1021/acs.jctc.7b00867.

(40)   Thompson, A. P.; Aktulga, H. M.; Berger, R.; Bolintineanu, D. S.; Brown, W. M.; Crozier, P. S.; in 't Veld, P. J.; Kohlmeyer, A.; Moore, S. G.; Nguyen, T. D.; et al. LAMMPS - a Flexible Simulation Tool for Particle-Based Materials Modeling at the Atomic, Meso, and Continuum Scales. *Comput. Phys. Commun.* **2022**, *271*, 108171. https://doi.org/10.1016/j.cpc.2021.108171.

(41)   Lindsey, R.; Bastea, S.; Hamel, S.; Lyu, Y.; Goldman, N.; Lordi, V. ChIMES Carbon 2.0: A Transferable Machine-Learned Interatomic Model Harnessing Multifidelity Training Data. *ChemRxiv* **2024**. https://doi.org/10.26434/chemrxiv-2024-s1fs5-v2.

(42)   Kresse, G.; Furthmüller, J. Efficiency of Ab-Initio Total Energy Calculations for Metals and Semiconductors Using a Plane-Wave Basis Set. *Comput. Mater. Sci.* **1996**, *6* (1), 15–50. https://doi.org/10.1016/0927-0256(96)00008-0.

(43)   Kresse, G.; Furthmüller, J. Efficient Iterative Schemes for Ab Initio Total-Energy Calculations Using a Plane-Wave Basis Set. *Phys. Rev. B* **1996**, *54* (16), 11169–11186. https://doi.org/10.1103/PhysRevB.54.11169.

(44)   Kresse, G.; Hafner, J. Ab Initio Molecular Dynamics for Liquid Metals. *Phys. Rev. B* **1993**, *47* (1), 558–561. https://doi.org/10.1103/PhysRevB.47.558.

(45)   Kresse, G.; Hafner, J. Ab Initio Molecular-Dynamics Simulation of the Liquid-Metal--Amorphous-Semiconductor Transition in Germanium. *Phys. Rev. B* **1994**, *49* (20), 14251–14269. https://doi.org/10.1103/PhysRevB.49.14251.

(46)   Perdew, J. P.; Burke, K.; Ernzerhof, M. Generalized Gradient Approximation Made Simple. *Phys. Rev. Lett.* **1996**, *77* (18), 3865–3868. https://doi.org/10.1103/PhysRevLett.77.3865.

(47)   Perdew, J. P.; Burke, K.; Ernzerhof, M. Generalized Gradient Approximation Made Simple [Phys. Rev. Lett. 77, 3865 (1996)]. *Phys. Rev. Lett.* **1997**, *78* (7), 1396–1396. https://doi.org/10.1103/PhysRevLett.78.1396.

(48)   Kononenko, V. V.; Kononenko, T. V.; Pimenov, S. M.; Sinyavskii, M. N.; Konov, V. I.; Dausinger, F. Effect of the Pulse Duration on Graphitisation of Diamond during Laser Ablation. *Quantum Electron.* **2005**, *35* (3), 252. https://doi.org/10.1070/QE2005v035n03ABEH002900.

(49)   Heimann, P.; Hartley, N. J.; Inoue, I.; Tkachenko, V.; Antoine, A.; Dorchies, F.; Falcone, R.; Gaudin, J.; Höppner, H.; Inubushi, Y.; et al. Non-Thermal Structural Transformation of Diamond Driven by x-Rays. *Struct. Dyn.* **2023**, *10* (5), 054502. https://doi.org/10.1063/4.0000193.

(50)   Ogawa, Y.; Ota, M.; Nakamoto, K.; Fukaya, T.; Russell, M.; Zohdi, T. I.; Yamazaki, K.; Aoyama, H. A Study on Machining of Binder-Less Polycrystalline Diamond by Femtosecond Pulsed Laser for Fabrication of Micro Milling Tools. *CIRP Ann.* **2016**, *65* (1), 245–248. https://doi.org/10.1016/j.cirp.2016.04.081.

(51)   García, M. M.; Jiménez, I.; Vázquez, L.; Gómez-Aleixandre, C.; Albella, J. M.; Sánchez, O.; Terminello, L. J.; Himpsel, F. J. X-Ray Absorption Spectroscopy and Atomic Force Microscopy Study of Bias-Enhanced Nucleation of Diamond Films. *Appl. Phys. Lett.* **1998**, *72* (17), 2105–2107. https://doi.org/10.1063/1.121290.

(52)   Morar, J. F.; Himpsel, F. J.; Hollinger, G.; Hughes, G.; Jordan, J. L. Observation of a C- 1 s Core Exciton in Diamond. *Phys. Rev. Lett.* **1985**, *54* (17), 1960–1963. https://doi.org/10.1103/PhysRevLett.54.1960.

(53)   Chang, Y. K.; Hsieh, H. H.; Pong, W. F.; Tsai, M.-H.; Lee, K. H.; Dann, T. E.; Chien, F. Z.; Tseng, P. K.; Tsang, K. L.; Su, W. K.; et al. Electronic and Atomic Structures of the Si-C-N Thin Film by x-Ray-Absorption Spectroscopy and Theoretical Calculations. *Phys. Rev. B* **1998**, *58* (14), 9018–9024. https://doi.org/10.1103/PhysRevB.58.9018.

(54)   Ma, Y.; Wassdahl, N.; Skytt, P.; Guo, J.; Nordgren, J.; Johnson, P. D.; Rubensson, J.-E.; Boske, T.; Eberhardt, W.; Kevan, S. D. Soft-x-Ray Resonant Inelastic Scattering at the C *K* Edge of Diamond. *Phys. Rev. Lett.* **1992**, *69* (17), 2598–2601. https://doi.org/10.1103/PhysRevLett.69.2598.

(55)   Kumar, N.; Kozakov, A. T.; Dash, S.; Tyagi, A. K.; Lin, I. N. Microstructure, Chemical Bonds, and Friction Properties of Nanocrystalline Diamond Films Deposited in Two Different Plasma Media. *Phys. Solid State* **2013**, *55* (10), 2076–2087. https://doi.org/10.1134/S1063783413100181.

(56)   Walter, M.; Mangolini, F.; McClimon, J. B.; Carpick, R. W.; Moseler, M. Fermi Level Pinning by Defects Can Explain the Large Reported Carbon 1s Binding Energy Variations in Diamond.

(57)   Hull, C.; Raj, S.; Lam, R.; Katayama, T.; Pascal, T.; Drisdell, W. S.; Saykally, R.; Schwartz, C. P. Early Time Dynamics of Laser-Ablated Silicon Using Ultrafast Grazing Incidence X-Ray Scattering. *Chem. Phys. Lett.* **2019**, *736*, 136811. https://doi.org/10.1016/j.cplett.2019.136811.

(58)   Brown, C. R. D.; Gericke, D. O.; Cammarata, M.; Cho, B. I.; Döppner, T.; Engelhorn, K.; Förster, E.; Fortmann, C.; Fritz, D.; Galtier, E.; et al. Evidence for a Glassy State in Strongly Driven Carbon. *Sci. Rep.* **2014**, *4* (1), 5214. https://doi.org/10.1038/srep05214.